1-1-2014

Applications of Hyperpolarized Xenon-129 Nmr and Chemical Exchange Saturation Transfer in Biosensing

Yubin Bai
University of Pennsylvania, baiyubin@gmail.com

Applications of Hyperpolarized Xenon-129 Nmr and Chemical Exchange Saturation Transfer in Biosensing

Abstract
Modern clinical applications require precise positional and temporal information regarding pathological changes in cells and tissues. For example, in magnetic resonance microscopy, better than 100 sq. micros per voxel spatial resolution is necessary for imaging capillary blood vessels. And in order to monitor the blood flows in brain tissues, a series of images must be acquired in less than 2 s intervals. Further, molecular imaging aims at visualizing molecules and molecular events that occur at a cellular level, i.e. sensing biological events at a fundamentally microscopic level. When compared to other imaging modalities, the main advantages of magnetic resonance imaging (MRI) are its millimeter-scale spatial resolution and wide applicability achieved with minimal perturbation to in vivo systems, whereas its major drawbacks are limited sensitivity (10 protons in a million contribute to magnetic resonance) and high cost (a million US dollars each MRI scanner). One promising solution to both problems is the combination of hyperpolarized 129Xe MRI with biosensors, which offers significant sensitivity enhancement at a much lower cost.

This dissertation reports my progress in hyperpolarized 129Xe nuclear magnetic resonance (NMR) studies for use in future molecular/medical MRI applications. First, I provide an overview of molecular imaging and, specifically, magnetic resonance imaging (MRI). 129Xe NMR/MRI is particularly promising as it solves solves the common problems of signal intensity and specificity (by employing biosensors).

In chapter 2, I present our hyperpolarization (nuclear spin polarization) method. A hyperpolarized 129Xe chemical exchange saturation transfer (Hyper-CEST) method was also applied to lower the biosensor detection limits significantly. These experiments were made possible through the development of a home-built 129Xe hyperpolarizer, continuous-flow hyperpolarized Xe delivery setup, Hyper-CEST pulse sequence, and accompanying NMR control programs.

In chapter 3, interactions between various biosensors and their target proteins have been characterized and analyzed in finer detail than previous studies. 129Xe NMR studies for biosensors targeting human carbonic anhydrase, alpha_{v}beta_{3} integrin, and pH changes have been carried out.

In chapter 4, hyperpolarized 129Xe chemical exchange saturation transfer (Hyper-CEST) NMR experiments have demonstrated unprecedented detection sensitivity for a synthetic xenon host molecule, tri-acetic acid cryptophane.

In chapter 5, to describe interactions between xenon and bacterial spores, Hyper-CEST has been successfully applied; Xe is demonstrated to be a good probe of the spore interior structure. Six spores strains with different protective layers were clearly distinguished by Xe exchanges between spore and water, observed by Hyper-CEST.

Finally, these results are summarized in chapter 6.

Degree Type
Dissertation

APPLICATIONS OF HYPERPOLARIZED XENON-129 NMR AND CHEMICAL EXCHANGE SATURATION TRANSFER IN BIOSENSING

Yubin Bai

A DISSERTATION

in

Chemistry

Presented to the Faculties of the University of Pennsylvania in Partial Fulfillment of the Requirements for the Degree of Doctor of Philosophy

2014

_____

Ivan J. Dmochowski, Associate Professor of Chemistry
Supervisor of Dissertation

_____

Gary A. Molander, Hirschmann-Makineni Professor of Chemistry
Graduate Group Chairperson

Dissertation Committee:
Jeffery G. Saven, Associate Professor of Chemistry (Chair)
Tobias Baumgart, Associate Professor of Chemistry
Feng Gai, Professor of Chemistry

To my parents, who supported all my decisions unconditionally.

To my friends, for all your generous help.

Acknowledgments

I would like to thank my supervisor, Prof. Ivan Dmochowski, for his continuous effort to lighten my path for research work. During my years in the group, we had innumerable fruitful discussions and I really admire his passion in research.

I would also like to thank the Dmochowski lab members: Xinjing Tang, Dage Liu, Olena Taratula, P. Aru Hill, Garry Seward, Julia Richards, Najat Khan, Brittani Ruble, Julie Griepenburg, Jasmina Cheng-lau, Zhengzheng Liao, Brittany Riggle, Sean Yeldell, Yanfei Wang, Ben Roose. Without their help I wouldn't have accomplished my work.

I received many valuable insights from my collaborators over the past several years. Dr. Nick Kuzma guided the initial trials of xenon-129 hyperpolarization. Dr. Nick Turro provided opportunity for an interesting fullerene study with xenon-129. Dr. Mark Goulian and Dr. Adam Driks provided various samples and helped make some key decisions for the bacterial spore work.

Drs. George Furst and Jun Gu of the UPenn NMR facilities provided help in supporting my requests for my xenon experiments. Friends in the chemistry

graduate program greatly boosted my morale over the hard times. Numerous other laboratories, both in the department and outside, have guaranteed access to many instruments and training.

I would also like to thank dissertation committee members, Prof. Tobias Baumgart, Prof. Feng Gai, and Prof. Jeffery Saven, for all their advice throughout the years.

ABSTRACT

APPLICATIONS OF HYPERPOLARIZED XENON-129 NMR AND CHEMICAL EXCHANGE SATURATION TRANSFER IN BIOSENSING

Yubin Bai

Ivan J. Dmochowski

Modern clinical applications require precise positional and temporal information regarding pathological changes in cells and tissues. For example, in magnetic resonance microscopy, better than 100 μm^3 per voxel spatial resolution is necessary for imaging capillary blood vessels. And in order to monitor the blood flows in brain tissues, a series of images must be acquired in less than 2 s intervals. Further, molecular imaging aims at visualizing molecules and molecular events that occur at a cellular level, i.e. sensing biological events at a fundamentally microscopic level. When compared to other imaging modalities, the main advantages of magnetic resonance imaging (MRI) are its millimeter-scale spatial resolution and wide applicability achieved with minimal perturbation to *in vivo* systems, whereas its major drawbacks are limited sensitivity (10 protons in a million contribute to magnetic resonance) and high cost (a million US dollars each MRI scanner). One promising solution to both problems is the combination of hyperpolarized ^{129}Xe MRI with biosensors, which offers significant sensitivity enhancement at a much lower cost.

This dissertation reports my progress in hyperpolarized ^{129}Xe nuclear magnetic resonance (NMR) studies for use in future molecular/medical MRI applications. First, I provide an overview of molecular imaging and, specifically, magnetic resonance imaging (MRI). ^{129}Xe NMR/MRI is particularly promising as it solves solves the common problems of signal intensity and specificity (by employing biosensors).

In chapter 2, I present our hyperpolarization (nuclear spin polarization) method. A hyperpolarized ^{129}Xe chemical exchange saturation transfer (Hyper-CEST) method was also applied to lower the biosensor detection limits significantly. These experiments were made possible through the development of a home-built ^{129}Xe hyperpolarizer, continuous-flow hyperpolarized Xe delivery setup, Hyper-CEST pulse sequence, and accompanying NMR control programs.

In chapter 3, interactions between various biosensors and their target proteins have been characterized and analyzed in finer detail than previous studies. ^{129}Xe NMR studies for biosensors targeting human carbonic anhydrase, $\alpha_v\beta_3$ integrin, and pH changes have been carried out.

In chapter 4, hyperpolarized ^{129}Xe chemical exchange saturation transfer (Hyper-CEST) NMR experiments have demonstrated unprecedented detection sensitivity for a synthetic xenon host molecule, tri-acetic acid cryptophane.

In chapter 5, to describe interactions between xenon and bacterial spores, Hyper-CEST has been successfully applied; Xe is demonstrated to be a good probe of the spore interior structure. Six spores strains with different protective layers were

clearly distinguished by Xe exchanges between spore and water, observed by Hyper-CEST.

Finally, these results are summarized in chapter 6.

Contents

List of Tables

List of Figures

Chapter 1

Introduction

1.1 Molecular Imaging

1.1.1 Current Techniques for Molecular/Medical Imaging

Modern clinical applications require precise positional and temporal information of pathological changes in cells and tissues. With the advent of minimally invasive surgery techniques, the challenges for imaging guidance are becoming even more demanding, especially for cancer treatments. For example, in magnetic resonance microscopy, better than 100 μm^3 per voxel spatial resolution is necessary for imaging capillary blood vessels. And in order to monitor the blood flows in brain tissues, a series of images must be acquired in less than 2 s intervals. Medical imaging seeks to answer multiple questions once a tumor is identified, including whether the tumor is malignant, where the tumor is located, the size of the tumor, whether cancer has begun to metastasize, and whether surgical resection would impact any critical anatomical structures. Medical imaging technologies have experienced tremendous growth over the past few decades, and now play a central role in almost every medical specialty. However, the truly revolutionary techniques that empower effective early-stage disease diagnosis and treatment still lie in the future, when imaging will be achieved at the molecular level.

Molecular imaging aims at visualizing molecules and molecular events that occur at a cellular level, i.e. sensing biological events at a fundamentally microscopic level [1–4]. Currently multiple medical imaging modalities have the potential for

molecular imaging. These include X-ray (including computed tomography, CT), radio-pharmaceutical imaging (positron emission tomography, PET; and single-photon emission computed tomography, SPECT), ultrasound, optical imaging (e.g. biopsy microscopy using fluorescence, bio-luminescence, absorption or reflectance), and magnetic resonance imaging (MRI). Each of these modalities exhibits characteristic advantages and limitations for specific applications. Further, hybrid imaging techniques, like PET-MRI, PET-CT, CT-MRI, are undergoing promising development. The detection of disease, particularly cancer, through the coordinated use of these techniques requires both spatial imaging of tissue and molecular imaging of endogenous and/or artificial biomarkers.

1.1.2 Magnetic Resonance Imaging (MRI)

When compared to other imaging modalities, the main advantages of magnetic resonance imaging (MRI) are its superb spatial resolution and wide applicability achieved with minimal perturbation to *in vivo* systems, whereas its major drawbacks are the limited sensitivity of its probes and high running cost [5].

MRI utilizes the magnetic resonance between the proton nuclear spin magnetic moment and the applied magnetic field. The resonance frequency (Larmor frequency) varies depending on the strength of an applied magnetic field and the chemical environment of the proton under observation, the same phenomenon utilized in nuclear magnetic resonance (NMR) spectroscopy. The water and lipid

proton resonance signals are often utilized due to the high concentration of these species *in vivo*. Through the use of electromagnets within a superconducting magnet providing magnetic polarization, field gradients can be used to encode the location information into distinguishable resonance frequencies, and 3D images can be reconstructed. The performance of MRI for deep tissue imaging is excellent, while achieved with minimal invasion. Compared to CT and PET, MRI is free of radiation hazards accumulated over many scans.

The acquisition and maintenance cost of MRI scanners is among the highest in imaging modalities, although with good justifications. A 1.5 T (60 MHz ^{1}H) clinical MRI scanner currently costs $\sim$1 million U.S. dollars on market, not to mention the running cost of maintaining the superconducting magnets inside. Further, while MRI offers excellent spatial resolution, poor signal-to-noise ratios caused by the inherent insensitivity of magnetic resonance can be problematic in data acquisition and processing.

1.1.3 MRI Contrast Agents

The effective information in medical images is the observed contrast, which is the difference in image brightness (signal intensity) between targets of interest and irrelevant background. In other words, contrast is what makes an object distinguishable in medical images. Sources of MRI contrast include proton density, T_1 relaxation, T_2 relaxation, and chemical shift [5]. Contrast agents, which aim at producing higher

contrast during MRI scans, are developed to improve the MRI image quality, reduce scan time and lower clinical cost. These agents are paramagnetic entities utilizing unpaired electrons to alter either the longitudinal (T_1) or transverse (T_2) relaxation times of water molecules within their effective sphere of action. Current commercial agents rely on the 7 unpaired electrons in the f-orbitals of gadolinium (Gd) to relax the protons of rapidly exchanging coordinated water molecules. It is estimated that 40-50% of the annual 30 million MRI scans utilize a gadolinium chelate to enhance contrast [6]. Other paramagnetic species, such as Mn(II) and iron oxides, are also under development [7].

The major disadvantages of these contrast agents are their high dosage necessary to perform a procedure, and, the weak relationship between pathological changes and enhanced contrast. Gadolinium-based agents generally require several grams of compound to be administered intravenously before a MRI procedure [8]. The toxicity of such large amounts of metal chelates made it not viable for patients with defective kidney function (Figure 1.1). More importantly, these agents enhance image contrast without specificity. Due to hydrophobicity of these Gd(III) chelates, tumors can be distinguished from healthy tissues as a consequence of their high vascular permeability. However, the confidence level of a bright or dark spot on MR images being a tumor is disappointingly low [9]. Besides, the requirement for high Gd concentrations makes it impossible to detect low concentrations of aberrant proteins or other molecular biomarkers [10].

1.1.4 Targeted MRI Contrast Agents (Biosensors)

Unlike general contrast agents, targeted imaging agents, also known as biosensors, aim at specific biological events such as elevated enzyme activity or cell surface receptor over-expression. In other words, such biosensors generate enhanced image contrast for specific targets of interest.

To achieve this, Gd(III) chelates and other supermolecular structures with bio-responsive moieties (e.g. enzyme inhibitors) have been developed [7, 9, 11–14]. After delivery and diffusion, these agents are selectively localized around the presence of targeted biomarkers, thereby generating elevated image contrast for certain biomarkers. While this specificity may limit their general applicability and market size, a targeted agent requires much smaller doses than general contrast agents, to achieve comparable contrast enhancement in regions of interest. Additionally, the identification and quantification of biomarkers provide much richer molecular information across different stages of diseases, particularly important for early-stage cancer detection.

1.2 ^{129}Xe in Magnetic Resonance

1.2.1 ^{129}Xe and Hyperpolarization

In addition to proton (^{1}H), other nuclei are also viable for MRI. A promising candidate for the development of MRI molecular imaging is hyperpolarized ^{129}Xe. This

isotope has a 26.5% abundance in Xe gas produced originally from liquid air, which is highly available. ^{129}Xe has $1/2$ nuclear spin, which gives a simple two-level energy layout that greatly simplifies NMR spectra. ^{129}Xe nuclei present a gyromagnetic ratio of 11.78 MHz $\cdot$ T^{-1} [15]; when applied at 1.5 T (a typical field strength for a clinical MRI scanner), it resonates at 17.7 MHz. Due to its large electron cloud of 54 electrons, mono-atomic ^{129}Xe has a 300 ppm chemical shift window in solvated and supermolecular forms; while it gives 5000 ppm chemical shift when transformed into solid state and covalently-bonded compounds. This large spectral range of xenon resonances has allowed multiple xenon species to be resolved in the frequency domain simultaneously. Though non-polar as an atom, the large, polarizable electron cloud provides a good water solubility of 5 mM under standard conditions, and it also allows Xe to interact with host molecules and proteins through dispersion forces [16, 17].

Given all these virtues, the reason that ^{129}Xe stands out from other nuclei is that it can be readily hyperpolarized, a feature also found in ^{3}He, ^{13}C, and a few other nuclei. Hyperpolarization is the nuclear spin polarization of a material far beyond thermal equilibrium conditions. This non-equilibrium spin distribution allows for large ($10^4 - 10^5$ fold) but one-time enhancement in NMR signal intensity. This significant but temporary increase has allowed for the ^{129}Xe NMR study of surfaces, zeolites, liquid crystalline phases, protein cavities, and, combustion [16, 18]. Xenon is most efficiently hyperpolarized through a process known as spin exchange optical

pumping (SEOP), which will be discussed in the next chapter. Without quadrupolar and covalent-bonding contributions to relaxation (Xe is a noble gas), ^{129}Xe is capable of exhibiting long lifetimes in the excited nuclear state (80-120 s T_1 when dissolved in aqueous solutions, and 4 h in natural isotopic abundance xenon ice at 77 K and 5000 G magnetic field), compared to other nuclei.

1.2.2 Developments Underway in ^{129}Xe MRI

As an additional channel of MRI, ^{129}Xe inherits most of the benefits of proton MRI while providing several extra features. As an exogenous MRI probe, ^{129}Xe enjoys zero background contrast, which is not possible with proton MRI. Unlike many other probes and contrast agents, xenon is minimally toxic, due to its inert chemical properties. *In vivo* ^{129}Xe MRI has been successfully applied to human lungs and mouse brains, and demonstrated high spatial resolution, high contrast, and minimal toxicity [19, 20]. In future clinical settings, ^{129}Xe images can be acquired simultaneously with proton images, and two images can be overlaid for analysis. This powerful technique provides complementary information of fine anatomical structures from proton and encoded chemical environments from xenon (Figure 1.3).

Targeted contrast agents (biosensors) for ^{129}Xe MRI are under development in our laboratory [12, 21–26] and elsewhere [27–30]. Biosensors have been synthesized and characterized for various biological events, including pH change [31], zinc concentration [32], enzyme activity [21], membrane fluidity [33], and over-expressed

proteins in cancer cells [22, 26] (Figure 1.2). Some of them demonstrated good cell uptake [25, 26, 29, 34]. With the wide chemical shift window described in the previous section, multiplexed imaging with different biosensors targeting orthogonal biomarkers is viable. For example, enzyme activity sensors when combined with pH sensing, can provide higher confidence for some diagnostic applications.

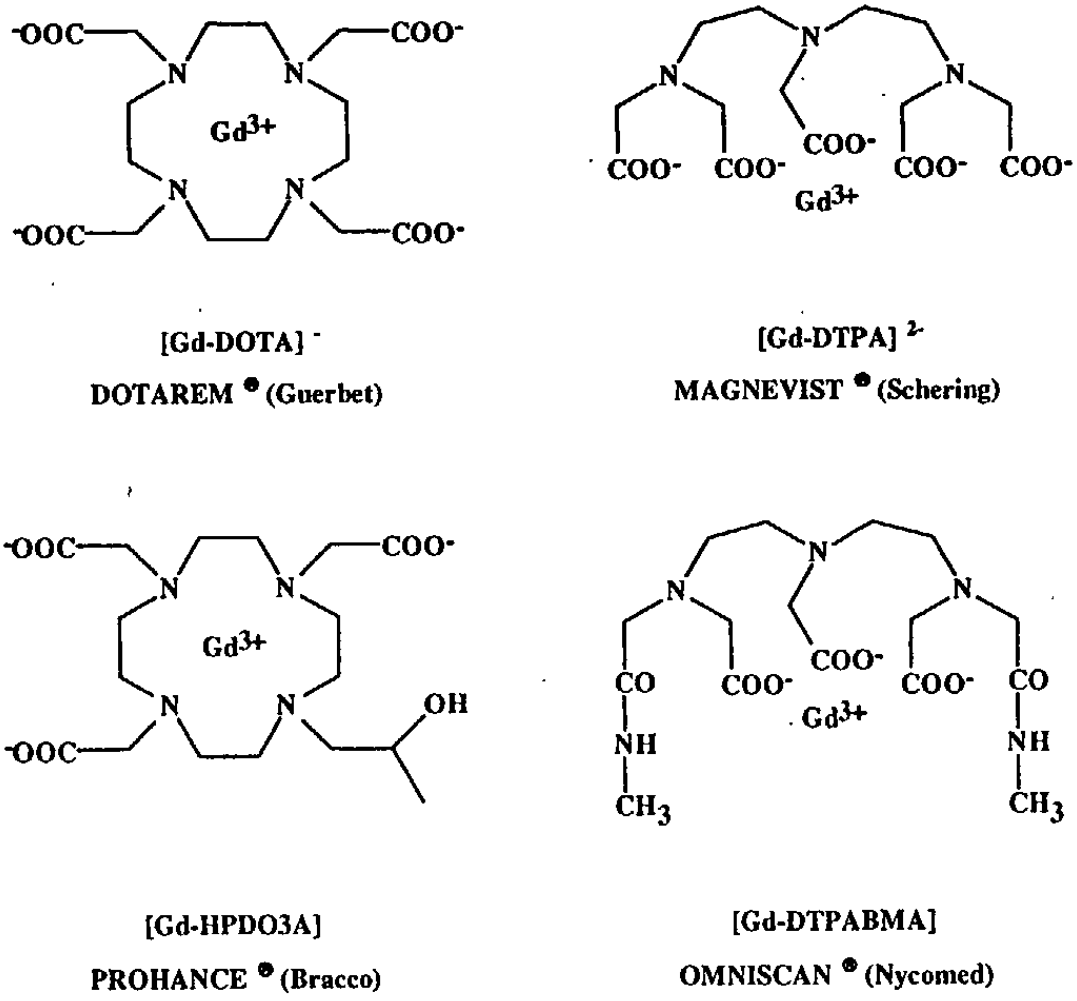

Figure 1.1: Gd(III)-based MRI contrast agents commonly employed in clinics. Figure from reference [35].

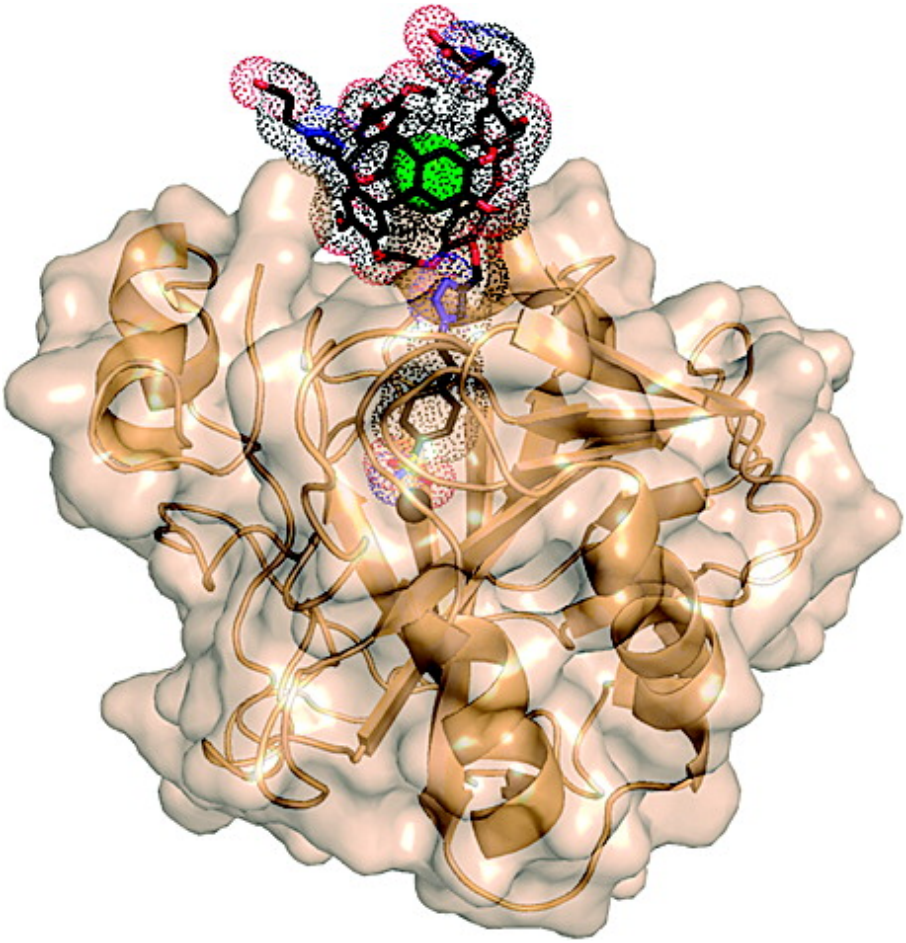

Figure 1.2: Crystal structure showing a Xe biosensor binding with carbonic anhydrase, from reference [22]. The Xe atom (green) is shown with a van der Waals diameter of 4.3 Å, the Zn^{2+} ion is gray, the CAII backbone and surface are tan, and the MoMo enantiomer of C8B is shown in black (carbon), red (oxygen), and blue (nitrogen), surrounded by its van der Waals surface (dots). C8B binds in the active site with the sulfonamidate anion coordinated to Zn^{2+}.

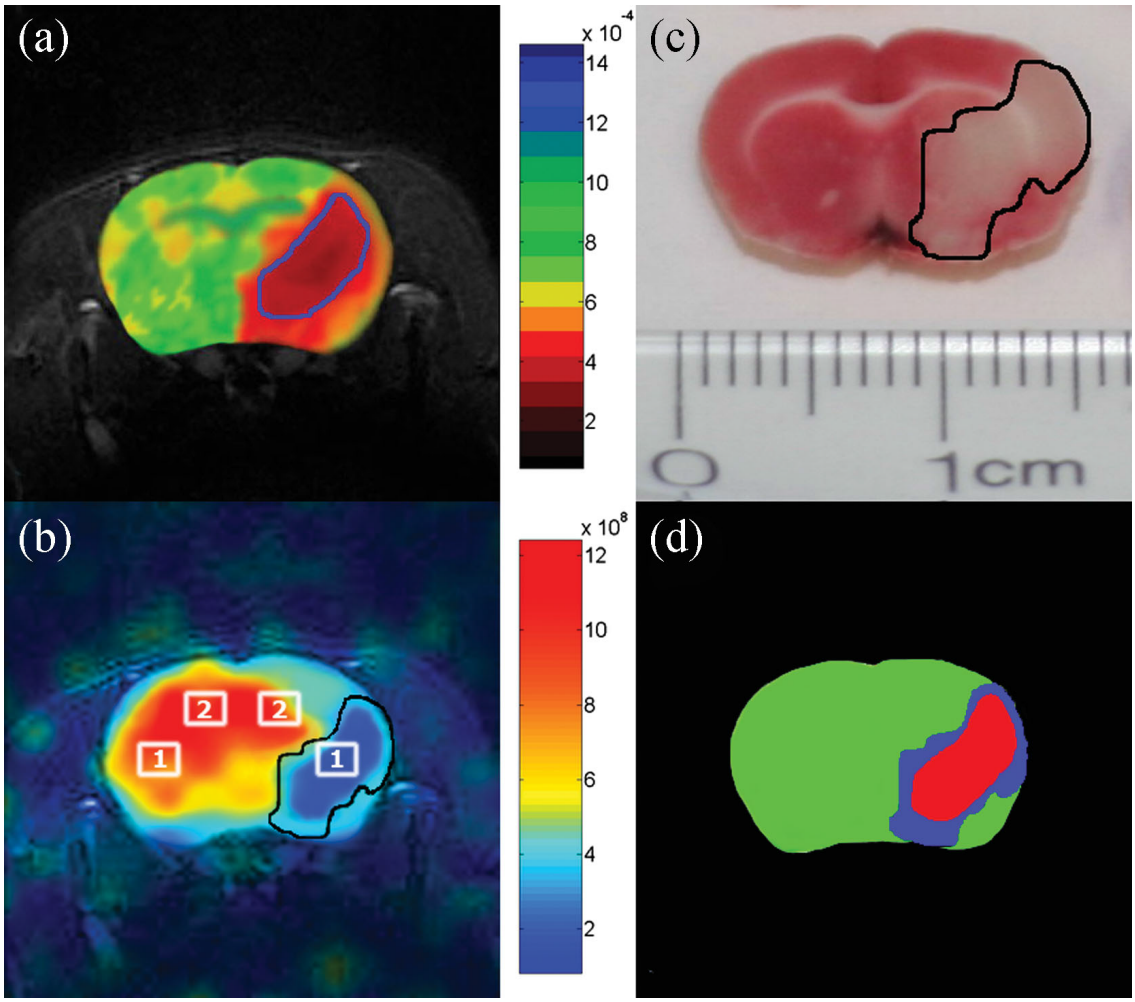

Figure 1.3: Multi-channel MRI images of a mouse brain with stroke, from reference [20]. a) Proton apparent diffusion coefficient (ADC) map image. The ischemic core (stroke center) is indicated by low ADC values (circled by a blue line). (b) Corresponding hyperpolarized ^{129}Xe chemical shift image (CSI). There is a large signal void in the ipsilesional (right) hemisphere. The regions of interest (ROIs) are labeled as follows: ROI1, core; ROI2, normal tissue. (c) Corresponding stained brain section of the same animal. (d) Tricolor map based on the above images. Green, red and blue represent nonischemic tissue, core and penumbra, respectively.

Chapter 2

Hyperpolarized (HP) ^{129}Xe NMR and Hyper-CEST

2.1 ^{129}Xe Hyperpolarization Through Optical Pumping

2.1.1 Nuclear Spin Polarization (Hyperpolarization)

Hyperpolarization is the nuclear spin polarization of a material far beyond thermal equilibrium conditions. The term "hyperpolarization" is invented to distinguish from "polarization" which conventionally relates to the electron cloud density redistribution due to surrounding electric fields. The prefix "hyper-" has two-fold implications: (1) like the term "hyperfine interaction" in molecular spectroscopy, it indicates the contribution of nuclear spin quantum number to atomic energy levels; (2) it involves significantly non-equilibrium population distributions of nuclear spin.

Hyperpolarization methods are commonly applied to nuclei such as ^{13}C, ^{129}Xe, and ^{3}He, where the polarization levels can be enhanced by a factor of $10^4 - 10^5$ above thermal equilibrium levels (see Figure 2.1). Various hyperpolarization techniques have been developed, including dynamic nuclear polarization (DNP) [36], spin-exchange optical pumping (SEOP) [37], and PASADENA (para-hydrogen and synthesis allow dramatically enhanced net alignment) [38]. Our method of choice is SEOP, which is highly efficient for ^{129}Xe.

2.1.2 Spin Transfer From Photons to ^{129}Xe Nuclei

The principle of spin exchange optical pumping(SEOP) for noble gas hyperpolarization was originally developed by Bouchiat and coworkers in the 1950s [39]. For SEOP we assume conditions of high gas pressures. The alkali-metal Rb is embedded in a high pressure gas mixture (64 psi, 4.3 atm) composed of 89% helium for buffering, 10% nitrogen for quenching, and 1% natural abundance xenon. In some cases a slightly higher percentage of xenon is employed. The high gas pressure considerably broadens the optical transitions of the alkali metal atoms, which makes the efficient use of broadband pumping lasers possible. In practice, broadband, high-power semiconductor lasers with typically 50 W of laser power are used, and their line width is 1-3 nm around the center. The N_2-quenching gas collisions prevent depolarization of the alkali-metal atoms caused by radiation trapping processes. Figure 2.2 shows a simplified picture of the mechanism involved in the two steps of polarization transfer: (1) the optical pumping process to polarize the Rb electron; (2) spin exchange between the Rb electron and the Xe nucleus.

Optical Pumping

In the optical pumping process, the photon spin ($s_z = 1$) of a circularly polarized laser beam (σ^+, uniform spin $I = 1$) is absorbed by a Rb atom. The frequency of the circularly polarized laser light is tuned to the D_1 transition of the Rb atoms (794.8 nm). Circularly polarized light is generated by passing the laser through a

beam expander and a $\lambda/4$ wave plate (Figure 2.3).

The selective optical transition from the $^5S_{1/2}$ ground state to the $^5P_{1/2}$ ($J = 1/2, m_J = +1/2$) excited state depopulates only the $m_S = -1/2$ ground state with an optical pumping rate (Figure 2.2), because for right-handed circularly polarized light ($s_z = +1$), no transition is allowed from the $m_S = +1/2$ ground state to the two excited states $m_J = +1/2$ or $m_J = -1/2$. This follows from the conservation of angular momentum (selection rule), where the absorption of the circularly polarized photon spin ($s_z = +1$) only changes the orbital angular momentum ($\Delta L = +1$) of the Rb atom but cannot affect the intrinsic electron spin orientation ($\Delta S = 0$). After the $m_J = +1/2$ excited state is selectively populated with the rate R, frequent collisions with ^{4}He atoms mix the excited $^5P_{1/2}$ state into an incoherent superposition of $m_J = +1/2$ and $m_J = -1/2$ states. Therefore the electron spin order of the excited state is completely destroyed.

The collisional rate for these J-randomizing ^{4}He collisions at 10 bar gas pressure is $1/T_J \approx 1 \times 10^{11}$ s^{-1}. Therefore, during an average of every 10 ps, one ^{4}He atom collides with the excited Rb atom [37]. The J-randomization leads to an equal population of the two excited states. Subsequent quenching collisions with N_2 molecules transport the excited state non-radiatively to the ground state. The quenching collisional rate for typical N_2 pressures of 0.1-1 bar is about $1/T_Q \approx 1 \times 10^9$ s^{-1}. This corresponds to an average lifetime of <1 ns which is much shorter than the natural excited state life time of about 30 ns. Therefore, only a small

fraction of the excited Rb atoms ($\sim$ 1%) can decay radiatively through emission of a fluorescence photon. The repopulation and depopulation pumping produces a ground state electron spin polarization, which is destroyed through collisions with Xe, N_2 or He atoms. An important consequence for spin exchange optical pumping under high pressure conditions is that the passage through the excited state, (depopulation pumping, J-randomizing and N_2 quenching collisions) and most of the spin polarization destroying relaxation processes are short-lived with respect to the nuclear spin.

Spin Exchange

The second part of Figure 2.2 shows the transfer of spin polarization from the Rb-electron spin to the nuclear spin of the Xe atom. Under high pressure conditions, there are mainly binary collisions between Rb and Xe atoms in the gas phase, which leads to short-lived Rb-Xe complexes. The Rb-electron spin of the transient Rb-Xe complex has a non-zero probability of being at the position of the Xe-nuclear spin. This is the physical origin for the isotropic hyperfine coupling, also called Fermi contact interaction. The form of the coupling indicates that the transfer is mediated by flip-flop processes between the Rb-electron spin and the Xe-nuclear spin. When the gas pressure is low, the main contribution for the polarization transfer comes from long-lived van der Waals complexes. This phenomenon was intensively studied by Happer et al. [40].

As the electronic and nuclear spins are polarized on a much longer timescale than photon absorption, J-randomization, and collision quenching, the steady-state approximation for spin populations leads to a simplified description of the spin exchange optical pumping process, which features a "spin temperature" parameter. After the Rb valence electron is spin polarized and aligned with the outer magnetic field, it displays a low "spin temperature" and serves as a "cold" spin reservoir. Xe nuclei are in close contact with this reservoir and their spin temperature is "cooled down" (see Figure 2.2), thereby achieving xenon nuclear spin polarization. This process can be operated under continuous xenon gas flow (Figure 2.3).

2.1.3 Cryogenic Separation of Pure HP Xe

Given enough laser power to maintain the Rb electron polarization, the gas mixture (N_2, He, Xe) can be flowed through the optical pumping glass cell continuously (Figure 2.3). To utilize this feature and attain large quantities of pure HP Xe, a cryogenic separation technique has been developed [41, 42]. As the gas stream (N_2, He, Rb vapor, HP Xe) flows out of the optical pumping chamber, the Rb vapor condenses on the inner surface of the tubing and other inert gases (containing HP Xe) are passed through. Further down the gas line a cold finger at 77 K traps Xe as a solid and accumulates Xe as "ice" (melting point 161.25 K) during the time of operation. Other gas components flow out of the setup exhaust. ^{129}Xe retains its polarization during freezing [41] and the relaxation time of solid ^{129}Xe is about 3 h

at 77 K [43]. The spin lattice relaxation time T_1 of the solid-phase ^{129}Xe constrains the duration of the accumulation to be within a few hours. After an accumulation time t_a (typically 20-40 min in practice), the remaining polarization of the ^{129}Xe ice is:

$$P_{Xe}(t_a) = P_{Xe}(0)(T_1/t_a)(1 - e^{-t_a/T_1}) \tag{2.1.1}$$

where $P_{Xe}(0)$ is the polarization of the ^{129}Xe exiting the optical pumping chamber [42]. The final polarization of the ^{129}Xe gas for a desired volume can be maximized by appropriate choice of gas flow rate and accumulation time. After accumulating sufficient hyperpolarized ^{129}Xe ice, the gas line is closed and evacuated to less than 5 Pa. Then HP Xe gas is released by quickly warming the xenon ice, and sealed in a NMR tube with liquid sample. The measured final polarization level is 10-15% at a volume of 0.1 L.

2.2 Hyperpolarized ^{129}Xe Chemical Exchange Saturation Transfer (Hyper-CEST) NMR

2.2.1 Chemical Exchange Saturation Transfer (CEST) in Proton MRI

As discussed in the introduction, the new landscape of molecular imaging applications prompts the search for new paradigms in the design of MRI contrast agents. A general insight deals with the exploitation of frequency, the key parameter of the NMR phenomenon. The possibility of designing frequency-encoded MRI protocols based on controlled magnetization transfer appears a very interesting perspective in terms of sensitivity enhancement. In the last decade, there has been a surge in NMR exchange applications due to the utilization of the highly controllable saturation transfer, which can be combined with proton exchanges between different chemical environments.

The first to demonstrate that exchange between labile protons of low-concentration solutes and water protons provides a sensitivity enhancement scheme were Balaban et al., who named this new MRI contrast mechanism chemical exchange dependent saturation transfer (CEST) [44]. In their experiments, barbituric acid and 5,6-dihydrouracil, both conducting proton exchanges with water, were selected as the sites for RF pulse saturation (see Figure 2.4). During CEST experiments, the proton spins in these compounds got saturated in a frequency-specific way by radio

frequency (RF) irradiation. As a result, spin population inversion in the selected frequency is transferred into the pool of water protons, through chemical exchange processes that are faster than spin relaxation. This process leads to a reduction of water proton signal intensity. Reporting the molecular information associated indirectly with the exchanging species, readouts of CEST experiments are the water signal intensities at different saturation frequencies and RF pulse strengths used. As the water signal is usually much stronger than any other proton species under observation, measuring the signal reduction instead of directly measuring the target proton species provides as much as 500,000-fold sensitivity enhancement [45].

The theoretical aspect of CEST generally aims at the description and quantification of the effects, and design and optimization of experimental schemes. For a spin system without scalar couplings, chemical exchange processes are commonly described by modified Bloch equations including exchange terms, sometimes called the Bloch-McConnell equations [46]. It is difficult to obtain the exact analytical solutions of these equations, even for the case of two-site exchange. Therefore, most investigators endeavor to derive concise analytical solutions of the problem using some reasonable assumptions.

2.2.2 Hyper-CEST with ^{129}Xe

CEST can also be applied to HP ^{129}Xe to observe chemical exchange sites indirectly, producing the acronym "Hyper-CEST". With HP ^{129}Xe, Hyper-CEST solves both

the contrast and the intensity problem for MRI. In Figure 2.5, a typical spectrum of ^{129}Xe biosensor is shown. Due to the low concentration of biosensors (∼100 µM), and the high concentration of dissolved ^{129}Xe (∼15 mM); the biosensor signal, which is also used in imaging, is 1000 times weaker. In direct detection, most Xe atoms are not contributing to the final imaging contrast, and the biosensor signal is not strong enough for more demanding applications. With Hyper-CEST, the biosensor signal can be analyzed indirectly via generating and observing changes in the Xe(solvent) signal, through saturation transfer mediated by chemical exchange. By tuning the saturation frequency, very clear signal contrast for identification of the biosensor can be generated at picomolar concentration, which will be shown in the following chapters.

2.2.3 Hyper-CEST Radio-frequency Pulse Sequence

In a NMR experiment, selective saturation is accomplished by radio-frequency (RF) pulses. A pulse sequence used in most Hyper-CEST experiments is shown in Figure 2.6. Multiple (L6) selective saturation 180° RF pulses (sp6) were irradiated at the Xe@host resonance frequency; meanwhile, HP Xe and depolarized Xe were dynamically exchanging with the host sites. Time-delay parameters (d1, d12) in the pulse sequence are used for coordinating the saturation cycle into the Xe exchange time frame. As a result, overall Xe depolarization was accumulated in the aqueous sample, and detected by another 90° hard excitation pulse (p1). Without Hyper-

CEST, HP Xe goes through depolarization exponentially by a time constant close to the Xe relaxation constant T_1 ($\sim$70 s when Xe is dissolved in water). For contrast, in the Hyper-CEST experiments with "depolarization catalyst" and "on-resonance" saturation transfer, the depolarization rates were observed to be much faster.

2.2.4 HP Xe Gas Delivery Control Device

To describe a biosensor's Hyper-CEST behaviors at different saturation frequencies and/or saturation powers, a series of Hyper-CEST data with a consistent Xe signal intensity are required, for comparison in the exchange experiments. However, due to the evanescent nature of ^{129}Xe hyperpolarization and the fast-changing hyperpolarization level, this has been impossible for batch-mode Xe delivery setups. On the other hand, for most continuous-flow gas delivery setups, turbulence and bubbles will affect magnetic field homogeneity in NMR samples.

These issues are solved by a home-built semi-continuous flow delivery setup for HP Xe (Figure 2.7). Freshly hyperpolarized gas mixture (89% helium, 10% nitrogen, and 1% natural abundance xenon), with a pressure of 66.7 psi, was guided from the hyperpolarizer to the NMR tube. The gas mixture was bubbled through the liquid sample by a capillary dispenser and the exhaust is guided to air. The flow rate is controlled by a pinch valve near the exhaust. After 20 seconds of bubbling, gas flow is stopped by two solenoid valves, controlled by a programmable relay from the computer. Immediately after flow is stopped, the Hyper-CEST pulse sequence

is started and NMR data are acquired. By the time acquisition is finished, gas flow is started again and fresh Xe is replenished through bubbling. With these steps repeated, Hyper-CEST experiments can be done with a near-constant starting Xe signal intensity.

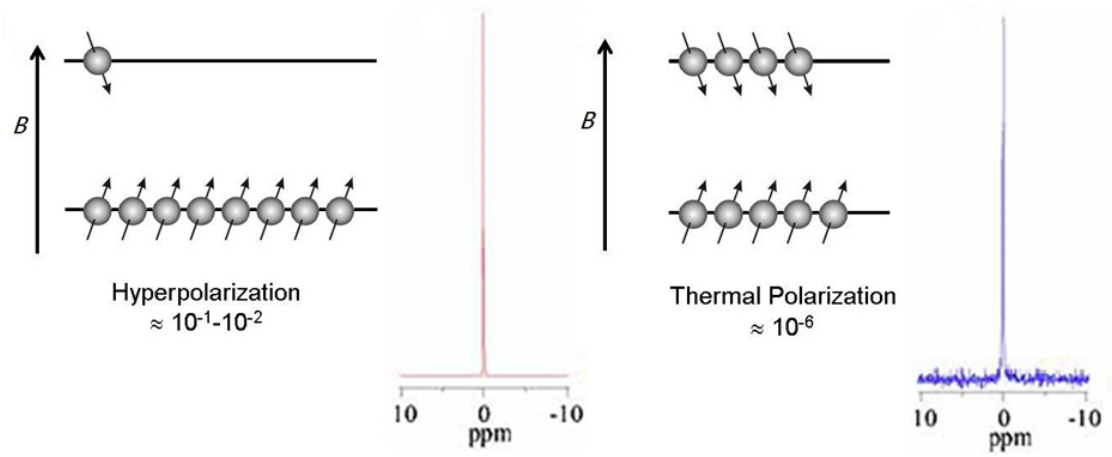

Figure 2.1: Comparison between thermally polarized and hyperpolarized NMR spectra. The population distributions on the spin energy levels are exaggerated for clarity. The signal/noise ratio for the hyperpolarized sample is 10^4-fold higher compared to the thermally polarized sample, given the same radio-frequency excitation.

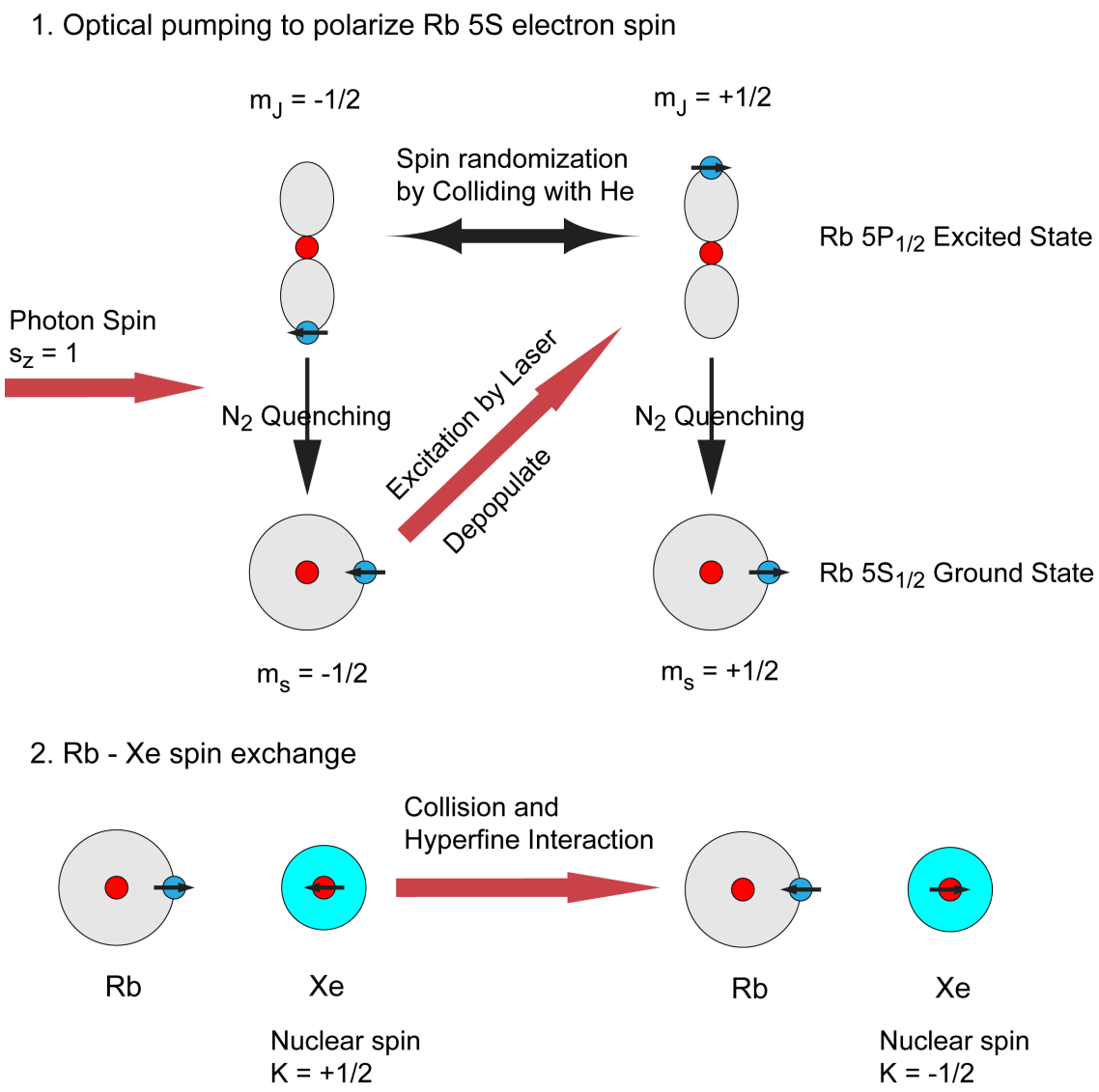

Figure 2.2: Two-step spin transfer in Spin-Exchange Optical Pumping (SEOP). First, spin angular momentum is accumulated in Rb valence electrons. In the following step, Xe nuclei achieve hyperpolarization through collision and hyperfine interaction.

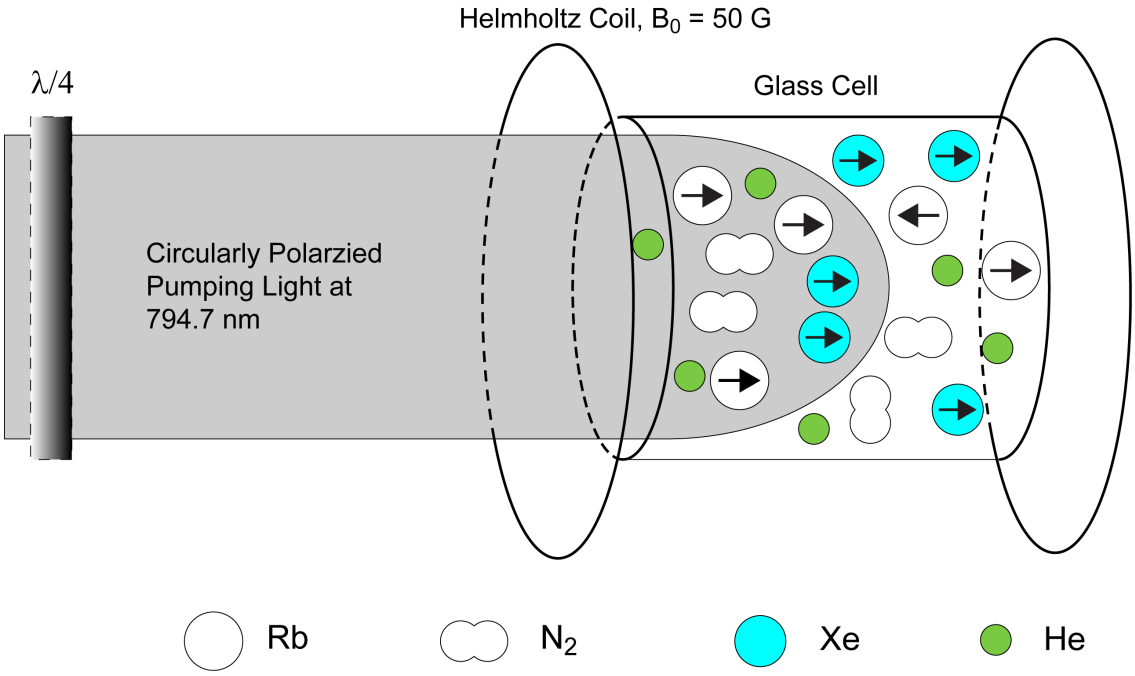

Figure 2.3: Spin-Exchange Optical Pumping (SEOP) setup. Spin angular momentum is transferred from circularly polarized photons (spin I = 1, 100%) to Xe nuclei through excited Rb. Nitrogen gas is used to quench exited state Rb quickly to facilitate spin transfer.

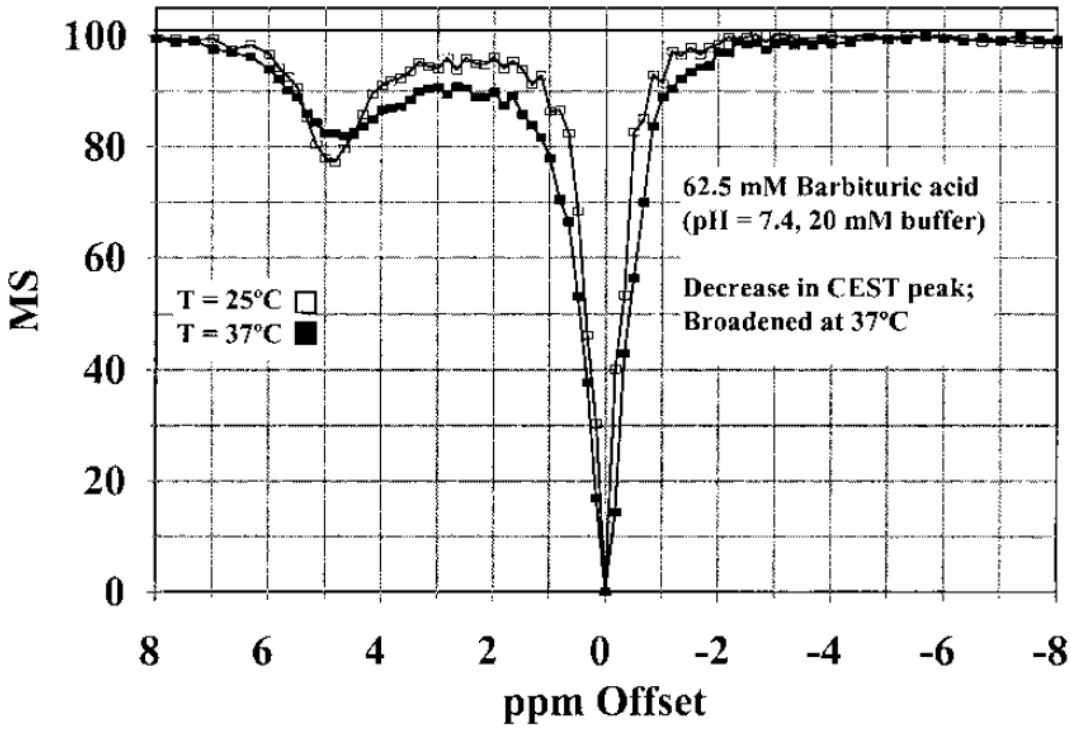

Figure 2.4: Temperature-dependent CEST spectra of barbituric acid solution (62.5 mM, 20 mM phosphate buffer), pH 7.4, from reference [44].

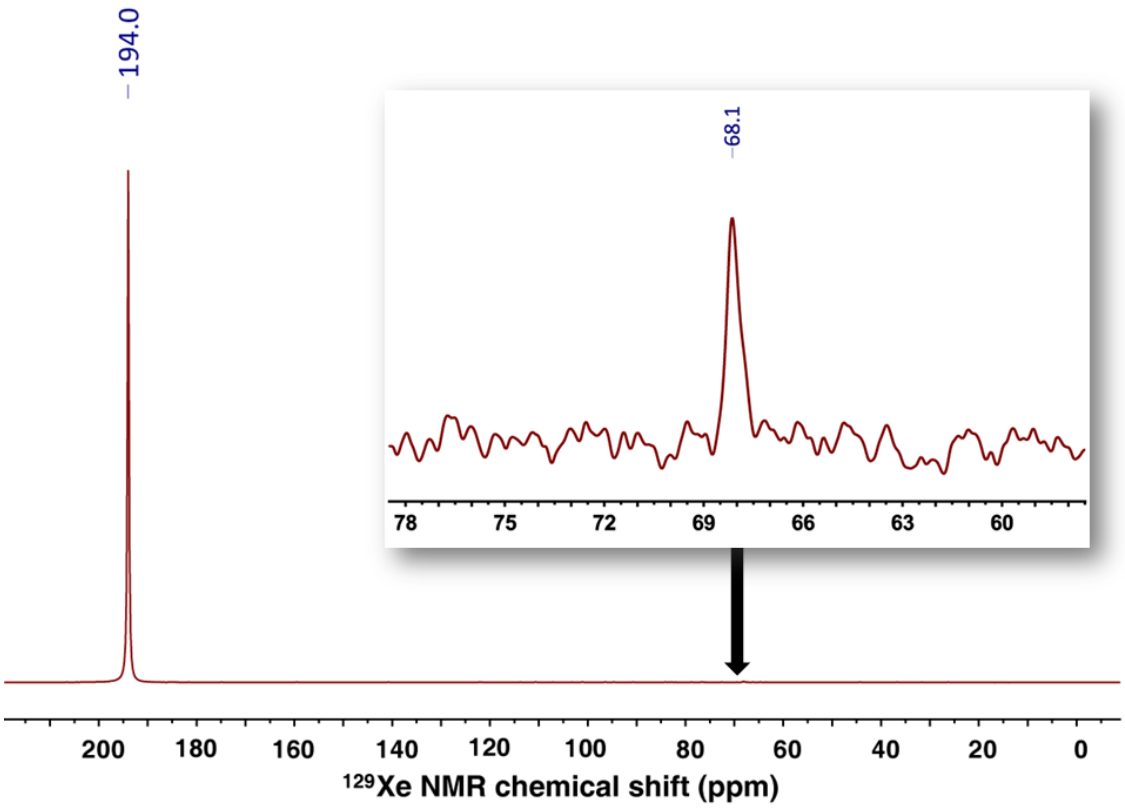

Figure 2.5: Directly detected ^{129}Xe spectrum of triacetic acid cryptophane-A derivative (TAAC). Xe dissolved in water appears at 194 ppm. Inset zooms in at the Xe@TAAC signal at 68.1 ppm.

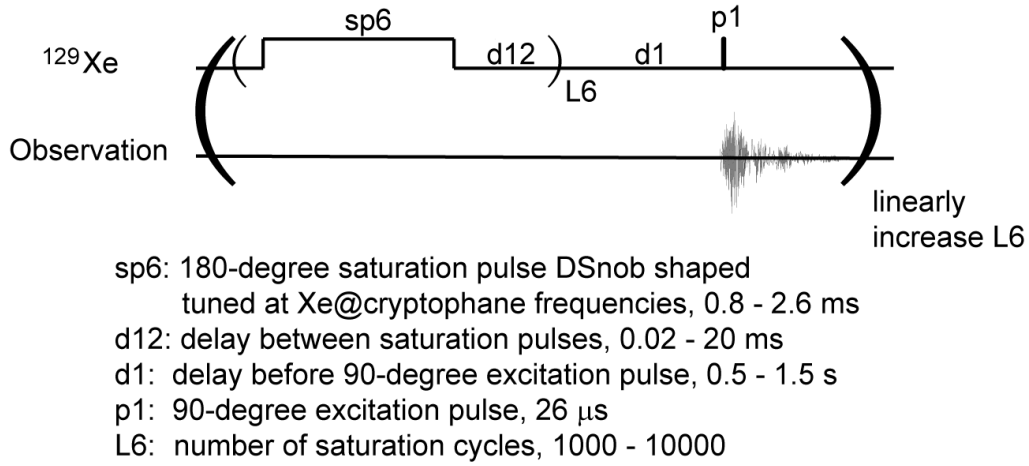

Figure 2.6: Hyper-CEST pulse sequence diagram, with parameters provided for in-house 10 mm PABBO probe. Different values were chosen considering biosensor concentration, sample temperature, HP Xe flow rate. Based on a recent saturation transfer optimization study [47], saturation pulse is DSnob-shaped to enhance power efficiency.

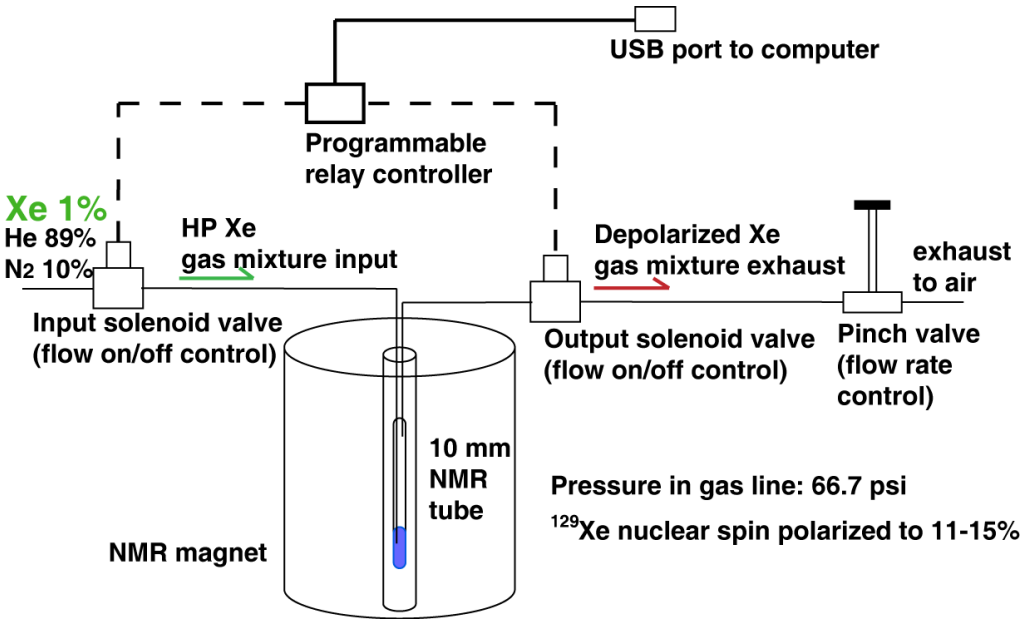

Figure 2.7: HP Xe gas mixture continuous-flow delivery setup. Typically the flow rate ranges between 0.6 and 0.8 standard liters per minute (SLM). The sample solution is saturated by HP ^{129}Xe after continuously running the gas line for 20 s, which is confirmed by monitoring ^{129}Xe signal intensity using small flip-angle pulses.

Chapter 3

HP ^{129}Xe NMR of Various Cryptophane-A Derivatives

3.1 Cryptophanes as Effective Xe Binders

Due to its small size (r = 2.17 Å), lipophilic character, and polarizability, Xe is capable of crossing cell membranes, and has been detected in hydrophobic pockets of proteins [48–51]. Xenon is also known to bind to a variety of synthetic host molecules with hydrophobic cores such as α-cyclodextrin [52], cucurbituril [53], hemi-carcerands [54], and a large portion of the cryptophane family [55]. Cryptophane-A and its variants have been the subject of more xenon binding studies than any other synthetic molecule. As shown in Figure 3.1, cryptophane-A is composed of two cyclo-triveratrylene (CTV) caps linked by three dioxyethylene bridges, thereby enclosing a void space in the center. Cryptophane-A is chiral with a D_3 axis of symmetry. For further applications in this report, only the *anti* isomer is used for biosensors [55], as the corresponding syn isomer (with a mirror plane and C_3 symmetry axis) is not formed under most synthetic conditions. Some of the best known Xe binders (Figure 3.2) [24, 56] are derived from cryptophane-A, and biosensors exploiting these properties have been synthesized by attaching different targeting/sensing moieties to these cryptophanes.

3.1.1 Water-soluble Cryptophanes

As cryptophane-A is intrinsically hydrophobic, members of the Dmochowski laboratory have worked to increase its water solubility by substituting the methyl groups in one of the two CTV caps, with acetic acid, triazole-propionic acid, and

triazole-ethylamine groups (see Figure 3.2). The tris-amine cryptophane currently has the highest affinity of known Xe host molecules at room temperature in aqueous solution, which is shown in table 3.1 [24, 56].

Table 3.1: Xe binding affinities for water-soluble cryptophanes. Described as binding constant (K_A) and dissociation constant (K_D)

Cryptophane derivatives	K_A	K_D
Tris(acetic acid) cryptophane (TAAC)	33 000 ± 2000 M^{-1}	30 ± 2 µM
Tris(triazole ethylamine) cryptophane (TTEC)	42 000 ± 2000 M^{-1}	24 ± 1 µM
Tris(triazole propionic acid) cryptophane (TTPC)	17 000 ± 2000 M^{-1}	58 ± 7 µM

3.1.2 Tri-propargyl Cryptophane and Click-reaction

To facilitate the attachment of functional moieties to cryptophanes, a template cryptophane named tri-propargyl cryptophane was previously synthesized by Aru Hill in our lab (see Figure 3.2, details can be found in reference [57]). In this cryptophane, all methyl groups on one cap of cryptophane-A are replaced by propargyl groups, which allows the well-used [3+2] cyclo-addition "click reaction" [58]. In the following sections, biosensors derived from this template cryptophane and their ^{129}Xe NMR behaviors will be discussed.

3.2 Carbonic Anhydrase Biosensors

3.2.1 Introduction

Human carbonic anhydrase (CA) is involved in many physiological processes such as carbon dioxide transport and pH homeostasis in tissue [59]. However, some CAs also appear to have detrimental effects on human health: For example, CA I, II, and other isozymes were shown to be present and probably involved in the formation of certain tumors and polycystic kidney disease [60, 61]. Particularly, upregulated CA IX and XII levels are found in various human cancer cells and can be used as a biomarker for cancer diagnosis [62, 63]. Thus, the development of isozyme-specific CA biosensors holds considerable promise for cancer imaging. Numerous crystal structures of CA-inhibitor complexes are available to guide biosensor development, and CA II in particular has served as a successful model system for rational drug design [64–66].

In previous works from our lab [22, 67, 68], xenon biosensors targeting CA were synthesized and characterized. The strategy for constructing protein-targeted xenon biosensors is to covalently attach a targeting ligand to the cryptophane. Through protein-specific binding of biosensors to proteins, the cryptophane-associated Xe atom experiences a different magnetic environment that depends on whether the encapsulating biosensor is bound to protein, and what kind of protein is bound to the biosensor. In several published studies, CA has been viewed as a model system

for understanding protein-ligand interactions [64].

3.2.2 Distance Variations

^{129}Xe NMR studies of peptido-biotin cryptophane biosensors have shown that decreasing the linker length to the biotin ligand increases the NMR signal change (upon avidin binding) in chemical shift as well as the line width [28]. To further study the effect of linker length on the ^{129}Xe NMR signals, biosensors for CA were developed by attaching azido-benzenesulfonamide of different linker lengths to the tri-propargyl cryptophane, through [3+2] cyclo-addition as discussed in the previous section. More, to increase the biosensors' water solubility, and to avoid the appendage of additional stereo-centers to the cryptophane core, two propionic acid groups were also "clicked-on" (see Figure 3.4).

In Figure 3.5, a series of HP ^{129}Xe NMR spectra is shown for biosensors with different linker length (6-8 bonds) binding to CA I and II. Detailed discussion can be found in reference [22]. Three important findings can be summarized: (1) biosensors of different linker lengths display distinguishable chemical shift differences, which proves though not covalently bonded, Xe can still report its chemical environment due to its high electron polarizability; (2) multiple "bound" signals for biosensor-protein complexes were observed, indicating multiple interaction paradigms; (3) different isozymes of the same protein can be distinguished by ^{129}Xe biosensors.

3.2.3 Stereochemistry

In a previous study of biotinylated biosensor targeting steptavidin, attaching a peptide to the chiral cryptophane created diastereomers, which increased the number of peaks in the ^{129}Xe spectrum, and correspondingly decreased the signal-to-noise ratio. Computational studies have helped to assign the various NMR resonances to their respective diastereomers [69]. However, the tetrameric nature of avidin can further complicate the ^{129}Xe NMR spectrum [28].

To investigate whether enantiomers of the same biosensor behave differently in the biosensor-CA binding event, stereopure C7B biosensor was synthesized in the Dmochowski lab [68]. HP ^{129}Xe NMR spectra were acquired with different biosensor to protein ratios (see Figure 3.7). Both (+)−C7B and (−)−C7B have the same NMR signal when "free" in solution. When bound to wild-type CA II, (+)−C7B shows sharp "bound" peaks indicating relatively less constrained interaction, between biosensor and protein. On the other hand, (−)−C7B shows broad "bound" peaks, which is attributed to more rigid interactions between biosensor and protein and therefore increased the biosensor-protein complex NMR relaxation time. More, the most down-field shifted "bound" peak, also observed in Figure 3.5, is only present for (+)−C7B. These interesting phenomenon confirmed part of our hypothesis that the two enantiomers behave differently in ^{129}Xe NMR; however, the origin of the two "bound" peaks was not deconvolved.

3.2.4 Binding Sites

Further efforts were made to resolve the origin of the two "bound" peaks for biosensor-CA II complexes (see Figure 3.5). It has been shown that CA II contains two binding sites for the sulfonamide group, one near the enzyme active site and the other close to the enzyme active site entrance [59]. Mutants of CA II were made by changing single amino acids near each of the two sites. D19L and H94R mutants were designed and prepared by our collaborators from the Christianson group. These mutations aimed at geometrically blocking the entrance of sulfonamide groups from entering the binding sites, and unpublished protein structures from crystal structures have proved their validity. Upon binding to C8B at a 1:1 ratio, each of the mutants presents only one "bound" signal on the ^{129}Xe NMR spectra. These results agree well with previous studies with the wild-type CA II (Figure 3.5), which proves the two-site model can be applied for assigning ^{129}Xe NMR signal of biosensor-protein complexes.

In summary, with the advancement of HP ^{129}Xe NMR techniques, higher resolution NMR spectra for biosensor-protein bound complexes can be acquired, which provides the opportunity to further understand the biosensor targeting interaction. Linker lengths, stereochemistry, and binding-site alterations all contributed in the variations of ^{129}Xe NMR signals. With the study of the CA-biosensor model system, molecular information can be acquired in possible MRI studies that utilize the highly sensitive ^{129}Xe chemical shift changes.

3.3 Integrin Biosensor

Peptide-modified cryptophane enables sensitive detection of protein biomarkers using HP ^{129}Xe NMR spectroscopy. As $\alpha_v\beta_3$ integrin receptor is overexpressed in many human cancers, it can serve as a potential biomarker for HP ^{129}Xe MRI. Targeting and delivery of cryptophane to cells expressing $\alpha_v\beta_3$ integrin receptor has been achieved [26]. In the previous work, cryptophane was functionalized with cyclic RGDyK peptide and Alexa Fluor 488 dye, and cellular internalization was monitored by confocal laser scanning microscopy. The peptide-cryptophane conjugate was determined to be nontoxic in normal human lung fibroblasts by MTT assay at micromolar concentrations (typical for hyperpolarized ^{129}Xe NMR biosensing experiments). Flow cytometry revealed 4-fold higher cellular internalization in cancer cells overexpressing integrin receptor compared to normal cells. Nanomolar inhibitory concentrations (IC_{50} = 20-30 nM) were measured for cryptophane biosensor against vitronectin binding to $\alpha_v\beta_3$ integrin and fibrinogen binding to $\alpha_{IIb}\beta_3$ integrin.

To test the biosensor's viability for HP ^{129}Xe MRI, NMR spectra for various supermolecular complexes are acquired. In Figure 3.10(b), biosensor (50 µM) and $\alpha_{IIb}\beta_3$ integrin (16 µM) were mixed in Tris buffer (1 mM, pH 7.2) with 30% glycerol and 0.1% Triton X-100. The $\alpha_{IIb}\beta_3$ integrin was chosen instead of $\alpha_v\beta_3$ integrin, due to the relative ease of isolating and lower cost of purchasing milligram quantities of this protein. Keeping the $\alpha_{IIb}\beta_3$ integrin membrane protein in buffer solution

required addition of glycerol and Triton X-100, and glycerol also mitigated foaming while introducing Xe. "Free" cryptophane gave a ^{129}Xe NMR peak at 67.1 ppm, while "bound" cryptophane appeared at 71.2 ppm, representing a 4.1 ppm down-field shift (see Figure 3.10(b)). Signal-to-noise ratio for the single "bound" cryptophane-protein peak was ∼3:1. With the racemic mixture of biosensors, protein binding results in diastereomers, which in some cases can produce multiple "bound" ^{129}Xe NMR peaks [22, 69]. We have seen single "bound" peaks previously in cases where the cryptophane enantiomers are constrained near the protein target surface, and the xenon by chance senses the environment identically. The short alkyl spacer (between the triazole and c[RGDyK] peptide in the integrin biosensor) may similarly constrain both cryptophane biosensor racemates at the integrin receptor, creating effectively one xenon binding site. Alternatively, a second peak corresponding to the other diastereomer may reside under the "free" peak (∼67 ppm).

This 4.1 ppm change in chemical shift is comparable to our previous carbonic anhydrase biosensor work (3.0-7.5 ppm) [22] and a biosensor optimization study with biotin-avidin (3-4 ppm) [70]. Considerably smaller ^{129}Xe NMR chemical shifts were observed in two related protein-binding studies (biotin-avidin, ∼1 ppm [27]; major histocompatibility complex, ∼1 ppm [71]). To make a competition assay (Figure 3.10(c)), c[RGDyK] (100 µM) was added to a fresh solution (1 mM Tris buffer, pH 7.2; 30% glycerol and 0.1% Triton X) containing biosensor (100 µM)

and $\alpha_{\mathrm{IIb}}\beta_3$ integrin (20 µM). Here "free" cryptophane gave the same ^{129}Xe NMR chemical shift, and no "bound" cryptophane was detected, which indicated that the peptide blocked biosensor from binding to $\alpha_{\mathrm{IIb}}\beta_3$ integrin. The disappearance of the smaller "bound" peak after addition of the competing peptide further confirmed that the spectral change observed upon addition of $\alpha_{\mathrm{IIb}}\beta_3$ is due to protein binding by the cryptophane biosensor.

3.4 pH Sensor

A recent study by lab coworker Brittany Riggle focuses on developing a pH biosensor based on the tri-propargyl cryptophane. pH variation is often found in the extracellular environment of tumor cells, and various tumors are demonstrated to acidify their micro-environment to levels between 6.2-6.9 from pH levels of 7.3-7.4, so as to facilitate cancer metabolism and metastasis [72,73]. Multiple attempts have been made to monitor extracellular pH using MRI contrast agents [74–78]. This work aims at generating a pH-biosensor relevant to *in vivo* pH ranges, and the synthetically derived EALA peptide was selected. EALA peptide is a 30-mer peptide made up mostly of glutamic acid, alanine, leucine, alanine repeats; in reaction to a reduction in pH from 7 to 5, it undergoes a conformational change from random coil to α-helix [79]. The amphipathic α-helix binds bilayer membranes; the nature of such interactions are dependent on the physiological environment and the chemical make-up of the membrane but this feature may prove to have interesting uses

in biological studies [80]. After adding an azide group, the peptide was attached to the tri-propargyl cryptophane by [3+2] azide-alkyne cycloaddition. Additional propionic acid was also attached to the cryptophane by the same method 3.11.

To show the sensitivity of ^{129}Xe NMR chemical shift in response to pH change, two physiologically relevant pH values (7.5, 6.5) were selected to measure the chemical shift changes on ^{129}Xe NMR. At pH 7.5, only one peak was shown, as the attached EALA peptide was in 100% disordered state. When buffer pH was changed to 6.5, an additional peak was also observed, which indicate the peptide underwent partial change into α-helix 3.12, and both the disordered and alpha-helical conformations were present in solution. This proves even though Xe is encapsulated inside a cryptophane, it can still respond to different isomers of large proteins shown in the last example, as well as a small peptide conformational change.

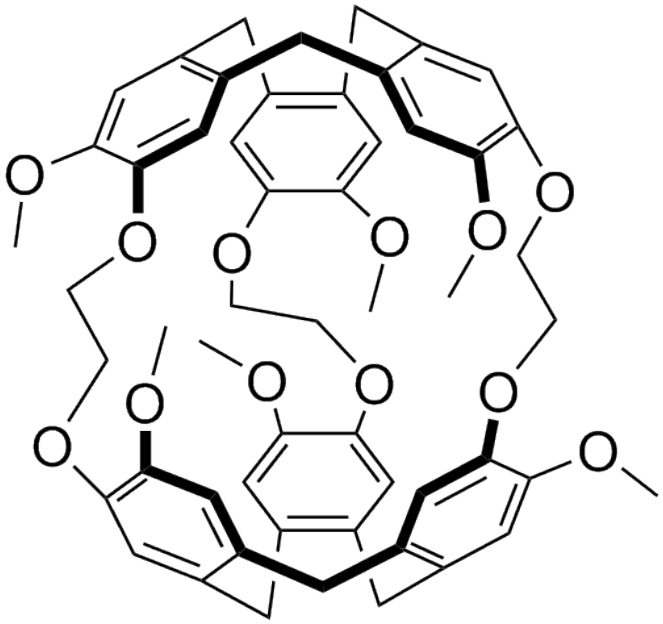

Figure 3.1: Structure of cryptophane-A. Cryptophane-A consists of two cyclotriveratrylene (CTV) caps joined by ethylene ether bridges. The near-spherical molecule has a diameter of 1 nm and an internal volume of approximately 95 $Å^3$.

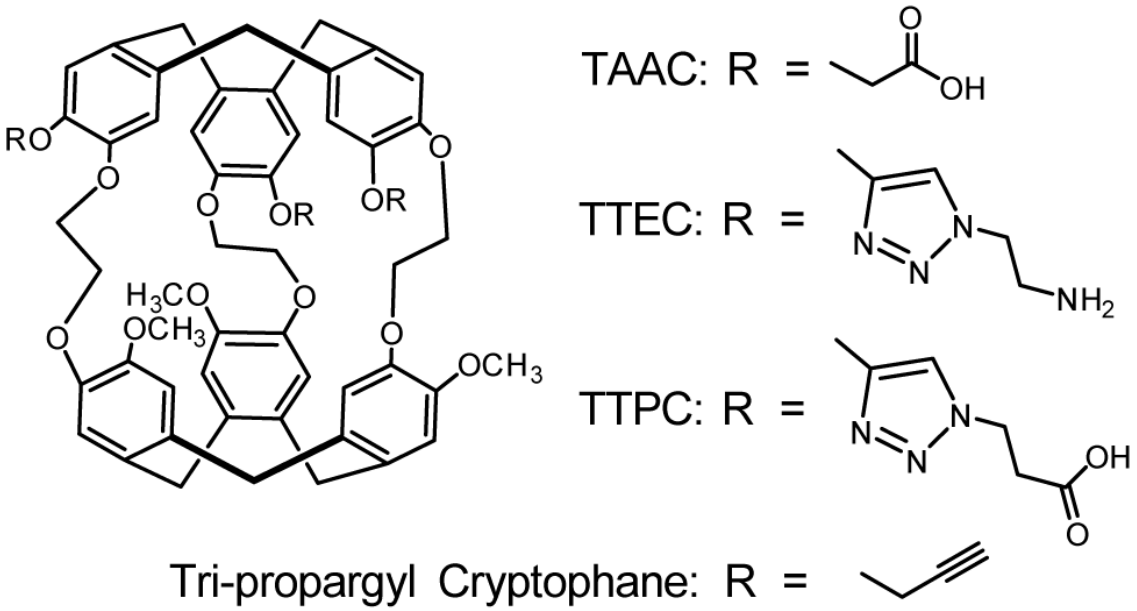

Figure 3.2: Structure of tris(triazole propionic acid) cryptophane (TTPC), tris(acetic acid) cryptophane-A (TAAC), tris(acetic acid) cryptophane (TTPC), tris-(triazole ethylamine) cryptophane (TTEC), and tri-propargyl cryptophane

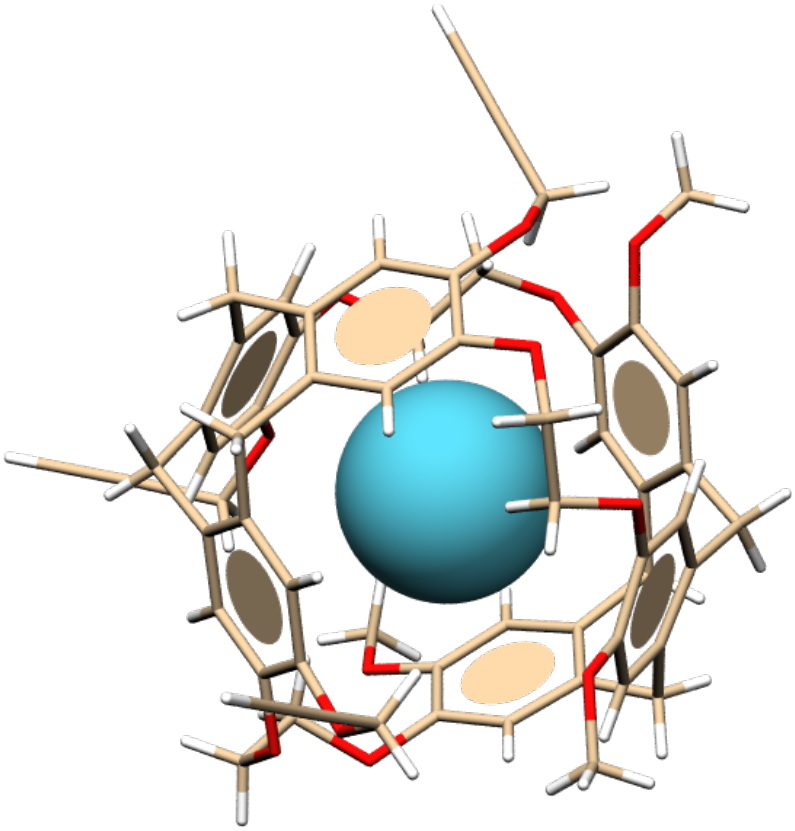

Figure 3.3: Crystal structure of Xe bound to tripropargyl cryptophane-A

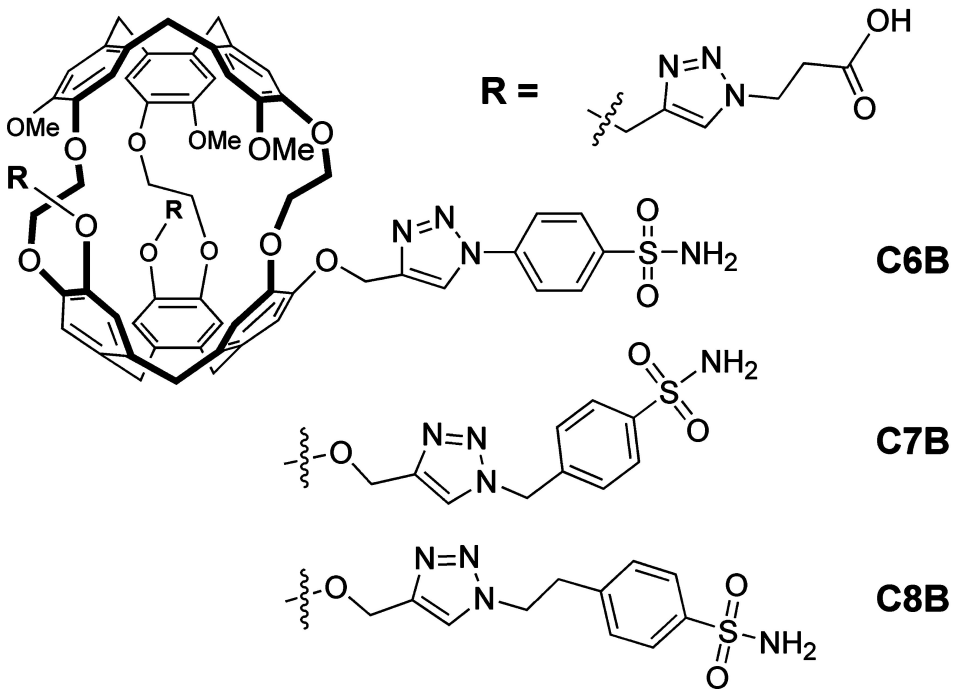

Figure 3.4: Structure of trifunctionalized cryptophane biosensors C6B, C7B, C8B, for targeting carbonic anhydrase, from reference [22].

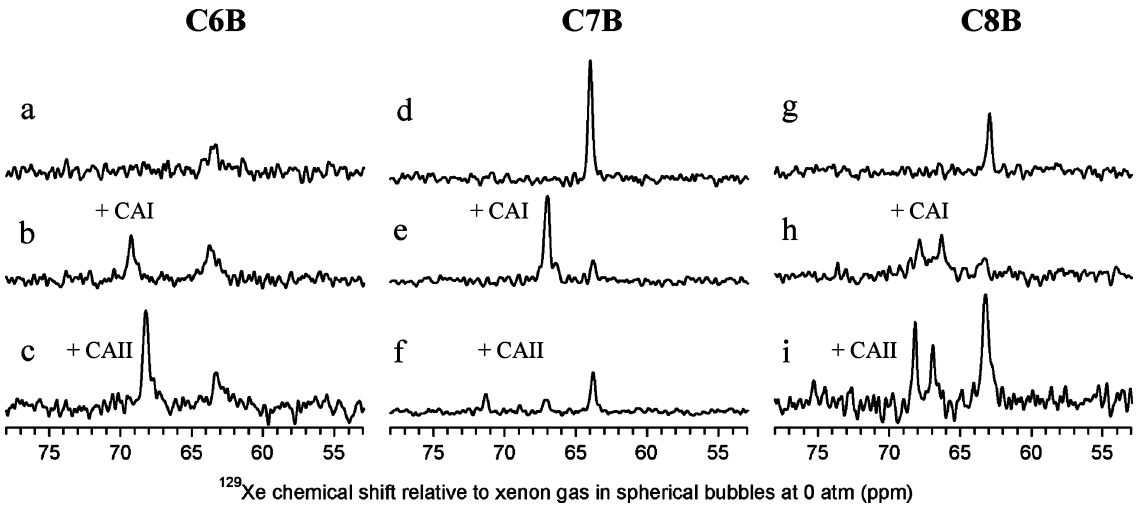

Figure 3.5: HP ^{129}Xe NMR spectra of benzenesulfonamide biosensors binding to wild-type carbonic anhydrase isomers I and II, from reference [22]. (a,d,g) ^{129}Xe NMR spectra showing individual biosensors free in solution, (b,e,h) ^{129}Xe NMR spectra showing each biosensor bound to CAI. (c,f,i) ^{129}Xe NMR spectra showing each biosensor bound to CAII. (a) C6B alone (96 µM); (b) C6B (188 µM) and CAI (141 µM); (c) C6B (148 µM) and CAII (123 µM); (d) C7B alone (186 µM); (e) C7B (136 µM) and CAI (100 µM); (f) C7B (132 µM) and CAII (105 µM); (g) C8B alone (121 µM); (h) C8B (189 µM) and CAI (141 µM); (i) C8B (189 µM) and CAII (153 µM).

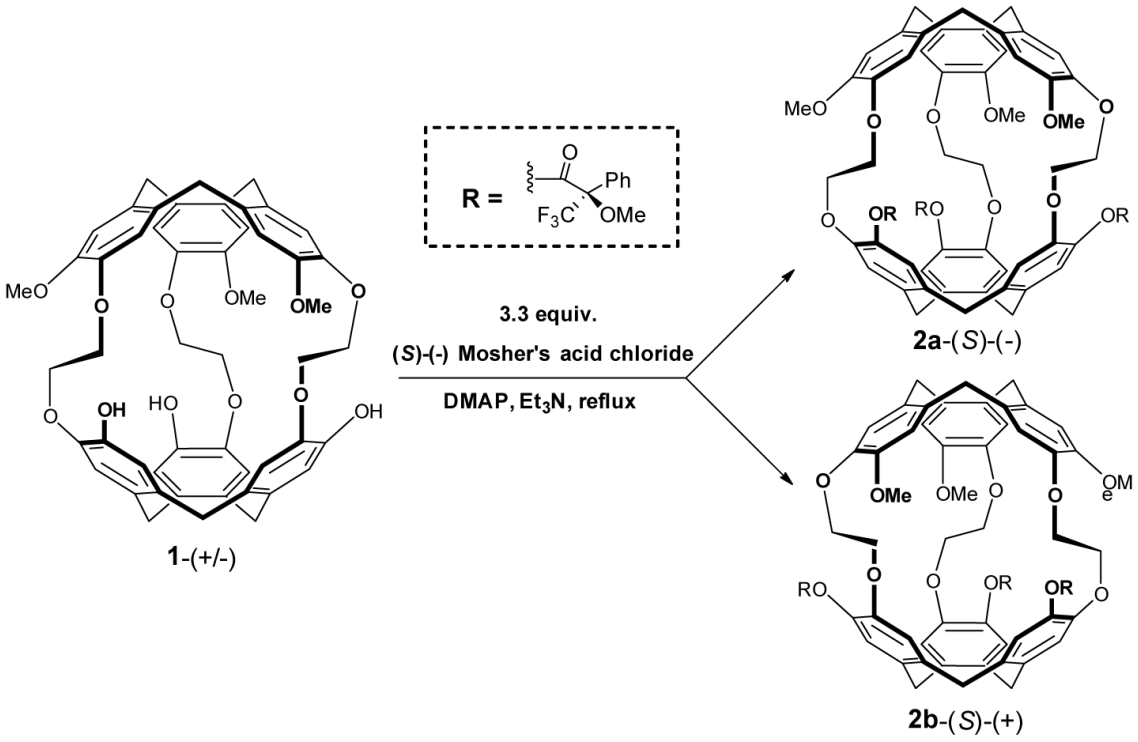

Figure 3.6: Structure of stereo-pure tri-substituted cryptophane-A derivatives, from reference [68]. By attaching mosher's acid moieties and column chromatography separation, two enantiomers of cryptophanes can be separated, and further substituted into other tri-functionalized cryptophanes. Note the difference between (2a) and (2b) is the orientation of linkers between two caps.

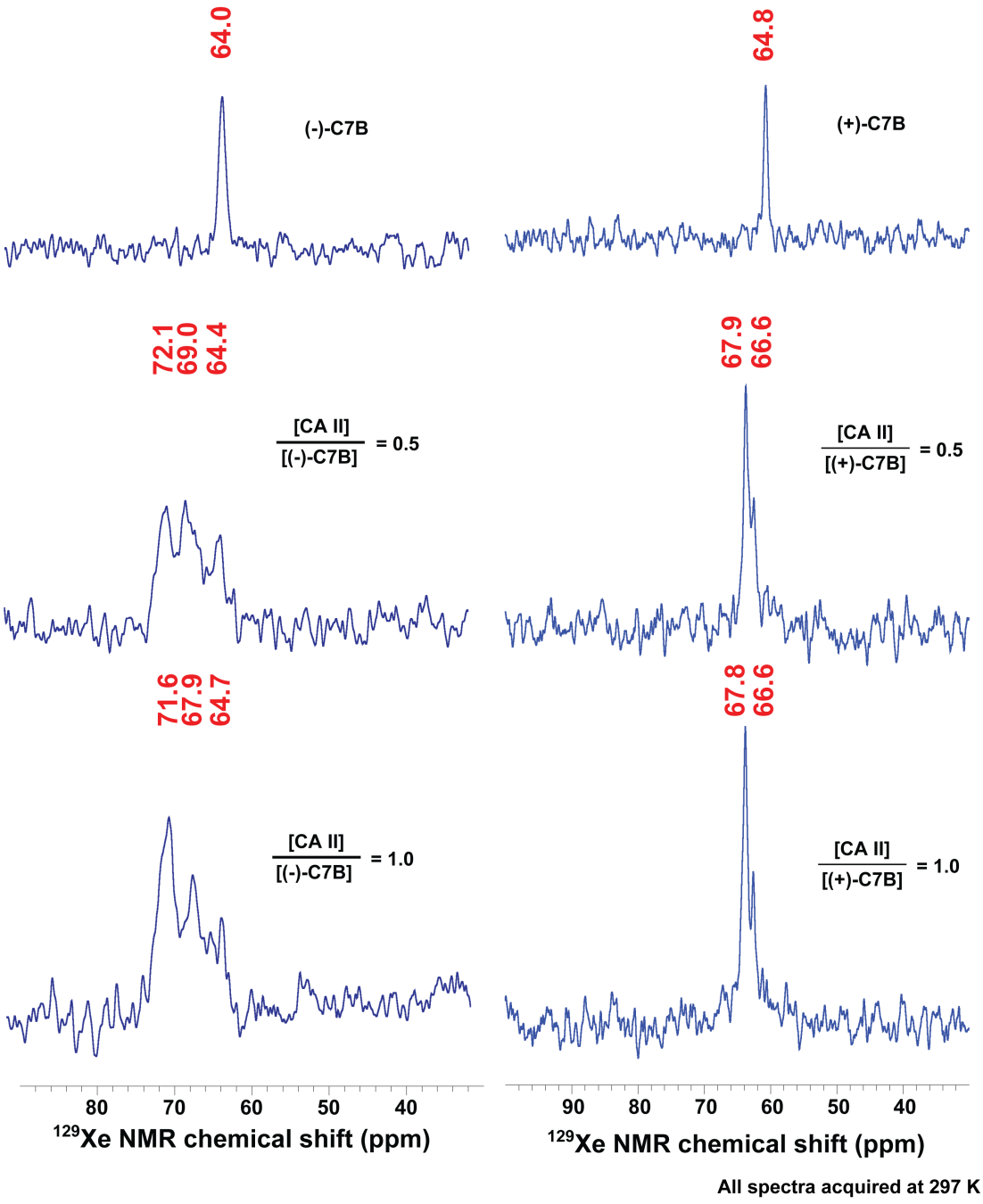

Figure 3.7: HP ^{129}Xe NMR spectra of stereo-pure C7B carbonic anhydrase biosensor binding to wild-type carbonic anhydrase II.

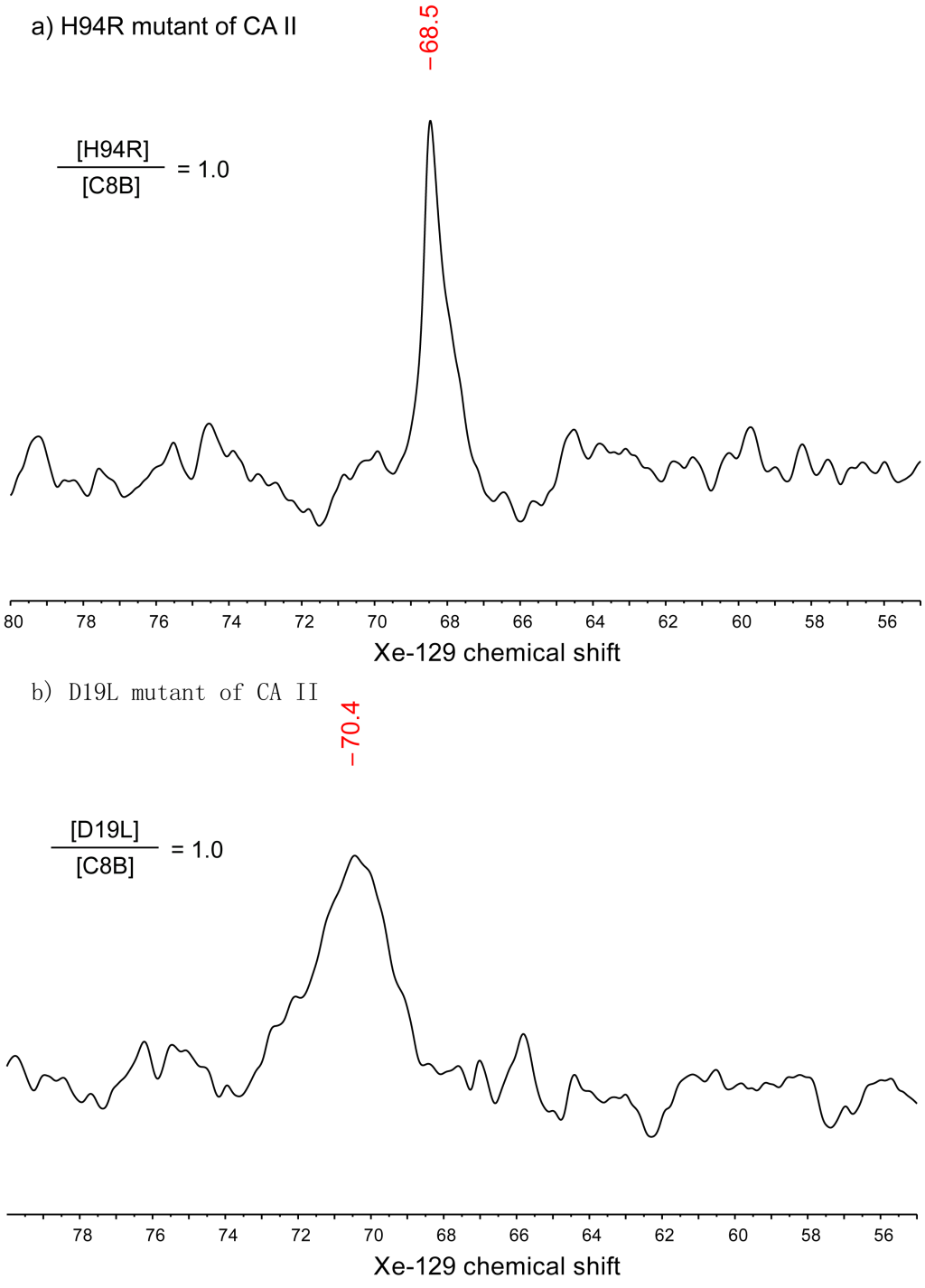

Figure 3.8: HP ^{129}Xe NMR spectra of C8B carbonic anhydrase biosensor binding to H94R and D19L mutants of carbonic anhydrase II.

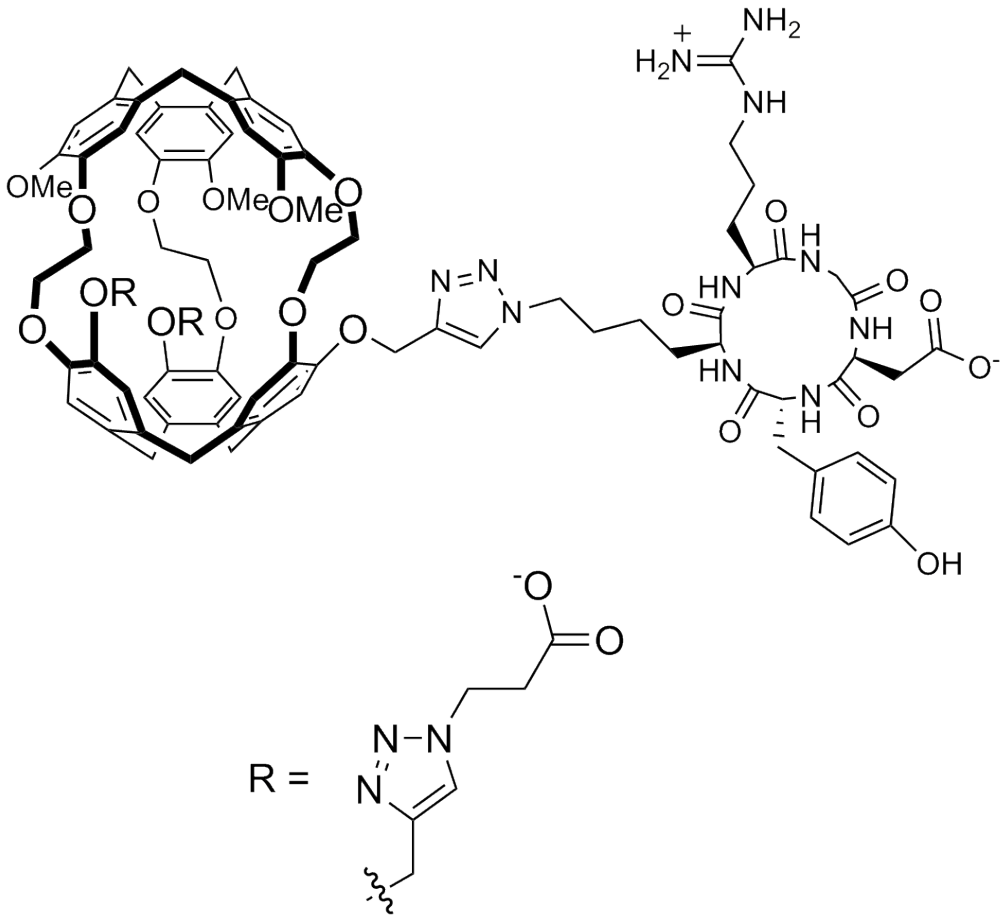

Figure 3.9: Structure of $\alpha_v\beta_3$ integrin biosensor. The cyclic RGDyk peptide moiety serves to target the integrin.

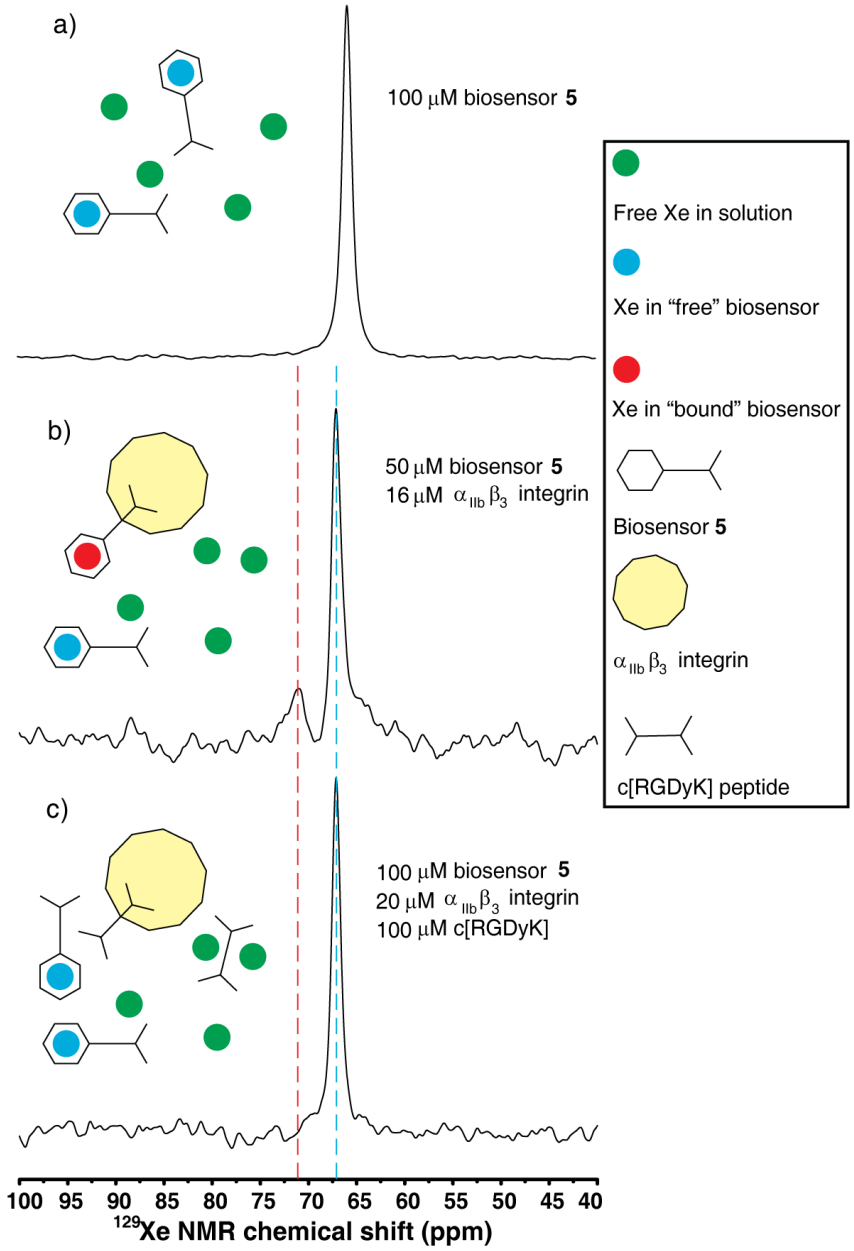

Figure 3.10: HP ^{129}Xe NMR spectra of $\alpha_v\beta_3$ integrin biosensor. (a) biosensor dissolved in Tris buffer (1 mM, pH 7.2) gave ^{129}Xe NMR chemical shift at 65.8 ppm. (b) biosensor and $\alpha_{\mathrm{IIb}}\beta_3$ integrin were mixed in Tris buffer with 30% glycerol and 0.1% Triton X-100. "Free" cryptophane gave ^{129}Xe NMR chemical shift at 67.1 ppm, while "bound" cryptophane appeared at 71.2 ppm, representing a 4.1 ppm down-field shift. (c) c[RGDyK] displaced biosensor from $\alpha_{\mathrm{IIb}}\beta_3$ integrin, in same buffer as (b). "Free" cryptophane gave the same ^{129}Xe NMR chemical shift, however no "bound" cryptophane was detected.

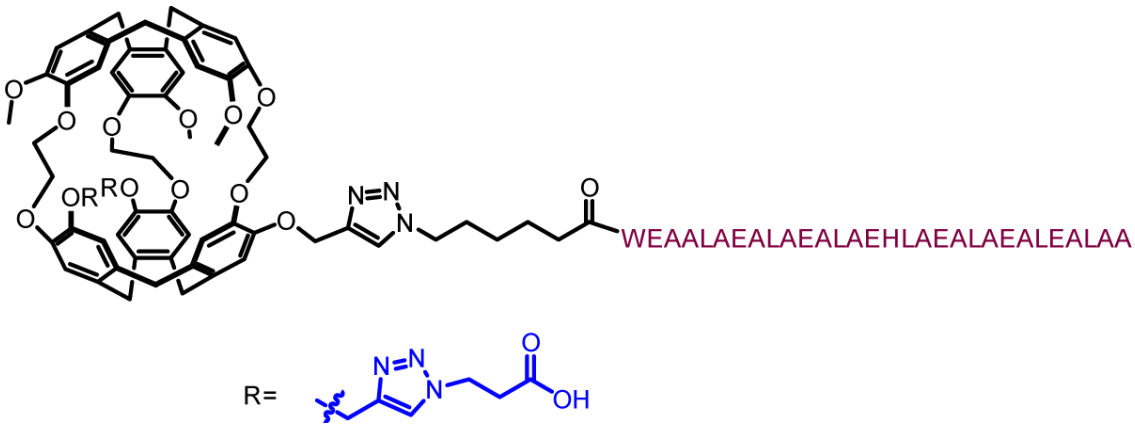

Figure 3.11: Structure of pH-sensitive cryptophane derived from EALA peptide. This cryptophane is derived from tri-propargyl cryptophane-A. EALA peptide and two propionic acid moieties are covalently bonded by click-chemistry. Conformational changes in the peptide at different pH values result in different ^{129}Xe NMR spectra.

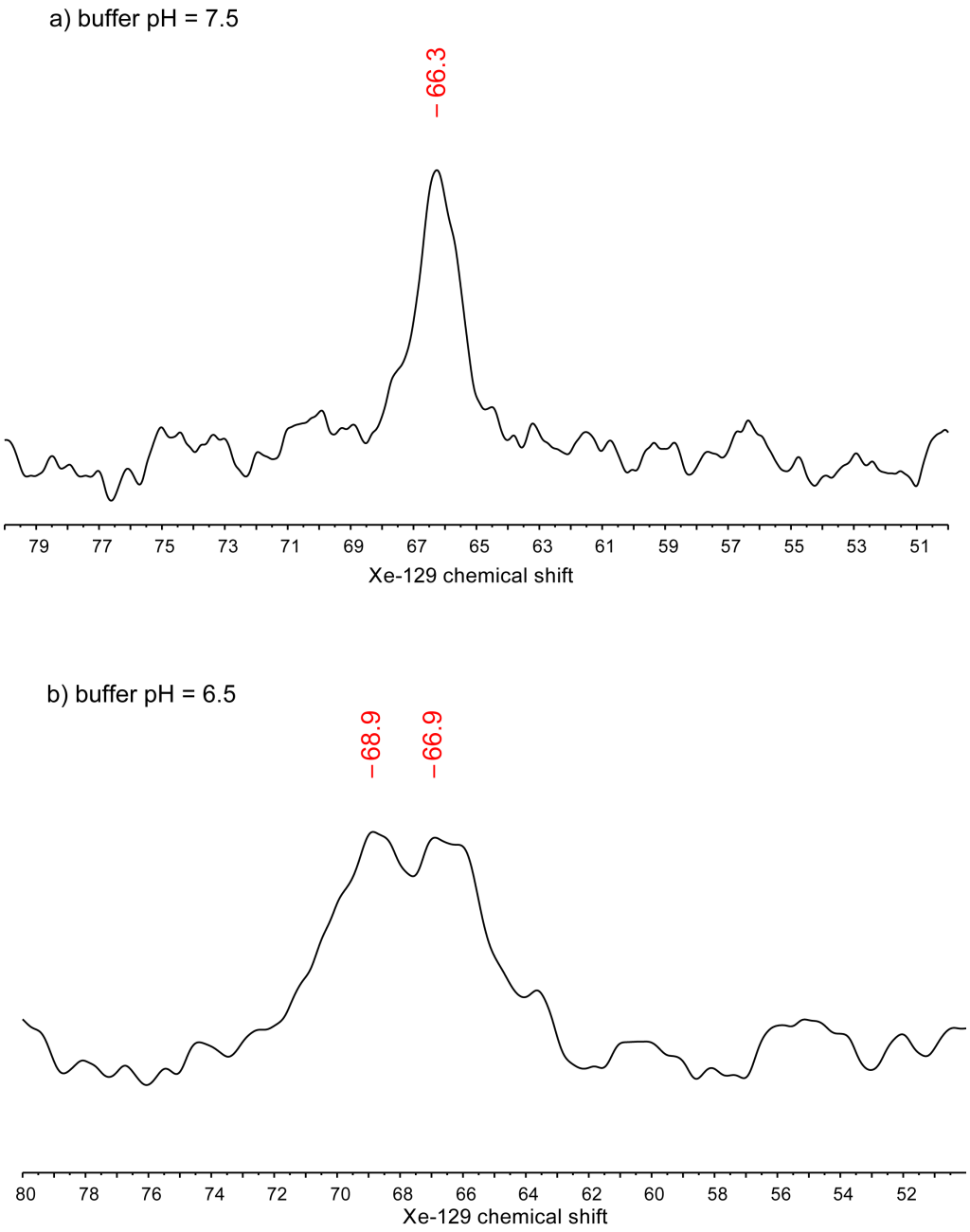

Figure 3.12: HP ^{129}Xe NMR spectra of EALA cryptophane at different pH. At pH 7.5 only one signal (66.3 ppm) of Xe@crypt exists, showing uniformly random peptide conformation; At pH 6.5 another signal (68.9 ppm) appears, indicating the peptide partially forms α-helix.

Chapter 4

Ultrasensitive Hyper-CEST NMR with TAAC

4.1 Background

Methods for detecting trace analytes play critical roles in chemistry and many applied fields, including biotechnology, biophysics, molecular pathology, metallurgy and homeland security. Nuclear magnetic resonance (NMR) spectroscopy is a versatile technique for probing molecular structure but typically offers limited detection sensitivity, based on the small magnetic moment of commonly employed nuclei (e.g., ^{1}H, ^{13}C, ^{15}N) and the narrow separation in energy levels between nuclear spin transitions. This leads to small polarization of the nuclear spin reservoir, where the difference in spin populations aligned parallel or anti-parallel to an external magnetic field at thermal equilibrium is typically just 1 in 1×10^5 spins. Thus, significantly enhanced NMR signals can be obtained via hyperpolarization techniques capable of generating a nuclear spin polarization level approaching 100% [37, 40].

For applications in biodetection and materials science, we [22] and others [55] have investigated the noble gas isotope ^{129}Xe, which is spin-$\frac{1}{2}$ and readily hyperpolarized (HP) via spin-exchange optical pumping. However, due to low concentrations of the delivered magnetic species and short spin relaxation lifetimes, the signal intensity is still not ideal for many demanding applications, e.g., clinical MRI [12, 81]. When exchanging magnetic species are present, chemical exchange saturation transfer (CEST) can provide another source of signal amplification based on cumulative magnetization transfer through selective saturation [13]. For proton MRI, CEST contrast originates from exchange of endogenous or exogenous amide

or hydroxyl protons with bulk water protons, or from exchangeable sites on paramagnetic inorganic coordination complexes [14, 82]. This gives the possibility of designing extremely sensitive contrast agents that respond to various exchange events, with techniques known as PARACEST [83] and LIPOCEST [84]. More recently, the analogous technique involving HP ^{129}Xe CEST (Hyper-CEST) was developed [85]. Based on its considerable polarizability, xenon exhibits significant affinity for organic host molecules known as cryptophanes [23, 24, 55, 56, 86–89]. In one example, Hyper-CEST was applied to virus capsids modified by ∼125 cryptophanes, thereby attaining 0.7 pM capsid detection sensitivity [30].

Here we present ultrasensitive Hyper-CEST NMR with a water-soluble triacetic acid cryptophane-A derivative (TAAC, Figure 4.1). ^{129}Xe NMR biosensors using similarly derivatized cryptophanes have been shown previously to be useful for detecting a wide variety of analytes [21, 22, 26, 27, 29, 31, 71, 90–92]. This single-unit cryptophane derivative, TAAC, was indirectly detected at 1.4 picomolar concentration at 320 K in aqueous solution, which is the record for a xenon host. Thermodynamic and kinetic studies of xenon binding were carried out to investigate this sensitivity enhancement, which establish TAAC as a very effective xenon binder/"spin catalyst" under the Hyper-CEST scheme. Our results suggest multiple Xe exchange processes for cryptophane-mediated HP ^{129}Xe NMR signal enhancement.

4.2 Experimental

4.2.1 Materials

TAAC was previously prepared by a thirteen-step synthesis [24], and found to be soluble to ∼500 µM in aqueous solution (pH 7), owing to its three carboxylates. The identity and purity of TAAC were confirmed by ^{1}H NMR spectroscopy. TAAC features a xenon association constant (K_A) of 33 000 M^{-1} at 293 K, making it currently one of the highest-affinity Xe host molecules [24, 56, 87].

Ultra-filtered water (18 $M \cdot \Omega \cdot cm$ resistivity) obtained from Mar Cor filtration system, was used to prepare TAAC solutions. TAAC (1.43 mg) was carefully weighed and dissolved in 10 mL water to form a 140 µM solution, which was confirmed by Agilent 8453 UV-vis spectrophotometer (285 cm^{-1}). For the Hyper-CEST experiments a series of 10-fold dilutions with ultra-filtered water was performed to bring TAAC solution down to picomolar concentrations. Dilutions were made with well calibrated Eppendorf Research pipettes with <1% error. After each dilution, solution was vortexed to homogenize sample. Reagents were used as purchased from Fisher: sodium phosphate dibasic heptahydrate, sodium phosphate monobasic dihydrate. Prior to isothermal titration calorimetry (ITC) measurement, TAAC solution was dialyzed in phosphate buffer (20 mM, pH 7.5) by GE Mini Dialysis Kit (1 kDa cut-off).

In the NMR samples, xenon concentrations were calculated by multiplying the

xenon partial pressure with its mole-fraction solubility in water, at a given temperature. For example, during the Hyper-CEST experiment at 320 K (Xe, all isotopes), is calculated as: xenon partial pressure in gas line $\times$ mole fraction solubility (at 320 K, 1 atm) $\times$ molarity of water $= 0.045 \times 4.95 \times 10^{-5} \times 55.5$ M $= 0.12$ mM, following Henry's Law. The concentration of hyperpolarized ^{129}Xe in solution (3.2-4.8 µM) was determined by multiplying [Xe] by the natural isotopic abundance (26.4%) and the hyperpolarization level (10-15%), measured by comparing with thermal Xe sample [93].

4.2.2 General NMR Method

A 500 MHz Bruker BioDRX NMR spectrometer was used for all ^{129}Xe NMR measurements. RF pulse frequency for ^{129}Xe was 138.12 MHz. Samples were observed using either a 5 mm PABBO NMR probe or a similar 10 mm probe. HP ^{129}Xe was generated using a home-built ^{129}Xe hyperpolarizer, based on the Nycomed-Amersham (now GE) IGI.Xe.2000 commercial system. A gas mixture of 89% helium, 10% nitrogen, and 1% natural abundance xenon (Concord Gases, NJ) was used for the hyperpolarizer input. ^{129}Xe was hyperpolarized to 10-15% after optical pumping of Rb vapor with 795 nm circularly polarized laser, cryogenic separation of Xe, and accumulation and collection in CAV NMR tubes (New Era). For the TAAC spectrum and exchange rate measurements, after introducing HP Xe to sample solution, the sealed NMR tube was shaken vigorously to mix solution with HP

^{129}Xe.

Directly recorded ^{129}Xe NMR spectra were acquired using 30° hard excitation pulses (7.5 µs on 5 mm probe), or 90° EBurp1 shaped pulses (7.5 ms, 602 Hz excitation bandwidth). Spectra were signal averaged by 10-30 scans. A delay of 0.15 s was given between scans to allow depolarized Xe to leave the cryptophane cavity and fresh HP Xe to enter the cavity. The spectra shown in Figure 4.2, page 75 were exponentially broadened by 4 Hz to give a larger signal/noise ratio. Sample temperature was controlled by VT unit on NMR spectrometer to ± 1 K.

At a series of temperatures from 300-325 K, HP ^{129}Xe NMR spectra were acquired following the aforementioned protocol and the natural line widths of the Xe@TAAC peaks were fitted (FWHM, Lorentzian) and summarized in Table 4.1.

4.2.3 Hyper-CEST Method

Figure 4.3 illustrates the Hyper-CEST experiment involving TAAC. Before starting the pulse sequence each time, a controllable amount of HP Xe was delivered into the 3-mL sample solution, and sealed in the NMR tube for signal stabilization by a homebuilt continuous-flow HP Xe delivery setup (Figure 2.7, page 31). Multiple selective 180° radio-frequency (RF) pulses were delivered to the sample at the ^{129}Xe@TAAC resonance frequency, while HP Xe and depolarized Xe were dynamically exchanging in and out of TAAC. As a result, depolarized Xe was accumulated in the aqueous sample, and detected by another 90 degree hard excitation pulse.

HP Xe in water undergoes depolarization exponentially by the time constant T_1. However, in the Hyper-CEST experiment TAAC served as a "depolarization catalyst", and could be turned "on" and "off" using a saturation frequency that was either on- or off-resonance with ^{129}Xe@TAAC.

Utilizing a home-built continuous flow HP Xe delivery setup (Figure 2.7, page 31), freshly hyperpolarized Xe gas mixture was bubbled through sample solutions at 65 psi. Before starting the pulse program each time, bubbling was stopped by two solenoid valves to maintain magnetic field homogeneity.

The Hyper-CEST experiment was carried out using the pulse program illustrated in Figure 2.6. DSnob-shaped pulses (parameter sp6) were looped numerous times (L6) to induce xenon polarization transfer. In the low concentration trials, where d12 $\ll$ sp6 in duration, the radiation became near-continuous. The DSnob pulse power was calibrated to give maximum saturation. With a single DSnob pulse (sp6) irradiated at Xe(aq) frequency, ¿90% signal was saturated. After the overall polarization was reduced by saturation pulses and chemical exchange, the sample was irradiated with a 90 degree hard pulse to read out the final magnetization state of ^{129}Xe in solution. Due to imperfection of frequency selectivity, sp6 contributed significantly to the off-resonance regions of the spectrum after 10 000 repeats. Therefore, for the lowest concentration TAAC Hyper-CEST experiments the Xe(aq) peaks were relaxed faster than the analogous T_1 of HP ^{129}Xe in aqueous solution.

4.2.4 Isothermal Titration Calorimetry (ITC)

ITC samples were prepared as described, and xenon binding measurements were performed using a MicroCal VP-ITC titration micro-calorimeter (Northampton, MA) at 310 K. Standard protocols and data analyses were used. Control enthalpograms for ITC are presented in Figures 4.6, 4.7, 4.8.

Xe@TAAC NMR line widths at different temperatures. The spectra were Lorentzian deconvolved to fit for full width at half maximum (FWHM). Peak widths of the Xe@TAAC peaks were corrected by subtracting the Xe(aq) peak line widths to account for magnet inhomogeneity. The line widths of Xe(aq) peaks range between 8-18 Hz (from 297 K to 320 K), which mainly originates from magnetic field homogeneity. This response of aqueous ^{129}Xe to temperature change was negligible compared to ^{129}Xe@TAAC peaks (Table4.1).

Xenon exchange lifetime measurement. Though 2D EXSY NMR is the standard method for determining exchange rates [94], selective 1D EXSY NMR [28, 95, 96] serves as a better measurement scheme in this case, due to the spectral dominance of the HP ^{129}Xe(aq) peak. Using a customized EXSY pulse sequence [28], the Xe@TAAC resonance was selectively excited and acquired twice (separated by designated mixing times), generating two FIDs (initial and recovery). The ratio of signal intensities was calculated to quantify the percentage of Xe@TAAC replenishment, at a manually set mixing time that's close to the xenon exchange lifetime being fitted. With a series of exchange-replenishment ratios and their correspond-

ing mixing times, Xe exchange lifetime can be fitted, providing a measurement of cryptophane-Xe exchange performance.

4.3 Results and Discussion

4.3.1 Hyperpolarized ^{129}Xe NMR Spectra of TAAC in Aqueous Solution

Two peaks arise in the HP ^{129}Xe NMR spectrum of 140 µM TAAC aqueous solution (Figure 4.2): Xe dissolved in water at 320 K (Xe(aq), 194.3 ppm) and Xe bound in TAAC (Xe@TAAC, 65.8 ppm). In HP ^{129}Xe detection schemes investigated to date, there is a large excess of Xe (mM) relative to cryptophane (µM) [97], which results in a Xe(aq) peak that is ∼1000 times stronger than Xe@TAAC without selective excitation. Given the almost 130 ppm separation of the two peaks, selective RF pulses focused on Xe@TAAC will have little effect on Xe(aq) under most conditions, which allows selective excitation of the minor "cryptophane-bound" species as well as selective saturation exchange experiments.

Direct detection, even selective excitation (for example, Figure 4.2), requires micromolar cryptophane, which limits cryptophane biosensor experiments to prevalent biological targets. Some cryptophanes may also be toxic to cells at this concentration [25,26]. Instead of trying to detect directly the Xe@TAAC peak, the Xe@TAAC resonance can be indirectly measured more sensitively via magnetization transfer

from the much stronger Xe(aq) signal.

Xenon binding kinetics of TAAC. The thermodynamics of xenon binding is established by the equilibrium shown in eq4.3.1:

$$\text{Xe+S@TAAC} \underset{k_{off}}{\overset{k_{on}}{\rightleftharpoons}} \text{Xe@TAAC + S} \tag{4.3.1}$$

where S@TAAC indicates solvent-bound TAAC. It is experimentally observed [98] that "empty" cryptophane is preferably bound with solvent, in this case one or multiple water molecules. Because the concentration of solvent is constant, the reverse process in eq4.3.1 can be simplified to be first-order, yielding constant "k_{off}" ($k_{off}[S]$). This yields eq4.3.2 with the rate constants of xenon binding (k_{on}) and dissociation (k_{off}) indicated:

$$k_{on}[\text{Xe}][\text{TAAC}] = k_{off}[\text{Xe@TAAC}] \tag{4.3.2}$$

The maximal Hyper-CEST effect should occur under conditions where all of the cryptophane is encapsulating xenon (to ensure maximal Xe absorption of the RF pulse) while still allowing the most rapid "Xe in"-"Xe out" exchange. The xenon on- and off-rates (k_{on}, k_{off}) describe the rates at which HP Xe gains access to the cavity of TAAC and the rate at which depolarized Xe leaves TAAC. This exchange process should occur most rapidly when a HP Xe atom directly displaces depolarized Xe, with no intermediary solvent binding. However, because TAAC experiments are conducted in water, solvent may compete with Xe binding.

4.3.2 Ultra-sensitive Detection of TAAC

Picomolar TAAC was detected by a series of Hyper-CEST measurements, following the general method developed in the Pines lab. [92] In Figure 4.4 on page 77, relative intensity of Xe(aq) signal was plotted against the time of saturation transfer pulse cycles, which is representative data from three trials. As in Figure 2.6, the shaped saturation pulse was configured to resonate at the frequency of Xe@TAAC signal (65.8 ppm). As a control, saturation at a mirror frequency ($2 \times 194.3 - 65.8 = 322.8$ ppm) was established, to perform off-resonance Hyper-CEST. When the saturation pulse was tuned to Xe(aq) frequency, the peak was able to be completely saturated with 2 scans. At 14 pM TAAC concentration and higher, on-resonance Hyper-CEST clearly presented a more sharply decaying Xe depolarization curve, indicating effective saturation transfer. After 10-fold dilution, the difference in depolarization rate was still observable from exponential fits (Figure 4.4, due to the instability of data, we didn't achieve good measurement of depolarization lifetime. However the clear difference between on- and off- resonance are verified). Detection of 1.4 pM TAAC is currently the lowest observed concentration for a single-unit Xe host. Previously, the Pines lab demonstrated detection of 10 nM cryptophane using this technique [99]. To explain the much greater detection sensitivity obtained in the current experiment, we hypothesized that TAAC must have much more rapid xenon exchange kinetics compared to previously measured cryptophane systems, in addition to its favorably high Xe@TAAC occupancy. To explore the origins of the

achieved sensitivity, a series of characterization experiments was performed.

4.3.3 ITC Measurement of Xenon Binding to TAAC

TAAC should be favorable for Hyper-CEST NMR based on its high Xe affinity. Moreover, its strongly positive entropy of Xe binding ($S = 5.9\ cal \cdot mol^{-1} \cdot K^{-1}$) at 293 K) supports high affinity as temperature increases from rt to physiological conditions [24]. Indeed, ITC measurements performed at 310 K showed the Xe-TAAC association constant to be 33 000 $\pm$ 2000 M^{-1} (Figure 4.5), the same value determined at 293 K [24]. During the Hyper-CEST experiment, xenon concentration [97] is calculated to be 0.12 mM by assuming the hyperpolarized Xe gas mixture, at 1 atm, saturates the sample solution. Therefore, more than 80% of the TAAC molecules were bound to Xe, which is higher than the 45-60% host occupancy in previous Hyper-CEST NMR experiments [30, 99, 100].

4.3.4 Xe@TAAC NMR Line Widths at Different Temperatures

Spectra were acquired for 140 µM TAAC aqueous solution following the same method as Figure 4.2, at different temperatures (see Table 4.1). The spectra were Lorentzian deconvolved to fit for full width at half maximum (FWHM). Peak widths of the Xe@TAAC peaks were corrected by subtracting the Xe(aq) peak line widths to account for magnet inhomogeneity.

4.3.5 Xenon Exchange Lifetime Measurement

Previously, Xe-cryptophane exchange rates in organic solution were measured by 2D ^{129}Xe NMR [95] spectroscopy and approximated by measuring the line width of the Xe@cryptophane NMR resonance [86]. Due to the high concentrations of xenon and cryptophane that dissolved in $C_2D_2Cl_4$ [95], it was possible to use the small ^{129}Xe polarization provided by the NMR magnet. Here, in order to examine the origins of the heightened cryptophane-mediated HP ^{129}Xe depolarization achieved with TAAC, we sought to measure the xenon-cryptophane exchange kinetics in aqueous solution by the combination of NMR selective excitation and ^{129}Xe hyperpolarization, which was demonstrated previously for a biotin-derivatized xenon biosensor [28].

By altering the exchange mixing time, a series of Xe replenishment efficiencies was measured (Figure 4.9). The xenon exchange lifetime, τ_{exch}, was determined to be 22 ± 3 ms at 297 K. This τ_{exch} value is shorter than measured for all previous cryptophanes in water close to rt [28, 70, 88, 89]. Using the measured τ_{exch} and K_A, xenon dissociation and association rate constants were determined at 297 K: $k_{off} \approx k_{exch} = 1/\tau_{exch} = 45 \pm 15$ s^{-1} and $k_{on} \approx 1.5 \times 10^6$ M$^{-1} \cdot$ s^{-1}. As k_{exch} is an intermolecular process [86], it likely underestimates the Xe dissociation rate (k_{off}) [28]. Despite this difference, the measured rates are more than 2-fold faster than the exchange rates measured for water-soluble cryptophanes with comparable Xe affinity ($k_{on} = 3.8 \times 10^5$ M$^{-1} \cdot$ s^{-1}; $k_{off} = 13.1$ s^{-1} at 293 K [88, 89];). Our

measured exchange rates with TAAC in water are more typical of cryptophane-A derivatives in organic solvent, where millisecond timescales have been observed [28]. A key difference, however, is that in large organic solvents such as $C_2D_2Cl_4$, the cryptophane should remain empty during the Xe exchange process. In water, solvent binding to TAAC will slow the Xe exchange process, with k_{off} likely reflecting the rate-limiting step of water dissociation, followed by Xe binding (k_{on}).

It has been established by Pines and co-workers that Hyper-CEST becomes dramatically more sensitive at temperatures slightly above rt [99], but the origin of this effect requires further investigation. Using our experimental setup, we were unable to measure the exchange rate ($1/\tau_{exch}$) exactly at 320 K, where the Hyper-CEST experiment was performed. However, HP ^{129}Xe NMR spectra collected at different temperatures (Table 4.1) provide estimates for k_{exch} from Xe@TAAC peak line widths: $k_{exch} = 1100$ s^{-1} at 320 K, $k_{exch} = 500$ s^{-1} at 310 K, $k_{exch} = 86$ s^{-1} at 300 K, which is in reasonable agreement with the 1-D EXSY exchange rate measurement at 297 K ($k_{exch} = 45$ s^{-1}). Because of the high concentration of water (55 M) in the TAAC solution, the exchange rate is limited by the dissociation rate of water en route to Xe binding.

4.3.6 Description of HP Xe Depolarization Rate

In the overall depolarization "reaction", resulting in thermal equilibration of all xenon nuclear spins in solution, TAAC (together with selective saturation RF

pulses) acts as a "spin catalyst". When depolarization curves are fit using first-order kinetics, the TAAC-mediated HP Xe depolarization rate constant (k_{TAAC}) and the natural T_1 relaxation rate constant (k_1) both contribute to the observed loss of HP Xe. By multiplying k_{TAAC} by the starting HP Xe concentration (3.1 µM), the maximum HP Xe depolarization rate can be expressed as $k_{TAAC}\times$[HP Xe] = $0.17\ \mathrm{M}\cdot\mathrm{s}^{-1}$. After dividing by TAAC concentration (14 pM), this equates to $k_{cat} = 1.2\times10^4$ HP Xe-^{129} atoms depolarized by each TAAC molecule per second. Compared to a virus-capsid-based biosensor which we calculate to have $k_{cat} = 1.3\times10^2$ s^{-1} [30], TAAC is observed to have 100-times greater activity on a per-cryptophane basis.

For TAAC, which is 80% bound with Xe in solution, the Xe-Xe exchange rate should be the critical kinetic parameter for determining Hyper-CEST efficiency. Based on very efficient saturation transfer (¿ 0.9 in a control experiment), we assume in our analysis of TAAC that k_{cat} approximates the Xe-Xe exchange rate. At 320 K this is one order of magnitude faster than k_{off}, the proposed Xe-H_2O exchange rate measured by NMR linewidth.

This suggests that there are two different kinetic processes, with only the slower H_2O-Xe exchange process being directly observable by either 1-D EXSY or NMR linewidth measurements. Such millisecond exchange processes are most consistent with previously published Hyper-CEST NMR results [30, 71, 85, 100], which led to detection of nanomolar cryptophane concentrations.

Some of TAAC's advantage in a Hyper-CEST detection scheme may arise from differences in cryptophane structure; for example, greater water solubilization of TAAC should promote more open, Xe-accessible conformations of the cryptophane, with high xenon on- and off-rates [12]. Our previous fluorescence lifetime studies indicated that only 5-10% of TAAC in aqueous solution adopts a more collapsed, non-Xe binding conformation [24]. In addition, high Xe occupancy and narrower line widths for the HP ^{129}Xe-cryptophane complex promote RF saturation leading to efficient HP ^{129}Xe depolarization.

4.3.7 Depolarization Mechanisms

Multiple processes may contribute to rapid Xe depolarization, beyond the discussed Hyper-CEST Xe-cryptophane-water exchange mechanism (Scheme 4.3). Weak dipole-dipole interactions between ^{129}Xe nuclear spins discount the possibility for through-space depolarization effects. However, there may be significant chemical shift anisotropy of the xenon atom(s) associated with TAAC, which would significantly accelerate relaxation of ^{129}Xe nuclei [101, 102]. In addition, with induced electron currents in the bound Xe@TAAC complex [103], meaningful variations of xenon local magnetic fields can be present, providing another depolarization pathway [104]. However, neither effect can explain the 10-fold discrepancy between k_{off} measured by NMR linewidth (all Xe isotopes) and the faster k_{cat} Xe depolarization rate determined by Hyper-CEST.

We surmise that the exchange rates that are measurable by either 1-D EXSY or NMR line widths are not measuring the pairwise Xe-Xe exchange rate, but instead a slower process involving the exchange of Xe for intermediary solvent in the 20% of "empty" (water-bound) TAAC molecules. To consider the potential for a much faster Xe-Xe exchange process, we note the previous observation that Xe exchange rates for cryptophanes in organic solution are accelerated at higher Xe concentrations, indicating an "associative" exchange mechanism [86]. Direct Xe-Xe exchange may be critical for avoiding a solvent-bound "kinetic trap", which we propose should deactivate cryptophane for efficient Hyper-CEST.

Notably, 1.4 pM TAAC detection sensitivity was achieved with natural isotopic abundance Xe (26.4% ^{129}Xe) polarized to 10-15%. Thus, most of the TAAC host molecules in solution were occupied with other "silent" Xe isotopes or "thermally polarized" ^{129}Xe nuclei not contributing to bulk magnetization. At the initiation of the experiment, TAAC-bound HP ^{129}Xe concentration was estimated to be: [TAAC] $\times$TAAC occupancy percentage $\times$ ^{129}Xe isotopic abundance $\times$ hyperpolarization level = 1.4 pM $\times 80\% \times 26.4\% \times 10\% = 0.03$ pM. Our analysis predicts that at least 10-fold greater detection sensitivity may be achieved for TAAC bound with more highly polarized (50%), isotopically-enriched (86%) ^{129}Xe — conditions that should allow more efficient depolarization of ^{129}Xe by RF pulses, "catalyzed" by TAAC. In this way, femtomolar detection of TAAC and related xenon-binding molecules should be readily achievable.

4.4 Conclusions

Using ^{129}Xe Hyper-CEST NMR spectroscopy, we detected a water-soluble cryptophane TAAC at concentrations as low as 1.4 pM, through enhancement from fast chemical exchange. This is a uniquely sensitive NMR measurement, and, in particular, represents a roughly 100-fold improvement in detection sensitivity over recently published ^{129}Xe Hyper-CEST NMR data, on a per cryptophane basis [30]. To investigate the role of TAAC in improving detection sensitivity, Xe binding kinetics of TAAC were characterized for the first time, by combining exchange lifetime with association constant measurements. Favorable thermodynamic and kinetic properties of Xe binding to TAAC were determined.

Kinetic analysis of Hyper-CEST NMR experiments with TAAC revealed a rapid, TAAC-mediated ^{129}Xe depolarization mechanism (k_{TAAC}[HP ^{129}Xe] = 1.7×10^{-7} M $\cdot$ s^{-1}), which corresponds to 1.2×10^4 HP ^{129}Xe atoms depolarized per second. Assuming near unity saturation efficiency, this corresponds to one order of magnitude faster Xe exchange than k_{off} measured by 1-D EXSY and linewidth NMR measurements, which we assign to HP ^{129}Xe exchanging with H_2O in the cryptophane cavity. We propose that the sub-millisecond kinetic process inferred from Hyper-CEST NMR experiments at 320 K can be assigned to efficient Xe-Xe exchange. Ongoing theoretical calculations and experiments using different cryptophane moieties are investigating the significance of these two possible Xe-cryptophane exchange pathways. We conclude that ultrasensitive cryptophane detection supports the further

development of xenon host molecules and cryptophane-based biosensors for *in vitro* and *in vivo* ^{129}Xe magnetic resonance studies.

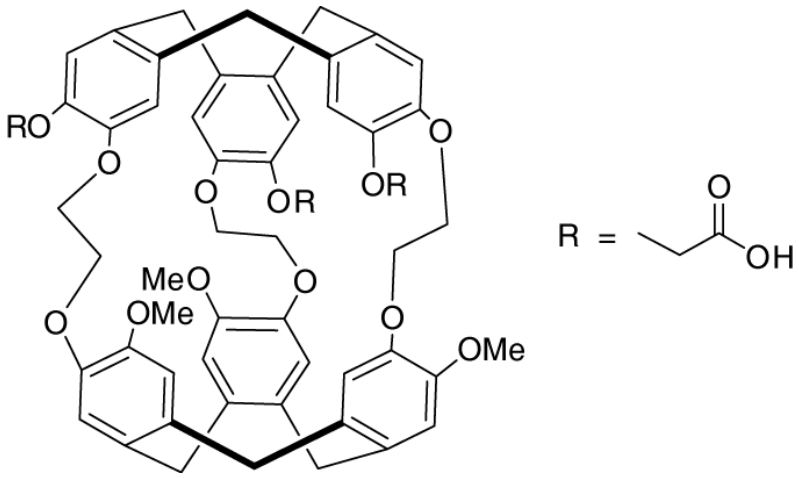

Figure 4.1: Triacetic acid cryptophane-A derivative (TAAC).

Table 4.1: Line width of ^{129}Xe@TAAC NMR peak at various temperatures, and estimated Xe exchange rates.

Temperature (K)	Line width of ^{129}Xe@TAAC peak (Hz)*	Estimated k_{exch} (s^{-1})
300	27.3 ± 1.1	86 ± 3.4
310	157.3 ± 1.1	500 ± 3.4
315	238.3 ± 3.6	750 ± 11
320	342.2 ± 5.7	1100 ± 18
325	294.2 ± 3.2	920 ± 10

*Magnetic homogeneity corrected.

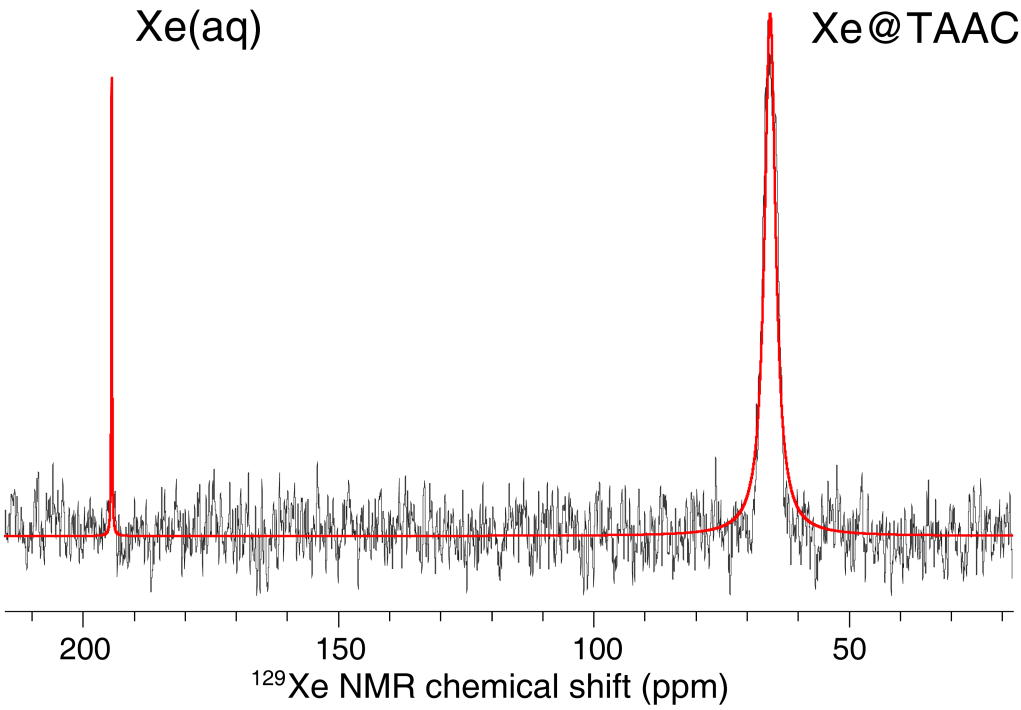

Figure 4.2: HP ^{129}Xe NMR spectrum of 140 µM TAAC dissolved in ultrafiltered water at 320 K, showing: Xe(aq) peak at 194.3 ppm and Xe@TAAC peak at 65.8 ppm (selectively excited). Lorentzian deconvolved spectrum is shown in red.

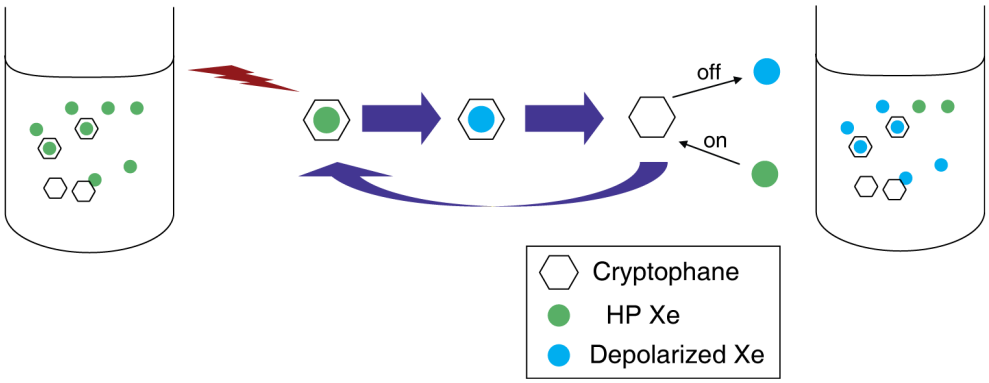

Figure 4.3: Saturation transfer processes in ^{129}Xe Hyper-CEST NMR with cryptophane.

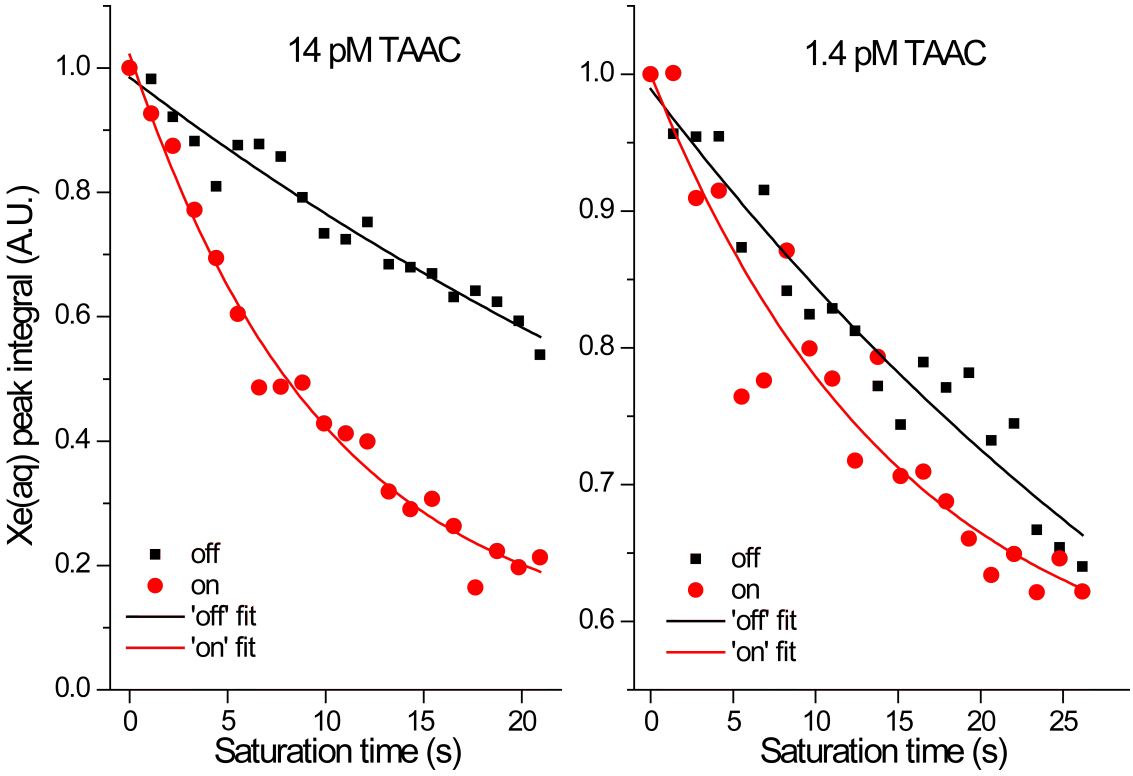

Figure 4.4: Representative ^{129}Xe Hyper-CEST profiles (from 3 trials) of 14 pM and 1.4 pM TAAC at 320 K plotted as the Xe(aq) peak intensities vs. saturation time. Differences between on- and off-resonance saturation are compared. Exponential fits of data are shown as red and dark curves. Depolarization lifetimes were fitted to be 10 ± 1 s (on) and 38 ± 2 s (off) for 14 pM sample (averaged over two trials); 53 ± 4 s (on) and 65 ± 4 s (off) for 1.4 pM sample (representative trial), respectively. In each experiment, a series of 2.6 ms DSnob pulses with 20 s delay was applied. In the Hyper-CEST pulse sequence, the following parameters were used: sp6 = 2.6 ms, d12 = 20 µs, d1 = 1 µs, L6 = 8 000 (max, 14 pM) or 10 000 (max, 1.4 pM).

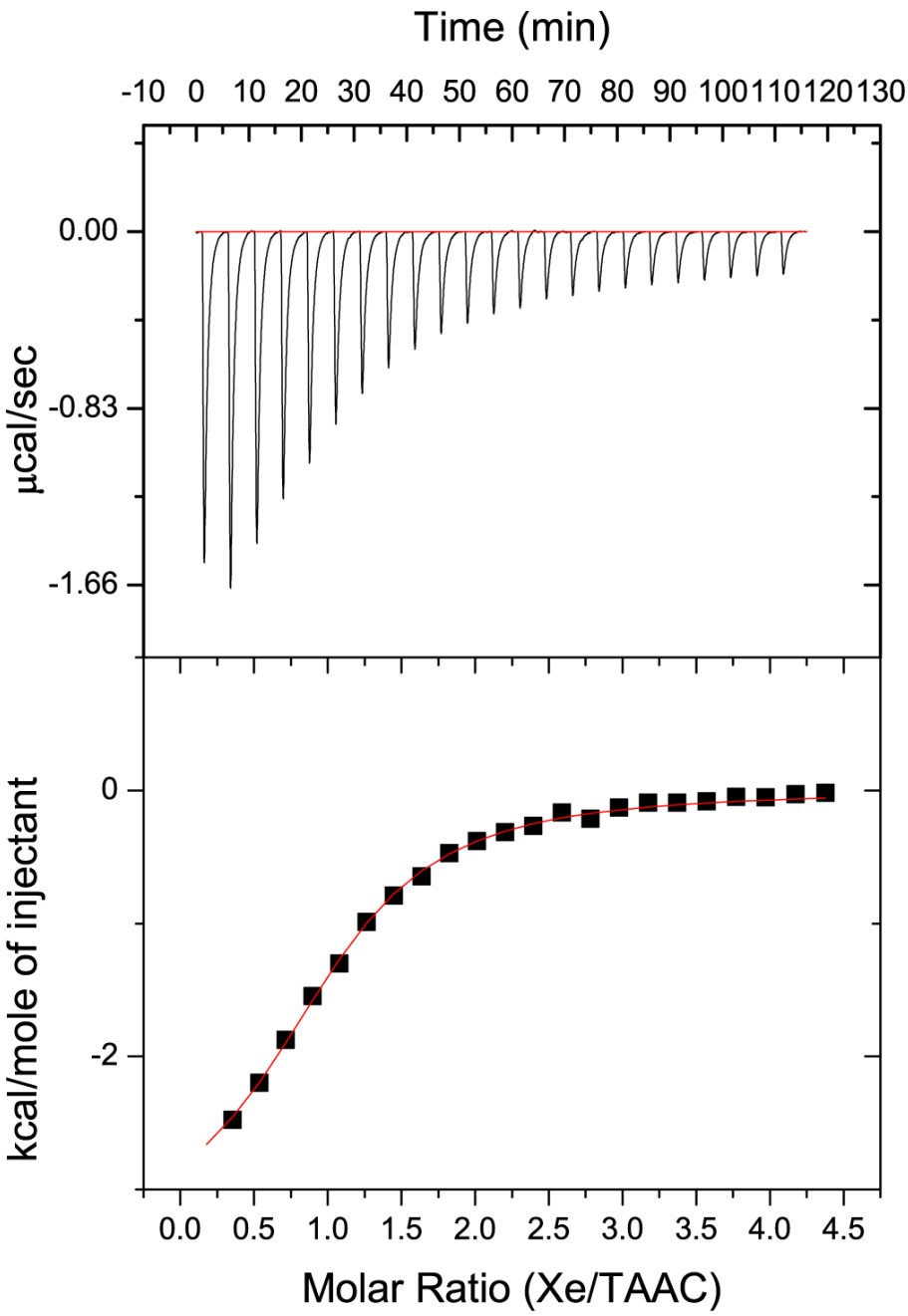

Figure 4.5: Enthalpogram of 3.31 mM aqueous xenon solution titrated into 131 µM TAAC solution (phosphate buffer, 20 mM, pH 7.5) at 310 K.

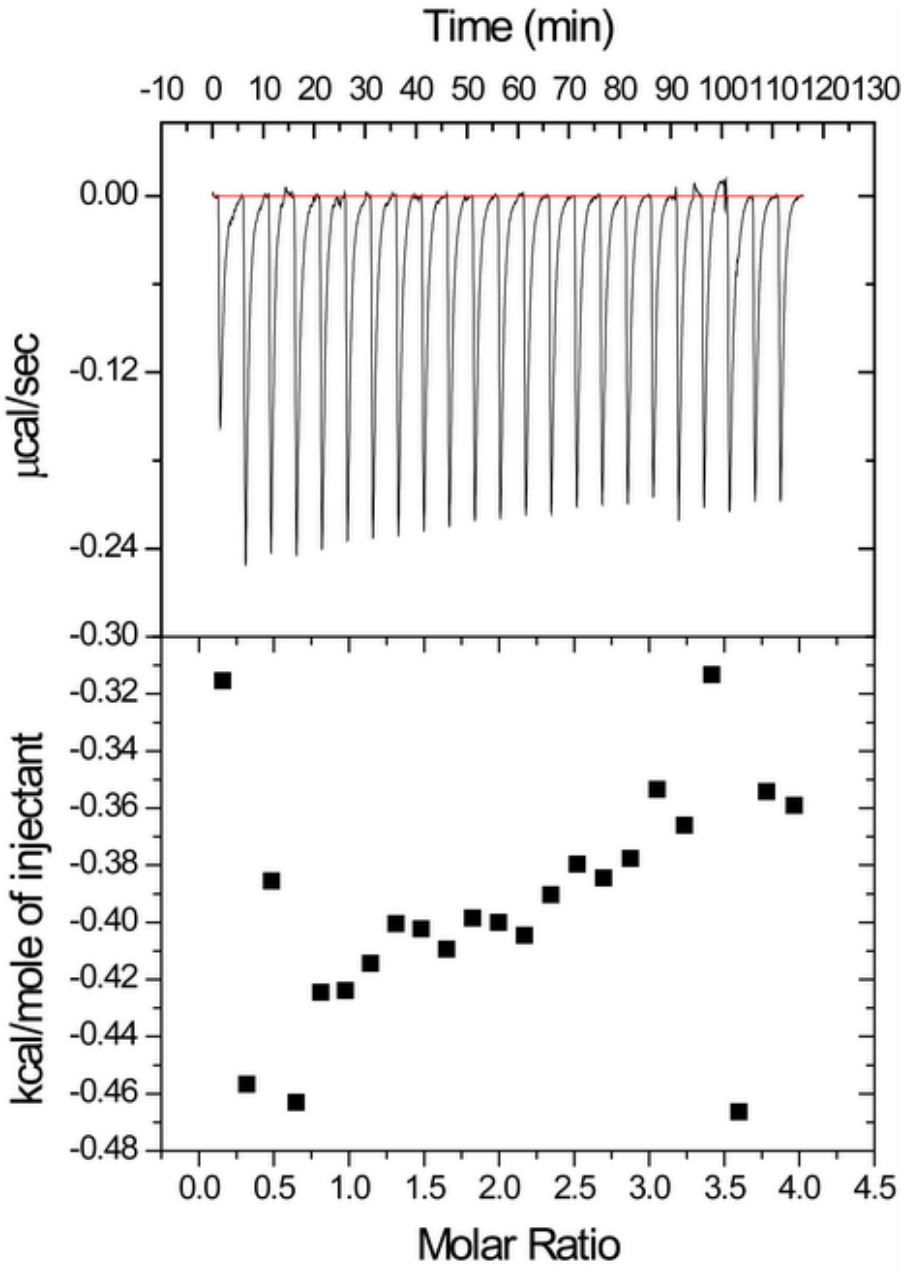

Figure 4.6: ITC buffer controls at 310 K. Water titrated into 20 mM phosphate buffer, pH 7.5.

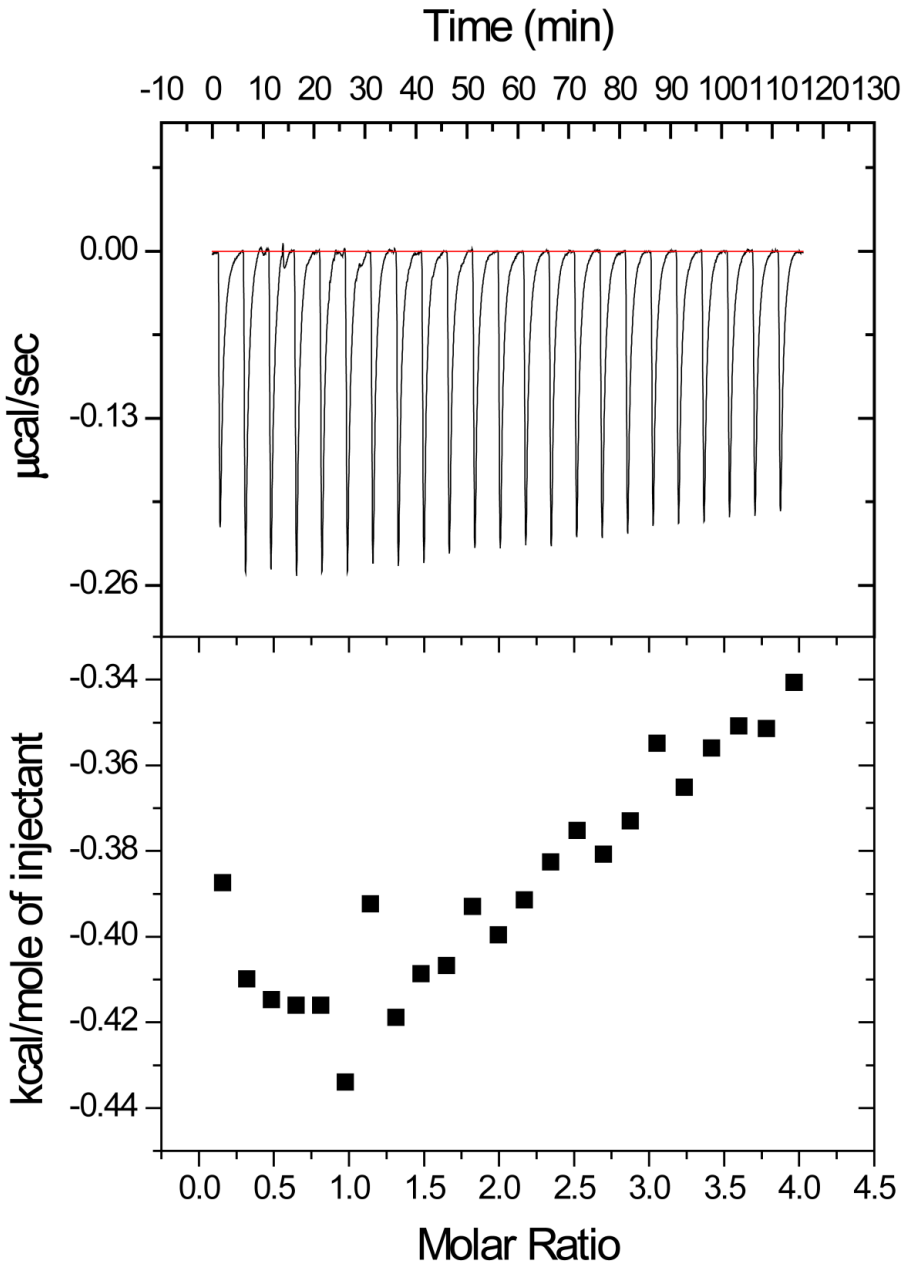

Figure 4.7: ITC buffer controls at 310 K. Water titrated into a solution of 131 µM TAAC in 20 mM phosphate buffer, pH 7.5.

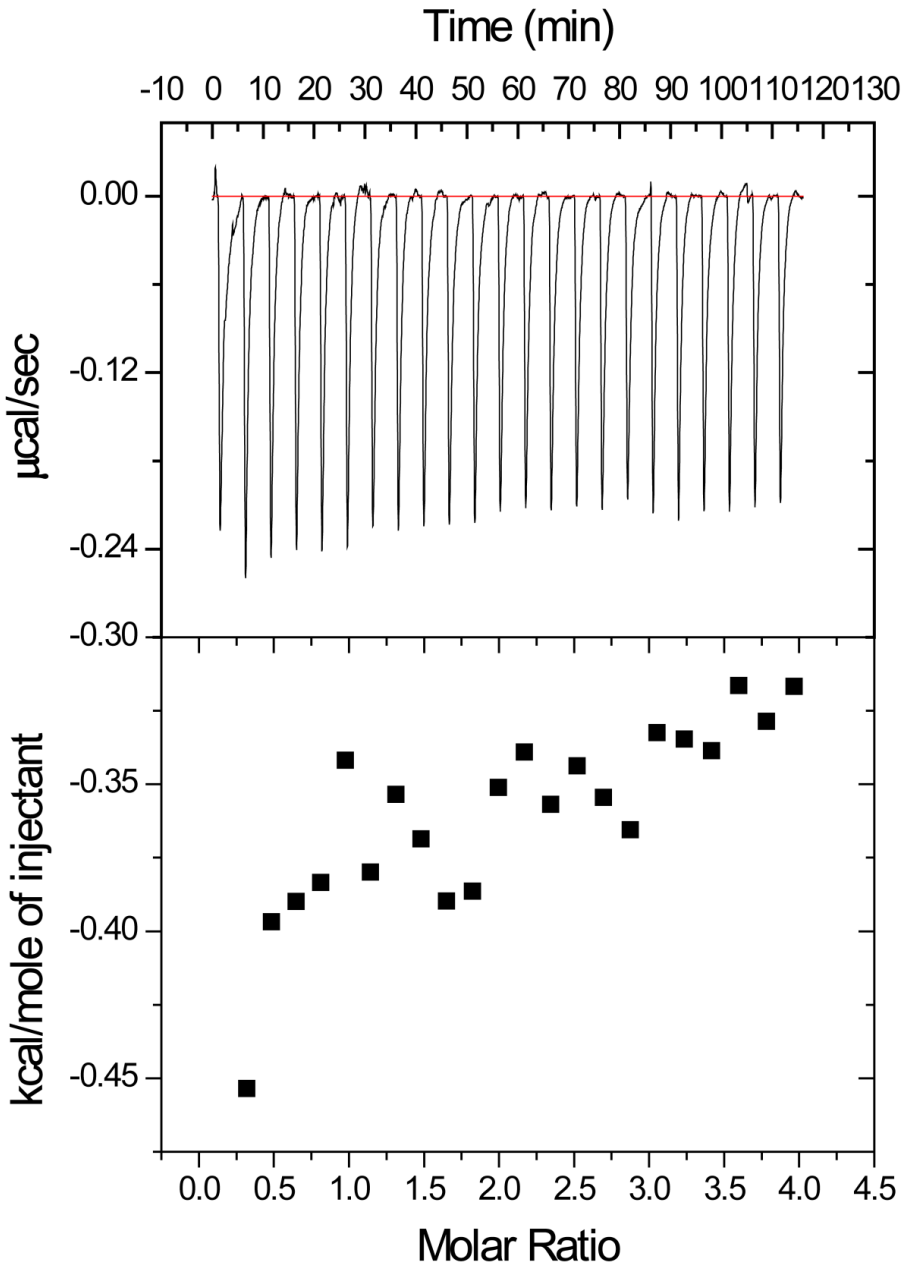

Figure 4.8: ITC buffer controls at 310 K. Xenon-saturated water (3.31 mM) titrated into 20 mM phosphate buffer, pH 7.5.

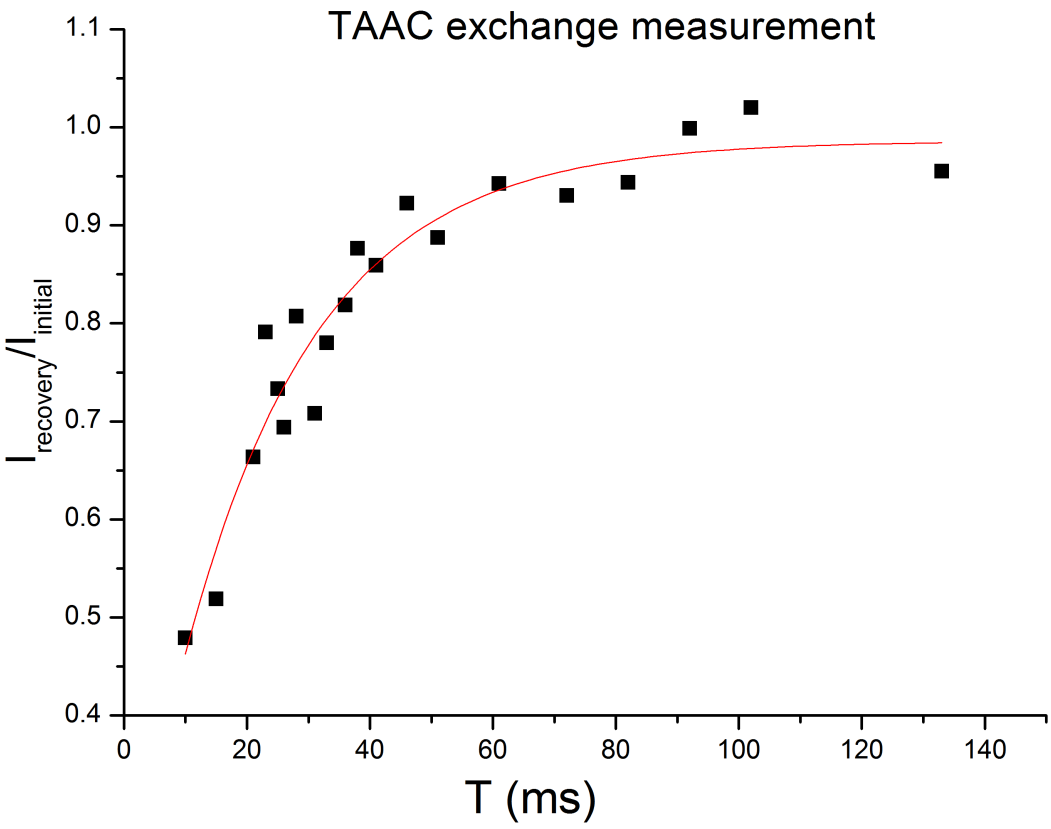

Figure 4.9: Xe-TAAC exchange lifetime measurement by selective EXSY at 297 K. The horizontal axis denotes the mixing time between two consecutive excitations. The vertical axis indicates the ratio of the integrated intensities of Xe@TAAC signals, exchange recovered vs. equilibrium. Data were exponentially fitted to give an exchange lifetime, $\tau_{exch} = 22 \pm 3$ ms. This exchange lifetime is in good agreement with linewidth measurements made at 300 K (Table4.1).

Chapter 5

Anthrax Detection and Bacterial Spore Analysis Using ^{129}Xe Hyper-CEST NMR

5.1 Background

A subset of bacteria produce a highly resistant, dormant cell type, called the spore, which is produced in response to specific stresses, most notably starvation [105]. Although essentially metabolically dormant [106], the spore can break dormancy (a process called germination) very soon after the spore detects specific signals (including, in some species, amino acids) that likely indicate conditions for resuming growth are present. A small fraction of spore-forming species are pathogenic, including *Clostridium difficile*, one of the most important health-associated infectious agents [107], as well as *Bacillus anthracis*, a major biothreat agent [108]. The threat posed by these and other pathogenic species has intensified efforts to better understand the roles of spore structures in resistance, and to improve methods of spore detection. The spore's unusual—and incompletely understood—structural integrity in the face of extreme temperatures, mechanical stress, chemical denaturation and other stresses is essential to maintaining viability as well as resisting host defense and decontamination [109]. A molecular understanding of how the structures encasing the spore provide this protection has been a goal of basic research for many decades [106]. Here, we demonstrate a ^{129}Xe nuclear magnetic resonance (NMR) spectroscopic method that allows both sensitive analysis and detection of intact spores in aqueous solution, without any further sample preparation.

Spores have a distinctive architecture, composed of a series of concentric layers, each of which contributes to resistance and other spore properties (Figure 5.1a,

b) [109, 110]. In some species, including *B. anthracis*, the outermost spore layer is the exosporium, a pleomorphic shell composed of proteins and glycoproteins (Figure 5.1a). The exosporium is present in pathogenic and nonpathogenic species (for example, see Traag et al. [111]). Beneath the exosporium (and separated by a gap) is the coat, which is present in all bacterial spores (Figure 5.1b) [110]. Although these two layers play key roles in spore resistance, their chemical properties and molecular organization remain incompletely understood. This lack of information hinders efforts to improve anti-spore therapeutics, decontamination and spore detection. In particular, sensitive methods for spore detection that do not require major sample preparation and discriminate between pathogenic and nonpathogenic spore-forming species are needed. No existing method achieves all these goals. In particular, identifying species without DNA sequencing has been especially challenging. For example, fluorescence-based assays have been developed that readily detect bacterial spores [112–116], but cannot discriminate between species, because the target analyte, dipicolinic acid (DPA), is present in bacterial spores of all species. Methods that identify subcellular structures in spores that vary among species (and, in particular, between at least certain pathogenic and non-pathogenic species) could be very helpful to improved pathogen detection.

NMR spectroscopy has been used previously to analyze spore contents [117–119] but typically offers limited detection sensitivity, due to small polarization of the nuclear spin reservoir, where the difference in spin populations aligned parallel or

anti-parallel to an external magnetic field at thermal equilibrium is typically just 10 in a million nuclei. Thus, significantly enhanced NMR signals can be obtained via hyperpolarization techniques capable of generating a nuclear spin polarization level approaching 100% [37, 120]. Our laboratory [21, 23, 24, 56, 121] and others [27,29,55,85,92,100,122–128] have explored the noble gas nucleus ^{129}Xe, which has one-half nuclear spin number (I = ½), and can be hyperpolarized (HP) to near unity by spin-exchange optical pumping [129]. To make the technique more sensitive for demanding applications, chemical exchange provides another source of NMR signal amplification. When exchanging magnetic species are present, chemical exchange saturation transfer (CEST) can achieve signal amplification based on cumulative magnetization transfer through selective saturation [13]. This gives the possibility of designing extremely sensitive contrast agents that respond to various exchange events, with techniques known as PARACEST [130] and LIPOCEST [84]. More recently, the analogous technique involving HP ^{129}Xe (Hyper-CEST) was developed [85]. Until now, this technique has only been applied to ^{129}Xe exchange between bulk aqueous solution and high-Xe-affinity, water-soluble organic host molecules (i.e., cryptophanes) or organic solvents. This work provides the first demonstration of using Hyper-CEST ^{129}Xe NMR to interrogate the structure of a biological sample.

Here we present Hyper-CEST NMR analysis of wild type and mutant *B. anthracis* and *B. subtilis* spores, where detection limits of 10^5-10^9 spores per milliliter were achieved in aqueous solution. ^{129}Xe gas irradiated by radio frequency pulses

in the spore interior efficiently transfers loss of magnetization to the bulk solution, which provides contrast between different spore structural components. We analyzed strains of *B. anthracis* that vary in exosporium structure and strains of *B. subtilis* that vary in coat structure. These strains show readily distinguishable Hyper-CEST behaviors, in a manner consistent with the hypothesis that spore layers cause variations in the rate of xenon diffusion between aqueous solution and the spore interior. We speculate that these signature differences are the consequence of as yet poorly understood chemical and structural features of the exosporium and coat. By determining the Xe accessibility of the spore interior to the outer environment, Hyper-CEST NMR provides a rapid, nondestructive measure of molecular porosity. Importantly, this methodology distinguishes between spores with and without exosporia. As a result, in combination with other technologies, it could be a component of a novel method or device to identify *B. anthracis* spores.

5.2 Results and Discussions

5.2.1 Strains

All strains are in either the attenuated Sterne strain 34F2 (for *B. anthracis*) or PY79 (for *B. subtilis*) backgrounds. The *B. anthracis* strain ADL986 lacks the exosporium (due to a mutation in *cotE*) and the strain ADL2260 possesses the innermost layer of the exosporium (the basal layer) but lacks the hair-like projections or nap that

project from the basal layer-outer surface, due to *BclA* mutation [131, 132]. The *B. subtilis* strains ADL25 and ADL57 lack the outer layers of the coat, or almost the entire coat, due to mutations in *cotE*, or *cotE* and *gerE*, respectively [133, 134]. We note that while the genes both named *cotE* in *B. anthracis* and *B. subtilis* are indeed orthologous, their mutant phenotypes have important differences between these two species, as noted.

5.2.2 Hyper-CEST Experiment with Spores

Before starting the Hyper-CEST experiment each time, fresh HP Xe was delivered into a 10 mm thick NMR tube, and bubbled through a 3-mL liquid sample. Right before the pulse sequence started, HP Xe bubbling was stopped by a couple of solenoid valves to stabilize the liquid sample for NMR acquisition. The NMR tube was airtight during the Hyper-CEST experiment, which is achieved by a homebuilt continuous-flow HP Xe delivery setup [121].

Figure 5.1c illustrates the Hyper-CEST experiment involving spores. As a starting point for all sets of Hyper-CEST experiments, a consistent amount of fresh HP Xe resides in the sample suspension. As the first step of the Hyper-CEST pulse sequence, DSnob-shaped 180-degree selective pulses were looped numerous times continuously, at frequencies of interest. Pulse power was calibrated to give maximum saturation performance. Xenon resonances within the RF pulses selected frequency range were depolarized, with the aid of chemical exchange, thereby ac-

celerating depolarization of the whole xenon sample. After the overall polarization was reduced by saturation pulses and chemical exchange, the sample was irradiated with a 90-degree hard pulse to observe the final magnetization state of ^{129}Xe in solution. More detailed description for the pulse sequence can be found in Figure 2.6.

5.2.3 Hyper-CEST Profile for Spores

Multiple (100-500) selective 180-degree radio-frequency (RF) pulses were delivered to spore samples at the various resonance frequencies, within a duration between 1.0 s and 9.5 s. By scanning the saturation frequencies, different Xe(aq) signal intensities were acquired and plotted as the exchange profile. At frequencies of observable Xe depolarization, HP Xe and depolarized Xe were dynamically exchanging among distinguishable chemical environments related to spores.

Figure 5.2 shows the profile of wild type *B. anthracis* at 1.2×10^9 cfu/mL, in 188-203 ppm frequency range, and at 0.5 ppm resolution. A Xe(spore) signal was observed to be actively exchanging with the Xe(aq) signal. After the profile was fit by Voigt line shape, two signals were found. The secondary peak at 196.3 ppm (7.6 ppm wide) is assigned to Xe(spore); while the main peak at 193.4 ppm (4.5 ppm wide) is assigned to Xe(aq). Similar profiles are also observed for all spore samples listed above (Figures 5.4, 5.5, 5.6, 5.7, 5.8), at a much lower density of 1.2×10^7 cfu/mL. The Xe(spore) peak chemical shifts are summarized in Table 5.1.

Except for *B. anthracis*, all Xe(spore) signals were found at 198 ± 1 ppm. This small difference may be attributable to the intact exosporium present in wild type *B. anthracis* and not in the other strains analyzed.

5.2.4 Depolarization Rate Measurement for Spores

To make comparison between Hyper-CEST performances across spore strains, and to make the CEST effect more observable, HP Xe depolarization background needs to be removed. Two frequencies, 197.5 ppm and 188.9 ppm, were selected for Hyper-CEST "on" and "off" resonance, and kept the same in the two series of data points. The number of saturation pulses in the sequence was increased from 0 to 2000 in steps of 200 (Figure 5.3a), corresponding to saturation times between 0 s and 38 s. Meanwhile, the Xe(aq) signal decreased exponentially as more pulse power was applied to the sample. The exponential decay time (T_1) of HP Xe, for the two selected frequencies, can be extracted from fitting the decay curves. In Figure 5.3, the decay time constants were fitted to be 16.5 s (on) and 29.6 s (off). The existence of chemical exchange with the "on resonance" group greatly accelerated the rate.

5.2.5 Saturation Transfer Efficiency (Hyper-CEST contrast)

A more direct way to quantify the contrast generated by the Hyper-CEST experiment is to compute the saturation transfer efficiency (ST), which is directly proportional to MR image contrast:

$$ST = \sum_k \frac{I_{off}^k - I_{on}^k}{I_{off}^k} \frac{L^k}{\sum_{k'} L^{k'}} \tag{5.2.1}$$

In equation 5.2.1, I represents the integral of Xe(aq) signal acquired in a Hyper-CEST experiment with set saturation frequency, duration, and power. L represents the duration of Hyper-CEST pulse sequences, which is the sum of time spent in shaped saturation pulses and delays. The summing index k indicates the experiment number in Figure 5.3a. This weighted sum, corresponding to ST, provides the proportion of saturation-transferred magnetization, over the initial value. Therefore ST quantifies the efficiency of the Hyper-CEST experiment for each sample.

5.2.6 Enhanced Hyper-CEST from Mutated Exosporium

We analyzed one *B. anthracis* strain lacking the exosporium (strain ADL986, with mutation in cotE [132]) and one missing the major exosporium protein BclA (strain ADL2260) [131]. *B. subtilis* spores lack an exosporium. In Table 5.1, ST is listed for all strains at 1.2×10^7 cfu/mL. Both strains gave dramatically enhanced Hyper-CEST contrast. Strain ADL986 had exosporium removed strongly increased sensitivity to Hyper-CEST, consistent with the interpretation that the lack of the hair-like projections on the exosporium surface increases sensitivity to Hyper-CEST. Significantly, detection of wild type *B. anthracis* by Hyper-CEST required a 100-fold higher concentration than the other strains.

5.2.7 Enhanced Hyper-CEST from *B. subtilis* Spores with Coat Defects

To determine whether Hyper-CEST can be used to monitor also the molecular features of the spore coat, we analyzed wild type *B. subtilis* and strains lacking the outer layers or almost all of the coat (strains ADL25 and ADL57, respectively) [133, 134]. We found that in the absence of the outer layers of the coat, the Hyper-CEST contrast was enhanced by more than 2-fold (comparing PY79 and ADL25, Figure 5.3b). In strain ADL57 (lacking almost the entire coat), we measured an additional 2-fold increase in Hyper-CEST contrast. We conclude that spores lacking coat layers are more sensitively detected by Hyper-CEST. We infer that this increase is due to the spore interior being more accessible to xenon in solution. To measure the limit of detection of the most Xe-accessible strain, we performed Hyper-CEST on ADL57 at concentrations from 10^4 to 10^6 cfu/mL. A clear Hyper-CEST contrast was observable at 10^5 cfu/mL (Figure 5.9).

5.2.8 Possible Origin of Xenon Exchange in Spores

With a ∼4.3-angstrom diameter, and a very polarizable electron cloud, Xe is known to exhibit affinity for sub-nanometer-sized void spaces in materials, proteins, and organic cages [16, 17, 135, 136]. Xe is also very sensitive to its environment, as reflected by the 4 ppm chemical shift difference between the Xe(aq) and Xe(spore) NMR peaks. Our data are consistent with xenon occupying sites in the spore

interior, where the chemical shift will differ from water and result in a reservoir for exchange behavior. Experiments are underway to verify the primary site(s) occupied by Xe in the spore interior. However, as highlighted above, spores with fewer outer layers presented stronger Hyper-CEST contrast. The best contrast was observed with strain ADL57, which largely lacks the coat. This argues that the cortex, inner membrane and/or core are the site(s) of Xe exchange. Notably, by producing a discrete Xe-bound resonance frequency, the spore must possess a significant number of Xe binding sites, albeit likely with low Xe affinity ($K_A \sim$ 10-100 M^{-1}, as seen for many proteins [48–51]). The core, the inner-most spore compartment, is one likely site of Xe occupancy, as it contains compacted, dehydrated DNA buried in crystalline Ca^{2+}-dipicolinic acid [109]. Additionally, the exchange rate must be fast compared to the timescale of the HP ^{129}Xe longitudinal relaxation time ($T_1 \sim$75 s) in order to produce the observed enhancement in detection sensitivity relative to direct detection schemes. Notably, no "bound" ^{129}Xe NMR signal is observed for any of the spore samples at concentrations of 1.2×10^7 cfu/mL.

These findings argue that the bacterial spore interior is accessible to small hydrophobic molecules of the size of Xe. Small molecules, such as methane, which differ somewhat from Xe in size, hydrophobicity, and diffusion rate, may also be able to penetrate through the spore protection layers, giving further opportunity to analyze the spore structure.

5.3 Methods

5.3.1 NMR Sample Preparation

Spores were prepared as described in previous references [132]. Spore number was measured by counting colony-forming units. Before each NMR experiment, the spores were suspended in MilliQ water to desired number densities (1.2×10^9 cfu/mL for strain 34F2, 1.2×10^7 cfu/mL for all samples, and 1.2×10^4 -1.2×10^7 cfu/mL for ADL57).

5.3.2 Hyperpolarized ^{129}Xe NMR Setup

All NMR spectra were acquired by a Bruker BioDRX 500 MHz NMR spectrometer. RF pulse frequency for ^{129}Xe was 138.12 MHz. Spore suspension samples were observed using a 10-mm PABBO NMR probe. HP ^{129}Xe was generated using a home-built ^{129}Xe hyperpolarizer, based on the commercial model IGI.Xe.2000 by GE. A gas mixture of 89% nitrogen, 10% helium, and 1% natural abundance xenon (Linde Group, NJ) was used as the hyperpolarizer input. ^{129}Xe was hyperpolarized to 10-15% after optical pumping of Rb vapor with 795 nm circularly polarized laser.

Sample temperature was controlled by VT unit on NMR spectrometer to 278 ± 1 K. All acquired NMR spectra using the Hyper-CEST pulse sequence were processed with 10 Hz Lorentz broadening. Xe(aq) signal intensities under different saturation frequencies and/or times were integrated and relative values were used for further

derivations.

5.4 Conclusions

We have successfully analyzed various bacterial spores using a sensitive Hyper-CEST NMR technique. The ability of Xe to diffuse readily within the spore layers and interact with the interior to give rise to Hyper-CEST signal (without cryptophane or other engineered binding sites), suggests many new applications for Hyper-CEST NMR in biophysics and materials science. In this example, the most Xe-accessible spores were detected at a concentration of just 10^5 cfu/mL, which is $\sim$7 orders of magnitude more sensitive than previous efforts at spore detection using NMR [117,118]. Moreover, this result did not require specialized sample preparation and was achieved without spore destruction, thereby allowing downstream analysis of the sample.

The finding that the Hyper-CEST signal increased in spores where outer structures were absent strongly suggests that Xe in aqueous solution gains ready access to the interior in a manner such that the rate of the exchange process depends on the thickness and/or composition of the outer layers present. We note, therefore, that Hyper-CEST could be an especially powerful method to distinguish between spores that are morphologically similar, but differ in characteristics that mediate Xe exchange, and that this technique also provides a novel method for spore detection. The finding that the exosporium effectively limits Xe entry into the spore

is notable and is consistent with the view that the exosporium acts as a molecular sieve. Taken as a whole, our results show that Hyper-CEST NMR provides a novel method for noninvasive spore detection and a powerful tool for probing the physical and chemical properties of the spore interior. We argue that, in combination with genetic manipulation of spore ultrastructure, Hyper-CEST can generate new insights into spore composition and function that have previously been difficult or impossible to analyze.

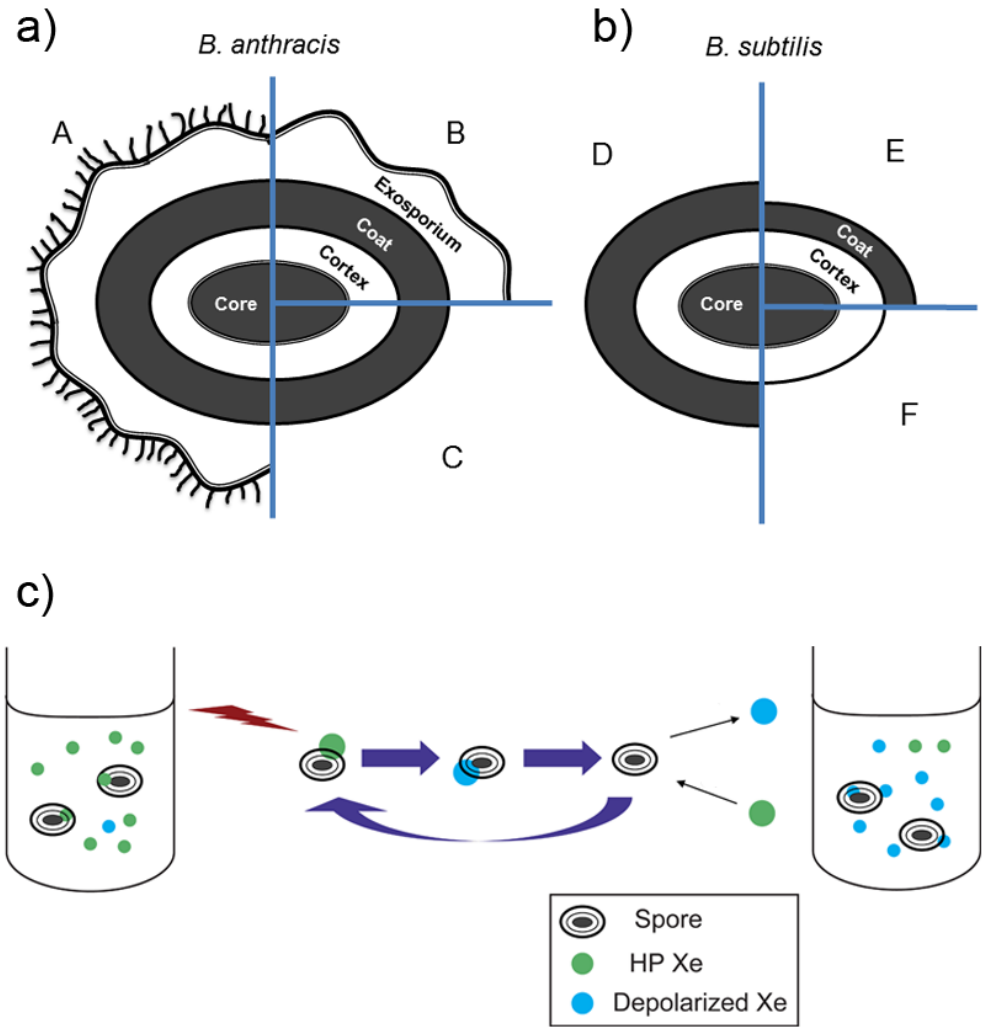

Figure 5.1: ^{129}Xe Hyper-CEST experiment with spores. a) *B. anthracis* strains: (A) 34F2, (B) ADL2260, (C) ADL986; b) *B. subtilis* strains: (D) PY79, (E) ADL25, (F) ADL57; c) Scheme showing Hyper-CEST experiment with spores.

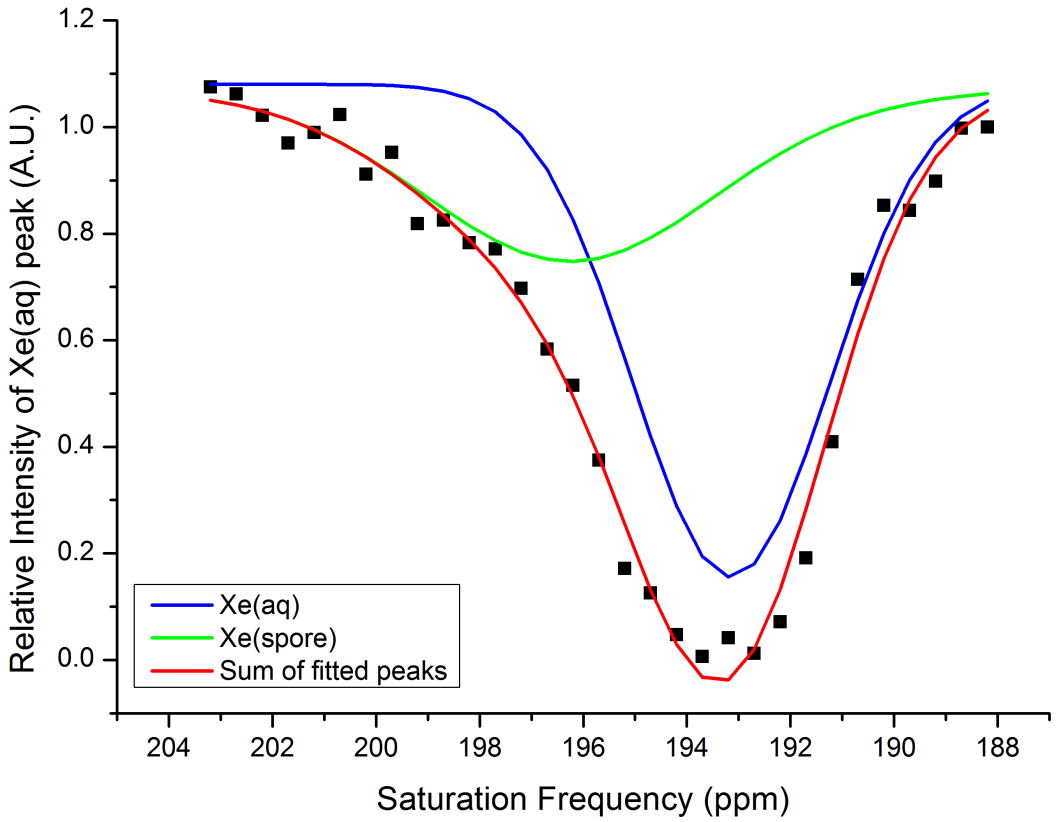

Figure 5.2: Hyper-CEST profile of wild type *B. anthracis* spore at 1.2×10^9 cfu/mL with 600 pulse cycles for saturation exchange (11.6 s saturation time). Profile acquired at 0.5 ppm resolution, at 278 K. Two peaks (193.4 ppm and 196.2 ppm) are shown for the water and spores, respectively.

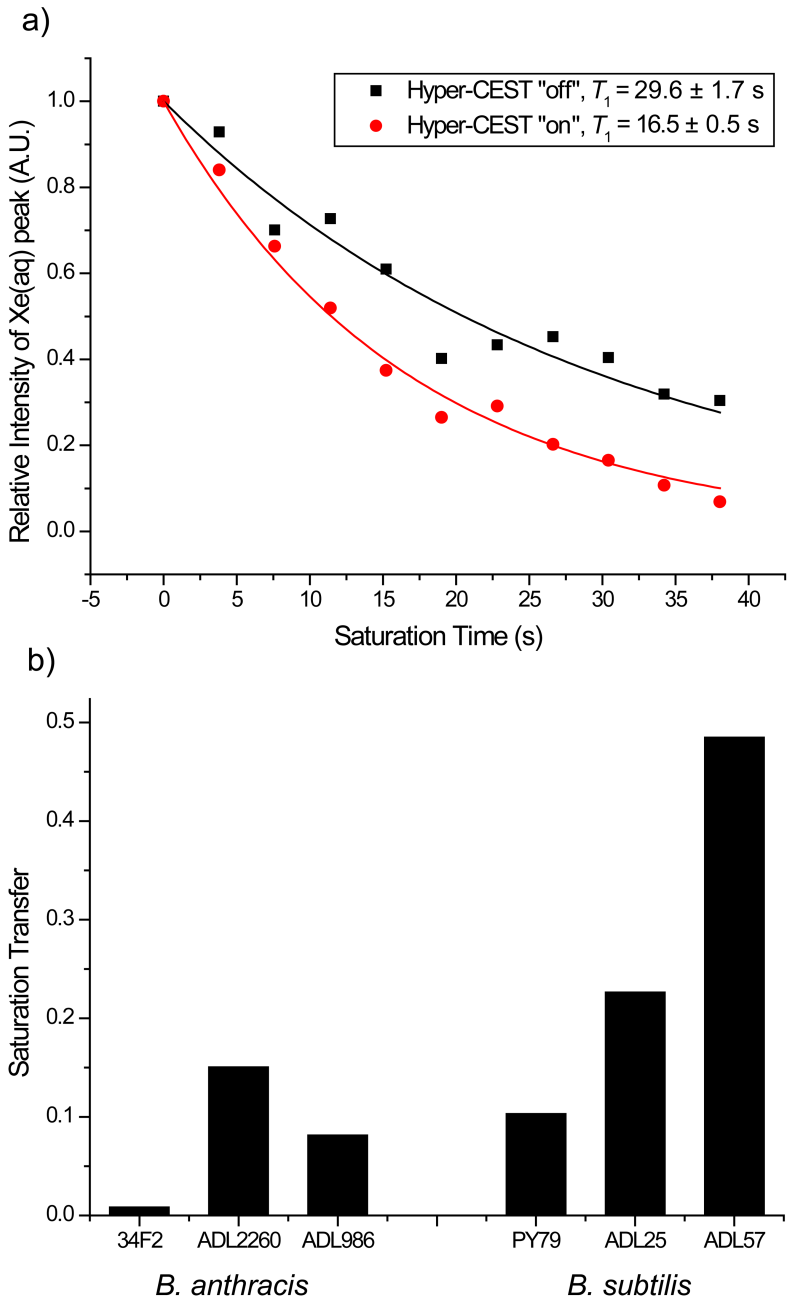

Figure 5.3: Hyper-CEST saturation transfer efficiency across spore strains. a) Hyper-CEST depolarization curve of wild type *B. anthracis* spores at 1.2×10^9 cfu/mL. Saturation frequencies were 197.5 = (193.2 + 4.5) ppm and 188.9 = (193.2 − 4.5) ppm, for "on" and "off" resonance, respectively. Decay time constants (T_1) were determined to be 16.5 s (on) and 29.6 s (off). b) Comparison of saturation transfer efficiencies across six spore strains. All strains were observed at 1.2×10^7 cfu/mL.

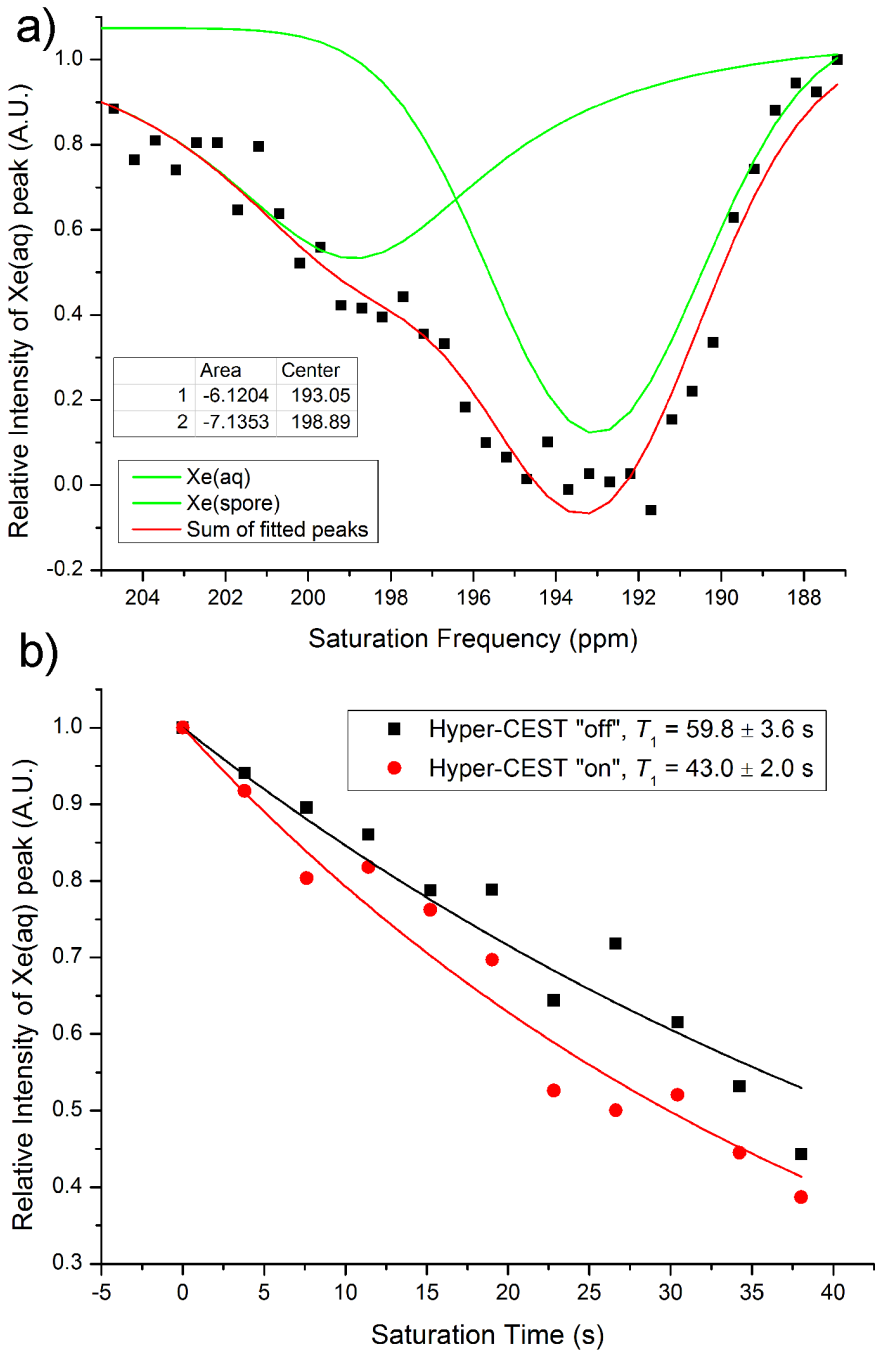

Figure 5.4: (a) Hyper-CEST profile of *B. anthracis* ADL2260 spores at 1.2×10^7 cfu/mL with 300 pulse cycles for saturation exchange; (b) Hyper-CEST depolarization curve of *B. anthracis* ADL2260 spores at 1.2×10^7 cfu/mL.

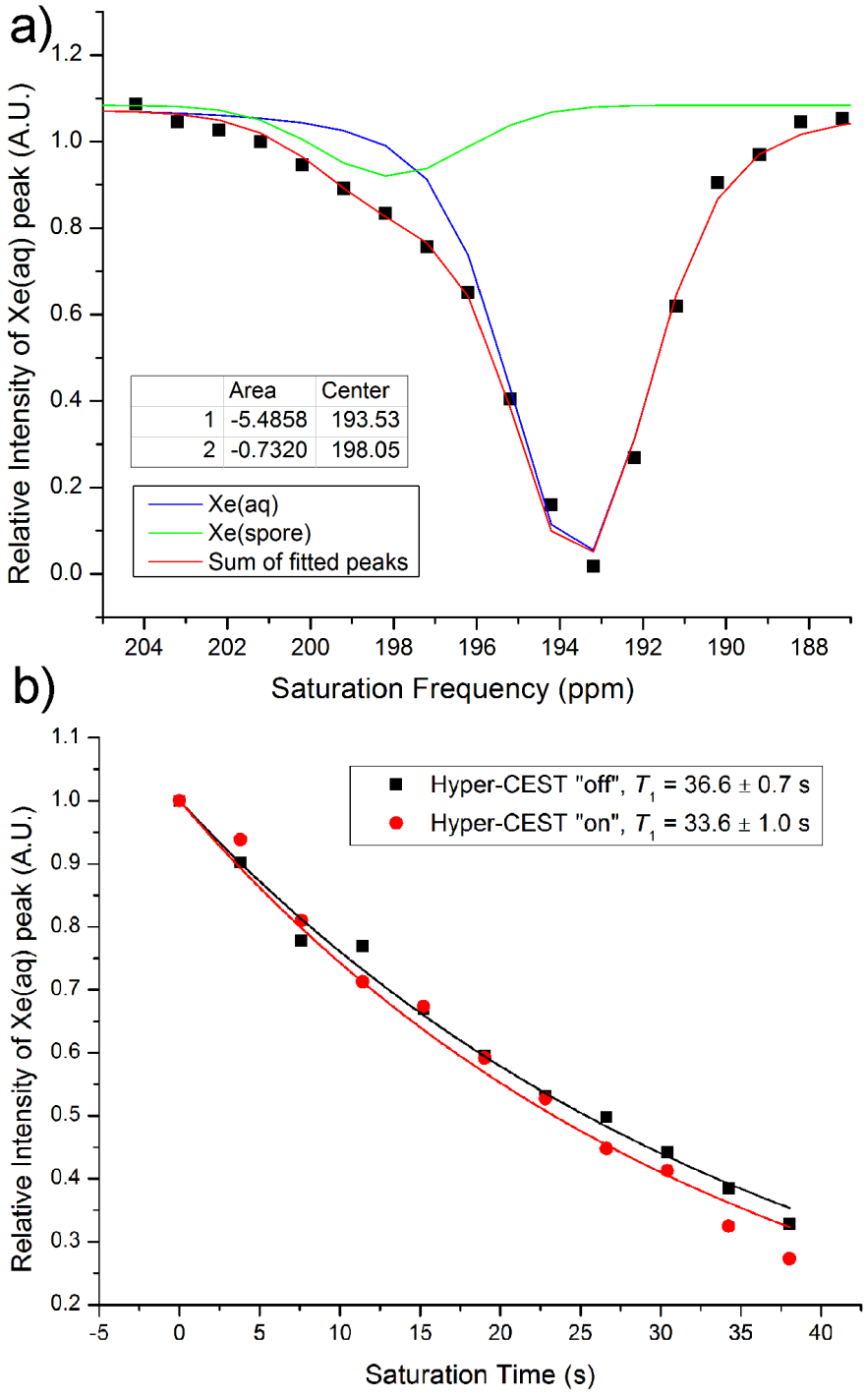

Figure 5.5: (a) Hyper-CEST profile of *B. anthracis* ADL986 spores at 1.2×10^7 cfu/mL with 200 pulse cycles for saturation exchange; (b) Hyper-CEST depolarization curve of *B. anthracis* ADL986 spores at 1.2×10^7 cfu/mL.

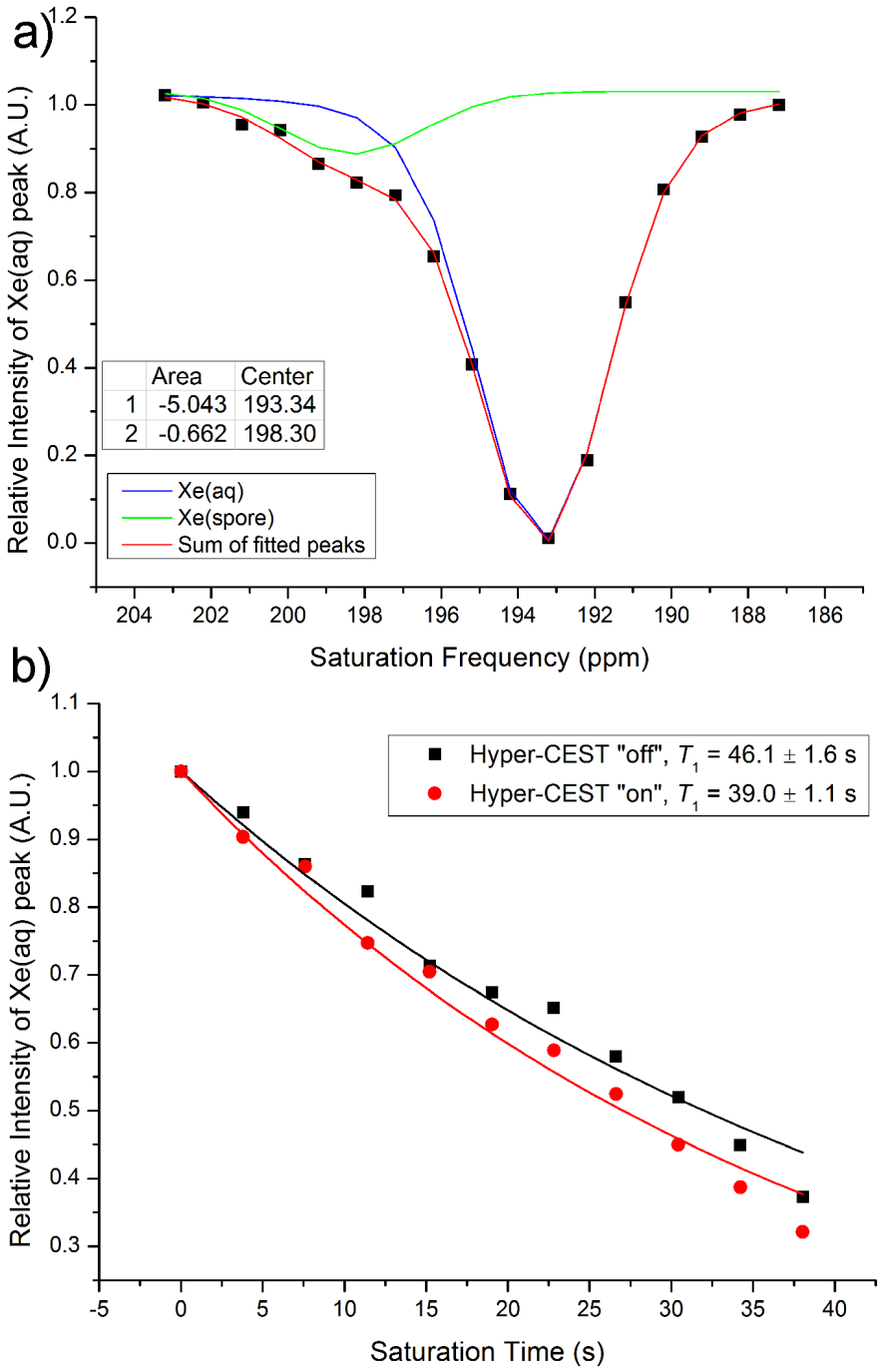

Figure 5.6: (a) Hyper-CEST profile of *B. subtilis* PY79 spores at 1.2×10^7 cfu/mL with 200 pulse cycles for saturation exchange; (b) Hyper-CEST depolarization curve of *B. subtilis* PY79 spores at 1.2×10^7 cfu/mL.

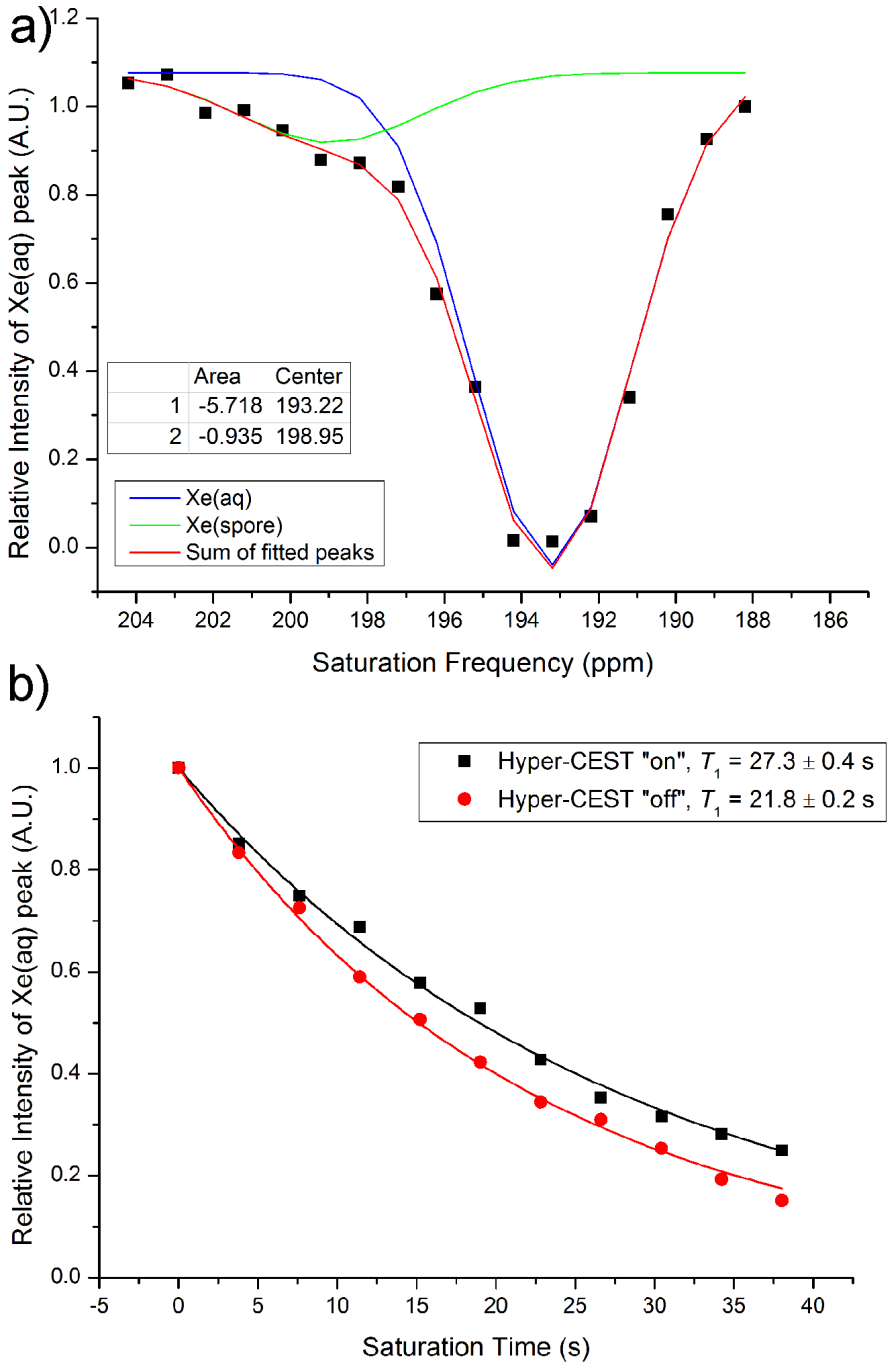

Figure 5.7: (a) Hyper-CEST profile of *B. subtilis* ADL25 spores at 1.2×10^7 cfu/mL with 200 pulse cycles for saturation exchange; (b) Hyper-CEST depolarization curve of *B. subtilis* ADL25 spores at 1.2×10^7 cfu/mL.

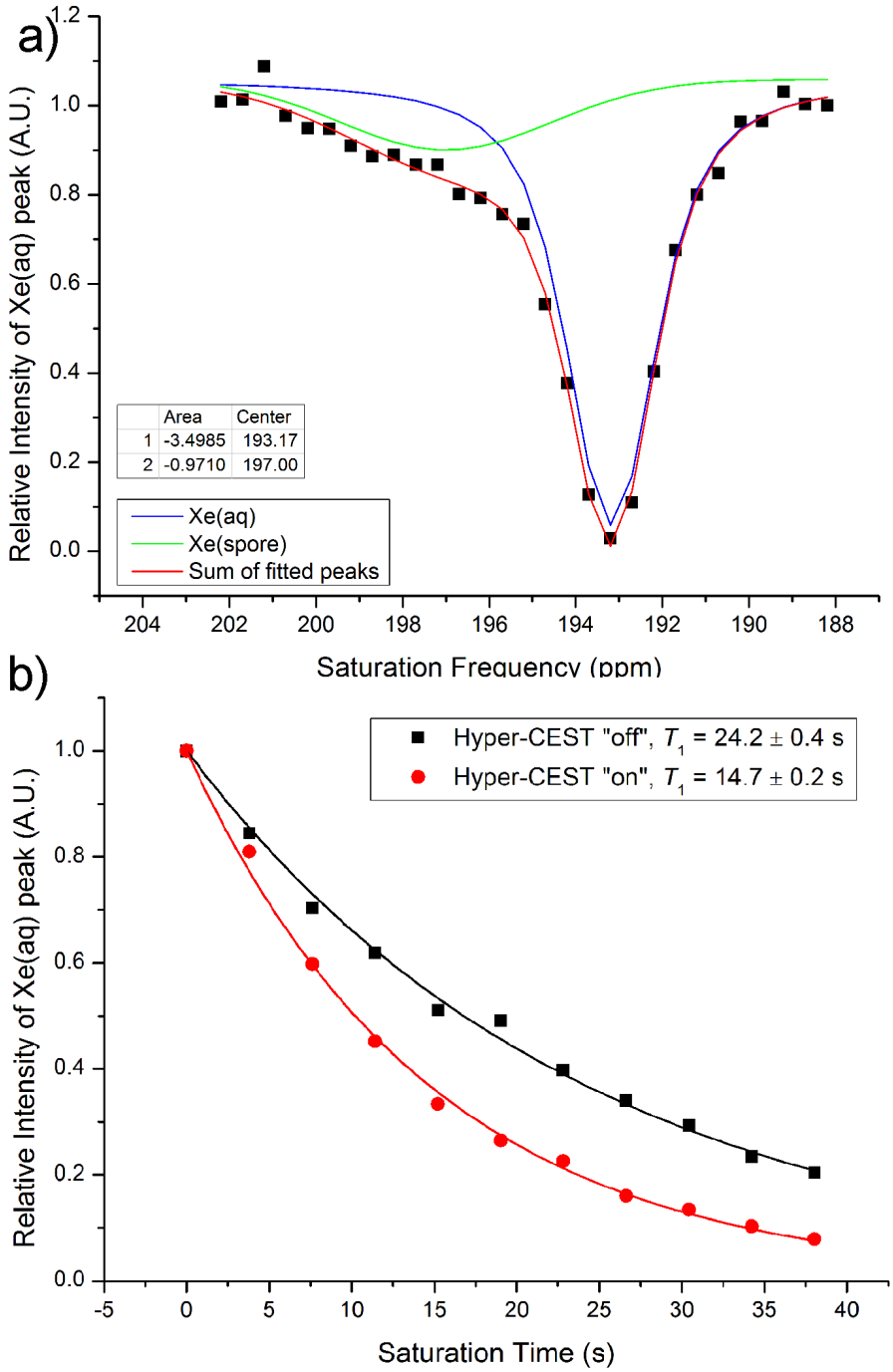

Figure 5.8: (a) Hyper-CEST profile of *B. subtilis* ADL57 spores at 1.2×10^7 cfu/mL with 200 pulse cycles for saturation exchange; (b) Hyper-CEST depolarization curve of *B. subtilis* ADL57 spores at 1.2×10^7 cfu/mL.

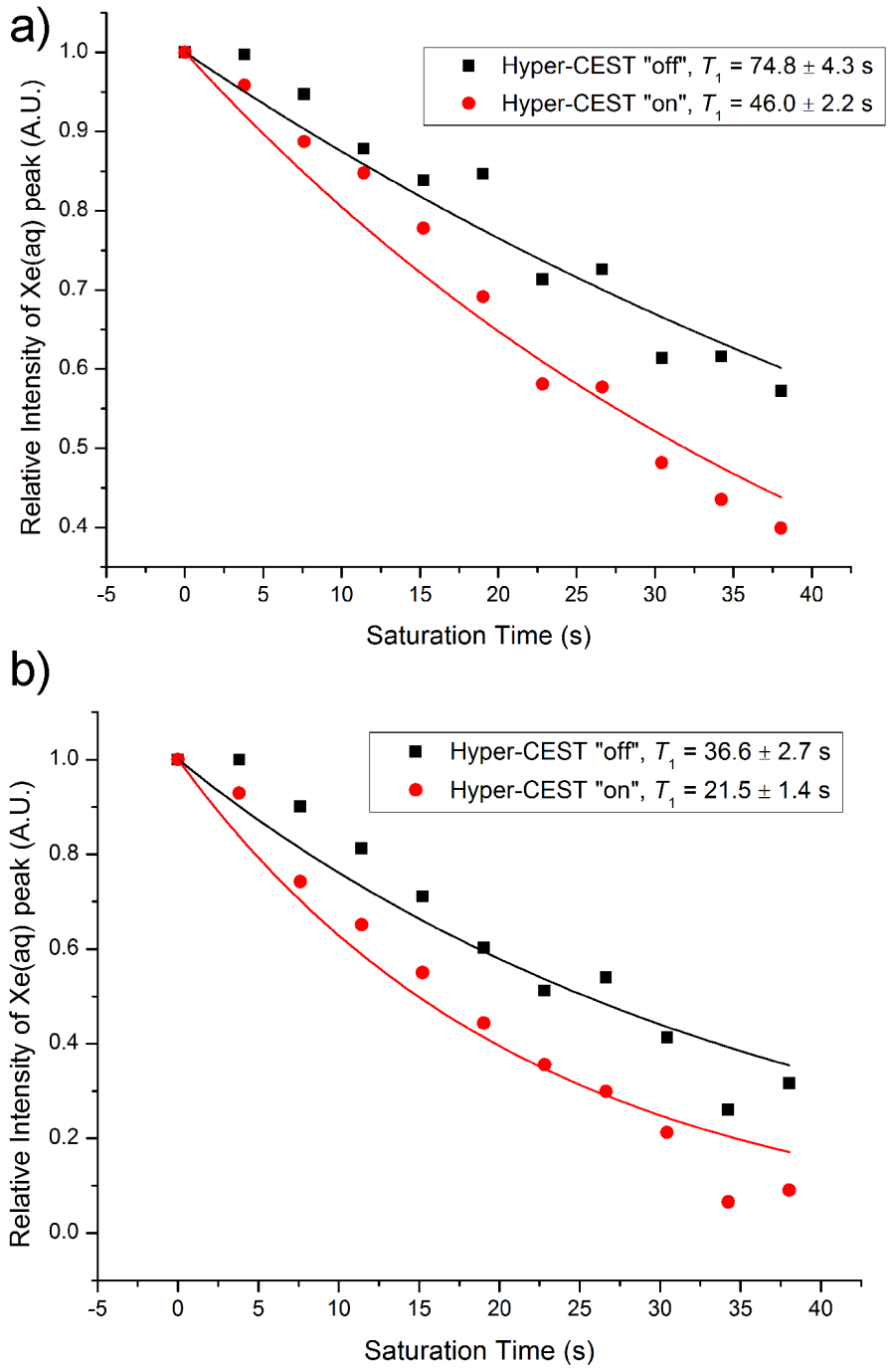

Figure 5.9: (a) Hyper-CEST depolarization curve of *B. subtilis* ADL57 spores at 1.2×10^5 cfu/mL. (b) Hyper-CEST depolarization curve of *B. subtilis* ADL57 spores at 1.2×10^6 cfu/mL.

Table 5.1: Saturation transfer (ST) efficiency and exchange signal chemical shift for six spore strains.

Spore	Strain	Saturation Transfer Efficiency	^{129}Xe(spore) NMR signal chemical shift (ppm)
B.anthracis	34F2	0.01	196±8
B.anthracis	ADL2260	0.15	199±2
B.anthracis	ADL986	0.08	198±1
B.subtilis	PY79	0.10	198±1
B.subtilis	ADL25	0.22	199±2
B.subtilis	ADL57	0.48	197±1

Chapter 6

Summary

This thesis aimed to increase the applicability of ^{129}Xe NMR/MRI techniques by ^{129}Xe hyperpolarization and chemical exchange saturation transfer, for medical and/or molecular imaging. Also, attempts were made to broaden the scope of hyperpolarized ^{129}Xe as a biophysical probe, for applications other than imaging.

6.1 Biosensor Multiplexing

Previous results from the Dmochowski lab and NMR studies described in this work show that cryptophanes can be conjugated with molecular recognition moieties (enzyme substrates, enzyme inhibitors, etc). Upon interacting with the targeted molecule, chemical shift changes are generated in the ^{129}Xe NMR spectrum, even for small perturbations of protein conformation or even for a peptide undergoing helix formation (chapter 3). The usage of a "cocktail" of multiple biosensors in the same experiment is viable, by guaranteeing that they do not interfere in the ^{129}Xe NMR frequency domain under measurement.

Under the Hyper-CEST scheme, xenon is observed to exchange between different sites at distinctive chemical shifts. Multi-site exchange behaviors arise when biosensors targeting different biomarkers are present inside the same xenon reservoir. This can be a double-edged sword in many cases as biosensors may compete for limited HP Xe, or may produce a much enhanced Hyper-CEST effect if they work synergically. More interestingly, as many different xenon reservoirs are present *in vivo*, multiplexed Hyper-CEST of the same biosensor with more than one xenon

reservoir could potentially be observed.

6.2 *In vivo* ^{129}Xe Hyper-CEST MRI

^{129}Xe MRI has previously been applied to both lab animals and human lungs. More, human clinical trials with various proton CEST imaging agents are currently underway. A natural extension is the application of *in vivo* ^{129}Xe Hyper-CEST MRI. From the viewpoint of this work, two main challenges are likely to emerge.

First, the Xe concentration, hyperpolariation level, and diffusion rate need to be determined and modeled in an imaging subject, given a particular HP Xe delivery method. In most organisms, no endogenous Xe is observable by MRI. If the Xe MRI scheme is not correctly predicted, the background for Hyper-CEST can report false positives/negatives. A hollow region on a Hyper-CEST MRI may indicate contrast generated by Hyper-CEST agents, however, it could also originate from anatomical structures that are impermeable to Xe gas.

Second, the pulse sequences for Hyper-CEST imaging can be difficult to implement. The pulse sequences and signal processing practices in conventional proton MRI, proton CEST, chemical shift imaging, and hyperpolarized ^{4}He/^{13}C/^{129}Xe MRI, are not well-suited for Hyper-CEST. For example, in HP ^{13}C imaging, a commonly applied method is to use small-flip-angle pulses to signal average multiple transients, thus minimally perturbing the hyperpolarized ^{13}C spin reservoir. This allows as many transients as possible, before ^{13}C hyperpolarization level drops due

to relaxation. However, to image Hyper-CEST contrast, the depolarization effect is the crucial observable. If it's necessary to acquire multiple transients for signal-averaging, multiple HP Xe deliveries need to be employed.

6.3 Xenon As a Useful Biophysical Probe

For early cancer detection and other imaging applications using HP ^{129}Xe, previous and ongoing efforts have utilized synthetic organic host molecules. In the literature, ^{129}Xe NMR has also been used in zeolite characterization, molecular host recognition [16, 17], and it also has good permeability to biological cells [29].

This thesis has demonstrated that HP Xe can be used directly in bacterial spore structure analysis. More, it's possible to use Hyper-CEST with analytes that have xenon exchanging sites which resonate at a distinguishable frequency. As mentioned previously, the exchange rate timescales of xenon must lie between the ^{129}Xe relaxation time (100 s) and NMR sampling time interval (10^{-5} s). We predict these criteria will be met by a very broad range of samples, including human tissues, biological cells, transient forming cavities in proteins, etc.

Appendices

Appendix A

^{129}Xe Hyperpolarizer Setup

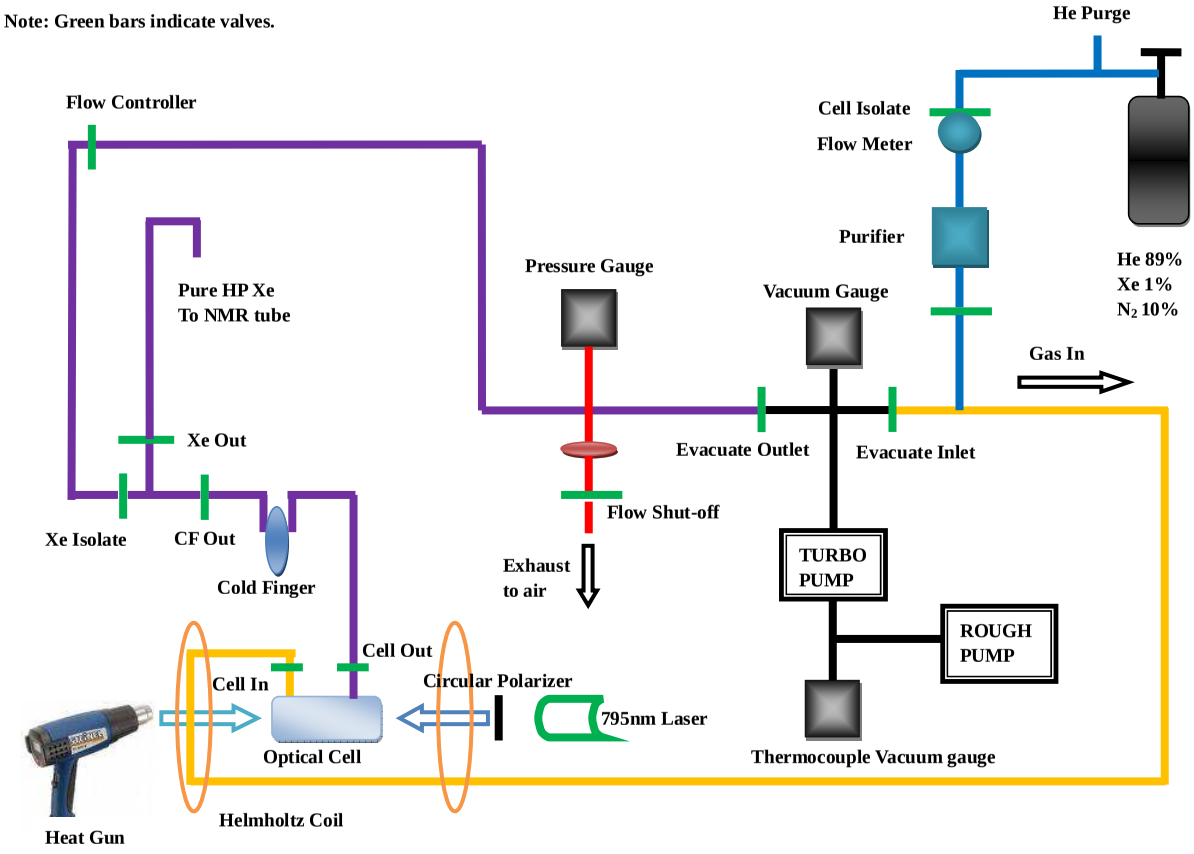

Figure A.1: Scheme of home-built ^{129}Xe hyperpolarizer

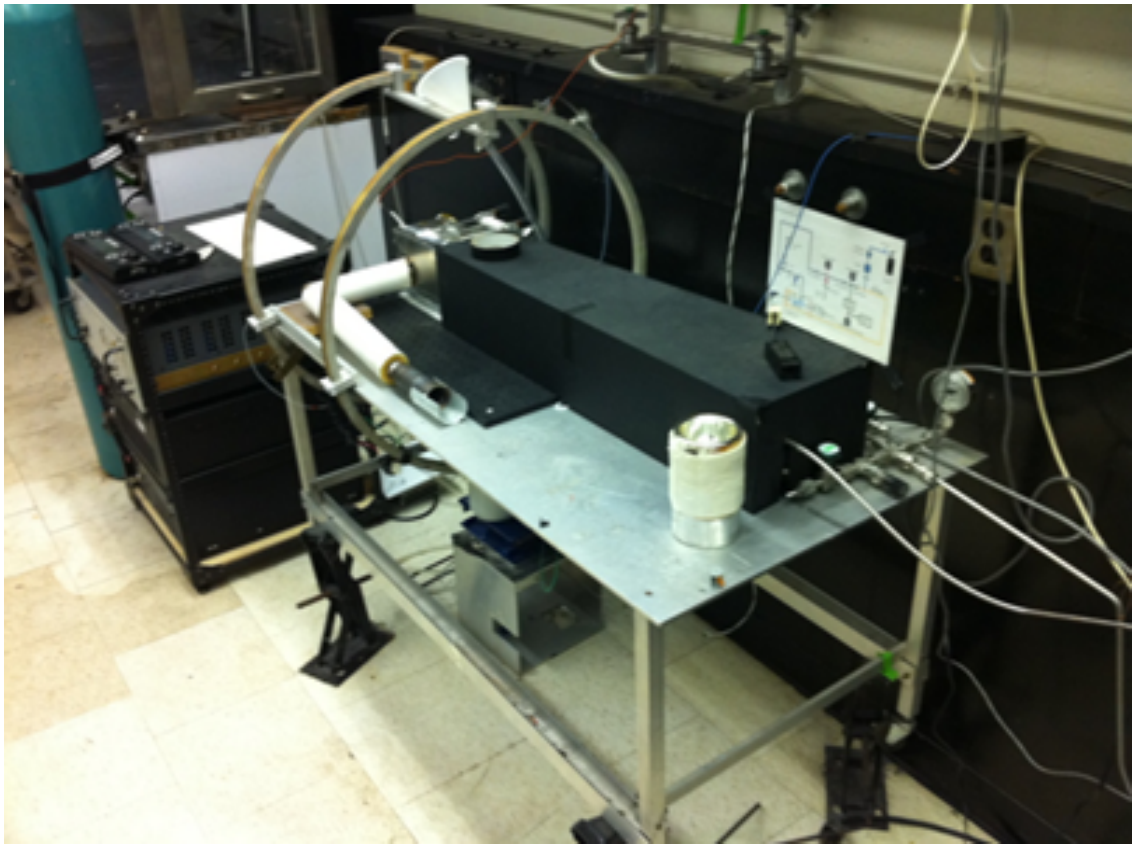

Figure A.2: Picture of home-built ^{129}Xe hyperpolarizer

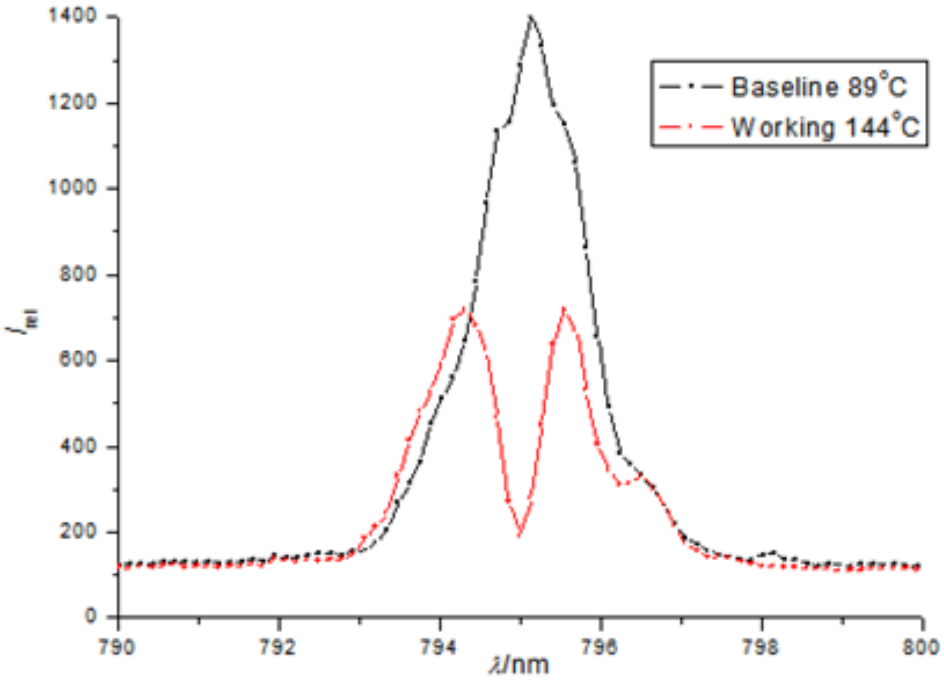

Figure A.3: Pump laser absorption profile by Rb vapor

Appendix B

Pulse Sequences and Source Code

B.1 Hyper-CEST NMR Pulse Sequence

```
;zgps_hyper_cest
;UNIVERSAL pulse sequence for Hyper-CEST
;
;
;1D sequence with presaturation (Hyper-CEST)
;using shaped pulse for presaturation
;use shaped pulse to saturate a different freq than f1
;then turn back to observe f1 with a hard pulse
;$CLASS=HighRes
;$DIM=1D
;$TYPE=
;$SUBTYPE=
;$COMMENT=


#include <Avance.incl>

"d12=20u"

"acqt0=-p1*2/3.1416"

1 ze
2 d1
  d12 fq=cnst20:f1
3 (p18:sp6 ph29):f1
  d6
  lo to 3 times l6
  d12 pl1:f1 fq=0:f1
  p1 ph1
  go=2 ph31
  30m mc #0 to 2 F0(zd)
exit

ph1=0 2 2 0 1 3 3 1
ph29=0
ph31=0 2 2 0 1 3 3 1

;pl1 : f1 channel - power level for pulse (default)
;sp6: f1 channel - shaped pulse for presaturation
;p1 : f1 channel -  90 degree high power pulse
;p18: f1 channel - presaturation using shaped pulse
;d12: delay for power switching                    [20 usec]
;l6: p18 * l6 = total duration of presaturation
;NS: 1 * n, total number of scans: NS * TD0

;use 100msec pulse of square shape defined by 1000 points
```

B.2 1D EXSY NMR Pulse Sequence

```
;xe nmr excitation-recovery
;measure xe exchage rates in cryptophanes
;avance-version (06/12/11)
;
;pseudo 2D
;using different acquisition time to define different mixing times
;using different memory-blocks for initial and recovery spectra

;
;$CLASS=HighRes
;$DIM=2D
;$TYPE=
;$SUBTYPE=
;$COMMENT=
;

;use the au program "yb-exch-time" to acquire while change the TD,
;therefore changing AQ
;use "yb-compare2" to record the data (ratio between integrals)
;use wider excitation region than 100 Hz (Applied to TAAC)
;

#include <Avance.incl>
#include <Delay.incl>


"d11=30m"
"DELTA1=d1-d20"


1 ze
2 3m st0
 d1

 4u pl0:f1
 (p11:sp1 ph1):f1
 goscnp ph31

 20u st
 4u pl0:f1
 (p11:sp1 ph1):f1
 goscnp ph31

 d11 wr #0
 3m ipp1 ipp31
 lo to 2 times ns
exit
```

```
ph1=0 0 2 0 1 3 3 1
ph31=0 0 2 0 1 3 3 1

;
;f1  : channel - power level for xenon excitation
;p1 : f1 channel -  90 degree high power pulse
;d1 : relaxation delay; 1-5 * T1
;d11: delay for disk I/O                              [30 msec]
;l4: l4 = number of averages = (total number of scans) / NS
;NS: 8 * n
;DS: 4
;td1: number of experiments
;NBL: NBL = number of irradiation frequencies
; choose td in f1 to be 2
;

;this pulse program produces a ser-file (PARMOD = 2D)
```

Appendix C

Experiment Control Programs

C.1 Hyper-CEST Profile at Different Saturation Frequencies

```
// AU program "yb-cest-profile"
// for Hyper-CEST profile scan
// use sw_ppm as the saturation frequency in ppm
// this AU program is used with pulse sequence "zgps_hyper_cest"

#include <stdlib.h>

char *envpnt;
int expTime, zgsafety, sleeptime = 20;
float sw_ppm_start = -50.0, sw_stepsize = 10.0,
    sw_hz = 0.0, sw_ppm_end = 50.0, sw_ppm = 0.0;
GETFLOAT("Choose the starting chemical shift
    (relative to the solvent peak):", sw_ppm_start);
GETFLOAT("Choose the ending chemical shift
    (relative to the solvent peak):", sw_ppm_end);
GETFLOAT("Choose the chemical shift scan
    stepwidth:", sw_stepsize);

/* Turn zg safety off if on. Turn it back on at the end. */
envpnt = getenv("UXNMR_SAFETY");
zgsafety = 0;
if(envpnt != NULL)
{
 if(strcasecmp(envpnt, "on") == 0)
 {
   zgsafety = 1;
   CPR_exec("env set UXNMR_SAFETY=off", WAIT_TERM);
 }
}
/* end of zg safety */

// calculate number of exp based on freq span and step size of freq change
int NumberOfExp=(sw_ppm_end - sw_ppm)/sw_stepsize + 1;

// write parameters into a temporary par set
GETCURDATA;
WPAR("temp_yb","all");


// three blank points to eliminate the starting bias of hp xenon flow
// go to the end of the dataset by changing expno
WRA(NumberOfExp + 1);
REXPNO(NumberOfExp + 1);
```

```
// acquire three blank points
TIMES(3)
    system("closeall.exe");
    sleep(sleeptime);
    SETCURDATA;
    RPAR("temp_yb","all");
    system("openall.exe");
    ZG;

  // auto process current data
  EFP;
  APK;
  XCMD("abs n");
  APK;
  XCMD("abs n");
  APK;
  XCMD("abs n");

  // go to next data set
    IEXPNO;
END

// go back to front of dataset
REXPNO(1);

// start acquistion of useful exp data
sw_ppm = sw_ppm_start;
TIMES(NumberOfExp)
   system("closeall.exe");
   sleep(sleeptime);
   SETCURDATA
   RPAR("temp_yb","all");

   // convert ppm to Hz
   sw_hz = sw_ppm * 138.24;
   STOREPAR("CNST 20", sw_hz);

   // increase the current scan freq
   sw_ppm += sw_stepsize;

   system("openall.exe");
   ZG;

  // auto process current data
  EFP;
  APK;
  XCMD("abs n");
  APK;
  XCMD("abs n");
  APK;
  XCMD("abs n");
```

```
  // go to next data set
   IEXPNO;
END

/* Turn zg safety on. */
if(zgsafety == 1)
 CPR_exec("env set UXNMR_SAFETY=on", WAIT_TERM);

QUITMSG("--- yb-cest-profile finished ---");
```

C.2 Hyper-CEST Depolarization Rate Contrast

```
// AU program "cest-profile"
// for Hyper-CEST profile scan
// use sw_ppm as the saturation frequency in ppm
// this AU program is used with pulse sequence "zgps_hyper_cest"

#include <stdlib.h>

char *envpnt;
int expTime, zgsafety, sleeptime = 20;
int loop_start = 0, loop_stepsize = 200, loop_current=0, loop_end=2000;
GETINT("Choose the starting number of saturation loops:", loop_start);
GETINT("Choose the ending number of saturation loops::", loop_end);
GETINT("Choose the loop incremental stepwidth:", loop_stepsize);

/* Turn zg safety off if on. Turn it back on at the end. */
envpnt = getenv("UXNMR_SAFETY");
zgsafety = 0;
if(envpnt != NULL)
{
 if(strcasecmp(envpnt, "on") == 0)
 {
   zgsafety = 1;
   CPR_exec("env set UXNMR_SAFETY=off", WAIT_TERM);
 }
}

GETCURDATA;
WPAR("temp_yb","all");

// three blank points to eliminate the starting bias of hp xenon flow
TIMES(3)
    system("closeall.exe");
    sleep(sleeptime);
    SETCURDATA;
```

```
    RPAR("temp_yb","all");
  STOREPAR("L 6 ", 0);
    system("openall.exe");
    ZG;

  // auto process current data
  EFP;
  APK;
  XCMD("abs n");
  APK;
  XCMD("abs n");
  APK;
  XCMD("abs n");

  // go to next data set

    IEXPNO;
END

// calculate number of exp based on loop span
// and step size of loop increment
int NumberOfExp=(loop_end - loop_start)/loop_stepsize + 1;
loop_current = loop_start - loop_stepsize;

TIMES(NumberOfExp)
   system("closeall.exe");
   sleep(sleeptime);
   SETCURDATA
   RPAR("temp_yb","all");

   // change number of saturation loops
   loop_current += loop_stepsize;
   STOREPAR("L 6 ", loop_current);
   system("openall.exe");
   ZG;

  // auto process current data
  EFP;
  APK;
  XCMD("abs n");
  APK;
  XCMD("abs n");
  APK;
  XCMD("abs n");

  // go to next data set
   IEXPNO;
END

/* Turn zg safety on. */
if(zgsafety == 1)
```

```
 CPR_exec("env set UXNMR_SAFETY=on", WAIT_TERM);

QUITMSG("--- yb-cest-loop finished ---");
```

C.3 Hyper-CEST Data Auto-processing Script

```
/*****************************************************************/
/*  yb-multi-int-cest   11/1/2012     */
/*****************************************************************/
/*  Short Description :         */
/*  AU program for automatic integration of a series  */
/*  of 1D spectra with AI calibration.      */
/*****************************************************************/
/*  Keywords :            */
/*  integration of a series of data sets      */
/*****************************************************************/
/*  Description/Usage :         */
/*  AU program for automatic integration of a series  */
/*  of 1D spectra with AI calibration. The spectra can  */
/*  either be stored in a series of EXPNOs or in a series */
/*  of PROCNOs.           */
/*  The AU program works as follows :     */
/*  1. Switch to the first experiment to be integrated.   */
/*  2. Define the integral region(s) you want to use  */
/*     in the interactive integration menu. Calibrate the */
/*     integrals with an appropriate calibration factor */
/*     (calibrate button) and store the intrng file (write  */
/*     return button).          */
/*  3. Store the intrng file with the 'wmisc' command */
/*     under a name of your choice.       */
/*  4. Start the AU program.        */
/*  The individual integration results are stored in the  */
/*  file integrals.txt in each dataset, the summary of  */
/*  all results is stored in the file intall.txt in the */
/*  first dataset.            */


char intrngfile[256], printname[256];
char intresult[256], intallresult[256], dummystr[256];
/* intallresult is the final output */
int iii, useprocnos=0, curr_loop = 0;
float curr_freq = 0;
FILE *fpnt, *fpnt2;

int integ_number = 0;
float start_ppm = 0, end_ppm = 0, integ_value = 0;
```

```
GETCURDATA

i1 = 4;
GETINT ("Enter first experiment number :",i1)
DATASET(name,i1,procno,disk,user)
i2 = 23;
GETINT ("Enter number of experiments :",i2)

/* Name of integration range, to be applied to all spectra */
(void) strcpy (intrngfile,"cest");
GETSTRING ("Enter name of intrng file :",intrngfile)

RMISC("intrng",intrngfile)
STOREPAR("INTSCL",1.0)
FETCHPAR("CURPRIN",printname)
STOREPAR("CURPRIN","integrals.txt")
LI
STOREPAR("CURPRIN",printname)

(void) sprintf (intresult,"%s/data/%s/%s/%s/%d/pdata/%d/integrals.txt",
    disk, user, type, name, expno, procno);
fpnt=fopen(intresult, "r");
if(fpnt==NULL)
{
  Proc_err(DEF_ERR_OPT, "No integral result file :\n%s\n\
Maybe CURPRIN is not a filename ?", intresult);
  ABORT
}
(void) sprintf (intallresult,"%s/data/%s/%s/%s/%s.txt",
      disk, user, type, name, name);
fpnt2=fopen(intallresult, "wt");
if(fpnt2==NULL)
{
  Proc_err(DEF_ERR_OPT, "No all-integral result file :\n%s",
               intallresult);
  ABORT
}
/* Discard first five lines of integral result file */

for (iii = 0; iii < 5; iii++)
  fgets(dummystr, 120, fpnt);

/*generate top of table */
  (void) sprintf (dummystr,"Chemical shift , CNST20(Hz) , L6 , Expno
    , Integral of Xe(aq) peak\n", curr_freq );
  fputs (dummystr, fpnt2);

  // get saturation frequency in each file (in ppm )
  FETCHPAR("CNST 20", &curr_freq)
  (void) sprintf (dummystr,"%.2f , ", curr_freq / 138.24 );
  fputs (dummystr, fpnt2);
```

```
  // get saturation frequency in each file (in Hz )
  FETCHPAR("CNST 20", &curr_freq)
  (void) sprintf (dummystr,"%.2f , ", curr_freq );
  fputs (dummystr, fpnt2);

  // get number of cest loops in each file
  FETCHPAR("L 6",&curr_loop)
  (void) sprintf (dummystr,"%d , ",curr_loop);
  fputs (dummystr, fpnt2);

  (void) sprintf (dummystr,"%d , ",expno);
  fputs (dummystr, fpnt2);
/*
while (fgets(dummystr, 120, fpnt) != NULL)
  fputs (dummystr, fpnt2);
*/
  fscanf(fpnt, "%d\t%f\t%f\t%f\t\n", &integ_number,
    &start_ppm, &end_ppm, &integ_value);
  fprintf(fpnt2, "%f\n", integ_value);
fclose (fpnt);

TIMES(i2-1)
    IEXPNO

  RMISC("intrng",intrngfile)
  STOREPAR("INTSCL",-1.0)
  FETCHPAR("CURPRIN",printname)
  STOREPAR("CURPRIN","integrals.txt")
  LI
  STOREPAR("CURPRIN",printname)
  (void) sprintf(intresult,
    "%s/data/%s/%s/%s/%d/pdata/%d/integrals.txt",
    disk, user, type, name, expno, procno);
  fpnt=fopen(intresult, "r");
  if(fpnt==NULL)
  {
    Proc_err(DEF_ERR_OPT, "No integral result file :\n%s", intresult);
    return(-1);
  }
  /* Discard first five lines of integral result file */
  for (iii = 0; iii < 5; iii++)
    fgets(dummystr, 120, fpnt);

  // get saturation frequency in each file (in ppm )
  FETCHPAR("CNST 20", &curr_freq)
  (void) sprintf (dummystr,"%.2f , ", curr_freq / 138.24 );
  fputs (dummystr, fpnt2);

  // get saturation frequency in each file (in Hz)
  FETCHPAR("CNST 20", &curr_freq)
```

```
  (void) sprintf (dummystr,"%5.2f , ", curr_freq );
  fputs (dummystr, fpnt2);

  // get number of cest loops in each file
  FETCHPAR("L 6",&curr_loop)
  (void) sprintf (dummystr,"%d , ",curr_loop);
  fputs (dummystr, fpnt2);

  (void) sprintf (dummystr,"%d , ",expno);
  fputs (dummystr, fpnt2);
/*
  while (fgets(dummystr, 120, fpnt) != NULL)
    fputs (dummystr, fpnt2);
*/
  fscanf(fpnt, "%d\t%f\t%f\t%f\t\n", &integ_number,
  &start_ppm, &end_ppm, &integ_value);
  fprintf(fpnt2, "%f\n", integ_value);

  fclose (fpnt);
END

fclose (fpnt2);

(void) sprintf (text,"--- yb-multi-int-cest finished ---\n\
All results summarized in :\n%s",intallresult);
QUITMSG (text)
```

Bibliography

[1] R. Weissleder and U. Mahmood, "Molecular imaging," *Radiology*, vol. 219, no. 2, pp. 316–333, 2001.

[2] R. Weissleder, "Molecular imaging in cancer," *Science*, vol. 312, pp. 1168–1171, 2006.

[3] T. F. Massoud and S. S. Gambhir, "Molecular imaging in living subjects: seeing fundamental biological processes in a new light," *Genes and Development*, vol. 17, pp. 545–580, 2003.

[4] E. L. Que, D. W. Domaille, and C. J. Chang, "Metals in neurobiology: Probing their chemistry and biology with molecular imaging," *Chemical Reviews*, vol. 108, pp. 1517–1549, 2008.

[5] M. M. Modo, J. W. W. Bulte, and Editors, *Molecular and Cellular MR Imaging*. CRC Press LLC, 2007.

[6] OECD, "Magnetic resonance imaging (mri) exams, total 2013," June 2009.

[7] E. Terreno, W. Dastru, D. D. Castelli, E. Gianolio, S. G. Crich, D. Longo, and S. Aime, "Advances in metal-based probes for mr molecular imaging applications," *Current Medicinal Chemistry*, vol. 17, no. 31, pp. 3684–3700, 2010.

[8] Wikipedia, "Mri contrast agent — wikipedia, the free encyclopedia," 2013. [Online; accessed 26-November-2013].

[9] E. Terreno, D. D. Castelli, A. Viale, and S. Aime, "Challenges for molecular magnetic resonance imaging," *Chemical Reviews*, vol. 110, no. 5, pp. 3019–3042, 2010.

[10] E. Terreno, D. D. Castelli, A. Viale, and S. Aime, "Challenges for molecular magnetic resonance imaging," *Chemical Reviews*, vol. 110, no. 5, pp. 3019–3042, 2010.

[11] G.-L. Davies, I. Kramberger, and J. J. Davis, "Environmentally responsive mri contrast agents," *Chemical Communications*, vol. 49, pp. 9704–9721, 2013.

[12] O. Taratula and I. J. Dmochowski, "Functionalized xe-129 contrast agents for magnetic resonance imaging," *Current Opinion in Chemical Biology*, vol. 14, no. 1, pp. 97–104, 2010.

[13] I. Hancu, W. T. Dixon, M. Woods, E. Vinogradov, A. D. Sherry, and R. E. Lenkinski, "Cest and paracest mr contrast agents," *Acta Radiologica*, vol. 51, no. 8, pp. 910–923, 2010.

[14] A. D. Sherry and M. Woods, "Chemical exchange saturation transfer contrast agents for magnetic resonance imaging," *Annual Review of Biomedical Engineering*, vol. 10, no. 1, pp. 391–411, 2008.

[15] Wikipedia, "Gyromagnetic ratio — Wikipedia, the free encyclopedia," 2013. [Online; accessed 22-November-2013].

[16] D. Raftery, "Xenon nmr spectroscopy," in *Annual Reports on NMR Spectroscopy, Vol 57*, vol. 57 of *Annual Reports on NMR Spectroscopy*, pp. 205–270, San Diego: Elsevier Academic Press Inc, 2006.

[17] C. Ratcliffe, "Xenon nmr spectroscopy," vol. 36 of *Annual Reports on NMR Spectroscopy*, pp. 123–221, Elsevier Academic Press Inc, 1998.

[18] K. F. Stupic, J. S. Six, M. D. Olsen, G. E. Pavlovskaya, and T. Meersmann, "Combustion resistance of the xe-129 hyperpolarized nuclear spin state," *Physical Chemistry Chemical Physics*, vol. 15, no. 1, pp. 94–97, 2013.

[19] B. Driehuys, S. Martinez-Jimenez, Z. I. Cleveland, G. M. Metz, D. M. Beaver, J. C. Nouls, S. S. Kaushik, R. Firszt, C. Willis, K. T. Kelly, J. Wolber, M. Kraft, and H. P. McAdams, "Chronic obstructive pulmonary disease: Safety and tolerability of hyperpolarized 129xe mr imaging in healthy volunteers and patients," *Radiology*, vol. 262, no. 1, pp. 279–289, 2012.

[20] X. Zhou, Y. P. Sun, M. Mazzanti, N. Henninger, J. Mansour, M. Fisher, and M. Albert, "Mri of stroke using hyperpolarized xe-129," *NMR in Biomedicine*, vol. 24, no. 2, pp. 170–175, 2011.

[21] Q. Wei, G. K. Seward, P. A. Hill, B. Patton, I. E. Dimitrov, N. N. Kuzma, and I. J. Dmochowski, "Designing 129xe nmr biosensors for matrix metalloproteinase detection," *Journal of the American Chemical Society*, vol. 128, no. 40, pp. 13274–13283, 2006.

[22] J. M. Chambers, P. A. Hill, J. A. Aaron, Z. Han, D. W. Christianson, N. N. Kuzma, and I. J. Dmochowski, "Cryptophane xenon-129 nuclear magnetic resonance biosensors targeting human carbonic anhydrase," *Journal of the American Chemical Society*, vol. 131, no. 2, pp. 563–569, 2009.

[23] P. A. Hill, Q. Wei, R. G. Eckenhoff, and I. J. Dmochowski, "Thermodynamics of xenon binding to cryptophane in water and human plasma," *Journal of the American Chemical Society*, vol. 129, no. 30, pp. 9262–9263, 2007.

[24] P. A. Hill, Q. Wei, T. Troxler, and I. J. Dmochowski, "Substituent effects on xenon binding affinity and solution behavior of water-soluble cryptophanes,"

Journal of the American Chemical Society, vol. 131, no. 8, pp. 3069–3077, 2009.

[25] G. K. Seward, Q. Wei, and I. J. Dmochowski, "Peptide-mediated cellular uptake of cryptophane," *Bioconjugate Chemistry*, vol. 19, no. 11, pp. 2129–35, 2008.

[26] G. K. Seward, Y. Bai, N. S. Khan, and I. J. Dmochowski, "Cell-compatible, integrin-targeted cryptophane-129xe nmr biosensors," *Chemical Science*, vol. 2, no. 6, pp. 1103–1110, 2011.

[27] M. M. Spence, S. M. Rubin, I. E. Dimitrov, E. J. Ruiz, D. E. Wemmer, A. Pines, S. Q. Yao, F. Tian, and P. G. Schultz, "Functionalized xenon as a biosensor," *Proceedings of the National Academy of Sciences of the United States of America*, vol. 98, no. 19, pp. 10654–10657, 2001.

[28] M. M. Spence, E. J. Ruiz, S. M. Rubin, T. J. Lowery, N. Winssinger, P. G. Schultz, D. E. Wemmer, and A. Pines, "Development of a functionalized xenon biosensor," *Journal of the American Chemical Society*, vol. 126, no. 46, pp. 15287–15294, 2004.

[29] C. Boutin, A. Stopin, F. Lenda, T. Brotin, J.-P. Dutasta, N. Jamin, A. Sanson, Y. Boulard, F. Leteurtre, G. Huber, A. Bogaert-Buchmann, N. Tassali, H. Desvaux, M. Carrire, and P. Berthault, "Cell uptake of a biosensor detected by hyperpolarized 129xe nmr: The transferrin case," *Bioorganic and Medicinal Chemistry*, vol. 19, no. 13, pp. 4135–4143, 2011.

[30] T. Meldrum, K. L. Seim, V. S. Bajaj, K. K. Palaniappan, W. Wu, M. B. Francis, D. E. Wemmer, and A. Pines, "A xenon-based molecular sensor assembled on an ms2 viral capsid scaffold," *Journal of the American Chemical Society*, vol. 132, no. 17, pp. 5936–5937, 2010.

[31] P. Berthault, H. Desvaux, T. Wendlinger, M. Gyejacquot, A. Stopin, T. Brotin, J.-P. Dutasta, and Y. Boulard, "Effect of ph and counterions on the encapsulation properties of xenon in water-soluble cryptophanes," *Chemistry - A European Journal*, vol. 16, no. 43, pp. 12941–12946, 2010.

[32] N. Kotera, N. Tassali, E. Lonce, C. Boutin, P. Berthault, T. Brotin, J.-P. Dutasta, L. Delacour, T. Traor, D.-A. Buisson, F. Taran, S. Coudert, and B. Rousseau, "A sensitive zinc-activated 129xe mri probe," *Angewandte Chemie International Edition*, vol. 124, no. 17, pp. 4176–4179, 2012.

[33] M. Schnurr, C. Witte, and L. Schroeder, "Functionalized 129xe as a potential biosensor for membrane fluidity," *Physical Chemistry Chemical Physics*, vol. 15, pp. 14178–14181, 2013.

[34] K. K. Palaniappan, R. M. Ramirez, V. S. Bajaj, D. E. Wemmer, A. Pines, and M. B. Francis, "Molecular imaging of cancer cells using a bacteriophage-based 129xe nmr biosensor," *Angewandte Chemie International Edition*, p. in press, 2013.

[35] S. Aime, C. Cabella, S. G. Crich, and V. Mainero, "New agents for magnetic imaging method, ep1369134a1," 2003.

[36] A. Abragam and M. Goldman, "Principles of dynamic nuclear polarisation," *Reports on Progress in Physics*, vol. 41, no. 3, p. 395, 1978.

[37] T. G. Walker and W. Happer, "Spin-exchange optical pumping of noble-gas nuclei," *Reviews of Modern Physics*, vol. 69, no. 2, p. 629, 1997.

[38] C. R. Bowers and D. P. Weitekamp, "Transformation of symmetrization order to nuclear-spin magnetization by chemical reaction and nuclear magnetic resonance," *Physical Review Letters*, vol. 57, no. 21, pp. 2645–2648, 1986.

[39] M. A. Bouchiat, T. R. Carver, and C. M. Varnum, "Nuclear polarization in he3 gas induced by optical pumping and dipolar exchange," *Physical Review Letters*, vol. 5, p. 373, 1960.

[40] W. Happer, E. Miron, S. Schaefer, D. Schreiber, W. A. van Wijngaarden, and X. Zeng, "Polarization of the nuclear spins of noble-gas atoms by spin exchange with optically pumped alkali-metal atoms," *Physical Review A*, vol. 29, no. 6, p. 3092, 1984.

[41] G. D. Cates, D. R. Benton, M. Gatzke, W. Happer, K. C. Hasson, and N. R. Newbury, "Laser production of large nuclear-spin polarization in frozen xenon," *Physical Review Letters*, vol. 65, no. 20, p. 2591, 1990.

[42] B. Driehuys, G. D. Cates, E. Miron, K. Sauer, D. K. Walter, and W. Happer, "High-volume production of laser-polarized [sup 129]xe," *Applied Physics Letters*, vol. 69, no. 12, pp. 1668–1670, 1996.

[43] M. Gatzke, G. D. Cates, B. Driehuys, D. Fox, W. Happer, and B. Saam, "Extraordinarily slow nuclear spin relaxation in frozen laser-polarized ^{129}Xe," *Physical Review Letters*, vol. 70, pp. 690–693, Feb 1993.

[44] K. M. Ward, A. H. Aletras, and R. S. Balaban, "A new class of contrast agents for mri based on proton chemical exchange dependent saturation transfer (cest)," *Journal of Magnetic Resonance*, vol. 143, no. 1, pp. 79–87, 2000.

[45] N. Goffeney, J. W. Bulte, J. Duyn, J. Bryant, L. H., and P. C. van Zijl, "Sensitive nmr detection of cationic-polymer-based gene delivery systems using saturation transfer via proton exchange," *Journal of the American Chemical Society*, vol. 123, no. 35, pp. 8628–9, 2001.

[46] H. M. McConnell, "Reaction rates by nuclear magnetic resonance," *The Journal of Chemical Physics*, vol. 28, no. 3, 1958.

[47] T. Meldrum, V. S. Bajaj, D. E. Wemmer, and A. Pines, "Band-selective chemical exchange saturation transfer imaging with hyperpolarized xenon-based molecular sensors," *Journal of Magnetic Resonance*, vol. 213, pp. 14–21, 2011.

[48] R. F. Tilton and I. D. Kuntz, "Nuclear magnetic resonance studies of xenon-129 with myoglobin and hemoglobin," *Biochemistry*, vol. 21, no. 26, pp. 6850–6857, 1982.

[49] S. M. Rubin, M. M. Spence, I. E. Dimitrov, E. J. Ruiz, A. Pines, and D. E. Wemmer, "Detection of a conformational change in maltose binding protein by 129xe nmr spectroscopy," *Journal of the American Chemical Society*, vol. 123, no. 35, pp. 8616–8617, 2001.

[50] S. M. Rubin, S. Y. Lee, E. J. Ruiz, A. Pines, and D. E. Wemmer, "Detection and characterization of xenon-binding sites in proteins by xe-129 nmr spectroscopy," *Journal of Molecular Biology*, vol. 322, no. 2, pp. 425–440, 2002.

[51] C. R. Bowers, V. Storhaug, C. E. Webster, J. Bharatam, A. Cottone, R. Gianna, K. Betsey, and B. J. Gaffney, "Exploring surfaces and cavities in lipoxygenase and other proteins by hyperpolarized xenon-129 nmr," *Journal of the American Chemical Society*, vol. 121, no. 40, pp. 9370–9377, 1999.

[52] K. Bartik, M. Luhmer, S. J. Heyes, R. Ottinger, and J. Reisse, "Probing molecular cavities in -cyclodextrin solutions by xenon {NMR}," *Journal of Magnetic Resonance, Series B*, vol. 109, no. 2, pp. 164 – 168, 1995.

[53] J. Lagona, P. Mukhopadhyay, S. Chakrabarti, and L. Isaacs, "The cucurbit[¡i¿n¡/i¿]uril family," *Angewandte Chemie International Edition*, vol. 44, no. 31, pp. 4844–4870, 2005.

[54] T. A. Robbins, C. B. Knobler, D. R. Bellew, and D. J. Cram, "Host-guest complexation. 67. a highly adaptive and strongly binding hemicarcerand," *Journal of the American Chemical Society*, vol. 116, no. 1, pp. 111–122, 1994.

[55] T. Brotin and J.-P. Dutasta, "Cryptophanes and their complexes-present and future," *Chemical Reviews*, vol. 109, no. 1, pp. 88–130, 2009.

[56] D. R. Jacobson, N. S. Khan, R. Coll, R. Fitzgerald, L. Laureano-Prez, Y. Bai, and I. J. Dmochowski, "Measurement of radon and xenon binding to a cryptophane molecular host," *Proceedings of the National Academy of Sciences of the United States of America*, vol. 108, no. 27, p. 10969, 2011.

[57] O. Taratula, P. A. Hill, Y. B. Bai, N. S. Khan, and I. J. Dmochowski, "Shorter synthesis of trifunctionalized crytophane-a derivatives," *Organic Letters*, vol. 13, no. 6, pp. 1414–1417, 2011.

[58] H. C. Kolb, M. G. Finn, and K. B. Sharpless, "Click chemistry: Diverse chemical function from a few good reactions," *Angewandte Chemie International Edition*, vol. 40, no. 11, pp. 2004–2021, 2001.

[59] C. T. Supuran and A. Scozzafava, "Carbonic anhydrases as targets for medicinal chemistry," *Bioorganic and Medicinal Chemistry*, vol. 15, no. 13, pp. 4336–4350, 2007.

[60] K. Nordfors, J. Haapasalo, M. Korja, A. Niemela, J. Laine, A. K. Parkkila, S. Pastorekova, J. Pastorek, A. Waheed, W. S. Sly, S. Parkkila, and H. Haapasalo, "The tumour-associated carbonic anhydrases ca ii, ca ix and ca xii in a group of medulloblastomas and supratentorial primitive neuroectodermal tumours: an association of ca ix with poor prognosis," *BMC Cancer*, vol. 10, p. 148, 2010.

[61] S. Kaneta, S. Ishizuki, M. Kasahara, S. Nagao, and H. Takahashi, "Renal carbonic anhydrase activity in dba/2fg-pcy/pcy mice with inherited polycystic kidney disease," *Experimental Animals*, vol. 48, no. 3, pp. 161–9, 1999.

[62] J. A. Loncaster, A. L. Harris, S. E. Davidson, J. P. Logue, R. D. Hunter, C. C. Wycoff, J. Pastorek, P. J. Ratcliffe, I. J. Stratford, and C. M. L. West, "Carbonic anhydrase (ca ix) expression, a potential new intrinsic marker of hypoxia: Correlations with tumor oxygen measurements and prognosis in locally advanced carcinoma of the cervix," *Cancer Research*, vol. 61, no. 17, pp. 6394–6399, 2001.

[63] O. Tureci, U. Sahin, E. Vollmar, S. Siemer, E. Gottert, G. Seitz, A. K. Parkkila, G. N. Shah, J. H. Grubb, M. Pfreundschuh, and W. S. Sly, "Human carbonic anhydrase xii: cdna cloning, expression, and chromosomal localization of a carbonic anhydrase gene that is overexpressed in some renal cell cancers," *Proceedings of the National Academy of Sciences of the United States of America*, vol. 95, no. 13, pp. 7608–13, 1998.

[64] V. M. Krishnamurthy, G. K. Kaufman, A. R. Urbach, I. Gitlin, K. L. Gudiksen, D. B. Weibel, and G. M. Whitesides, "Carbonic anhydrase as a model for biophysical and physical-organic studies of proteins and protein-ligand binding," *Chemical Reviews*, vol. 108, no. 3, pp. 946–1051, 2008.

[65] J. Greer, J. W. Erickson, J. J. Baldwin, and M. D. Varney, "Application of the three-dimensional structures of protein target molecules in structure-based drug design," *Journal of Medicinal Chemistry*, vol. 37, no. 8, pp. 1035–54, 1994.

[66] C. T. Supuran, "Carbonic anhydrases: novel therapeutic applications for inhibitors and activators," *Nature Reviews. Drug Discovery*, vol. 7, no. 2, pp. 168–181, 2008.

[67] J. A. Aaron, J. M. Chambers, K. M. Jude, L. Di Costanzo, I. J. Dmochowski, and D. W. Christianson, "Structure of a xe-129-cryptophane biosensor complexed with human carbonic anhydrase ii," *Journal of the American Chemical Society*, vol. 130, no. 22, pp. 6942–+, 2008.

[68] O. Taratula, M. P. Kim, Y. B. Bai, J. P. Philbin, B. A. Riggle, D. N. Haase, and I. J. Dmochowski, "Synthesis of enantiopure, trisubstituted cryptophane-a derivatives," *Organic Letters*, vol. 14, no. 14, pp. 3580–3583, 2012.

[69] E. J. Ruiz, D. N. Sears, A. Pines, and C. J. Jameson, "Diastereomeric xe chemical shifts in tethered cryptophane cages," *Journal of the American Chemical Society*, vol. 128, no. 51, pp. 16980–16988, 2006.

[70] T. J. Lowery, S. Garcia, L. Chavez, E. J. Ruiz, T. Wu, T. Brotin, J.-P. Dutasta, D. S. King, P. G. Schultz, A. Pines, and D. E. Wemmer, "Optimization of xenon biosensors for detection of protein interactions," *ChemBioChem*, vol. 7, no. 1, pp. 65–73, 2006.

[71] A. Schlundt, W. Kilian, M. Beyermann, J. Sticht, S. Gunther, S. Hopner, K. Falk, O. Roetzschke, L. Mitschang, and C. Freund, "A xenon-129 biosensor for monitoring mhc-peptide interactions," *Angewandte Chemie International Edition*, vol. 48, no. 23, pp. 4142–4145, 2009.

[72] R. J. Gillies, N. Raghunand, M. L. Garcia-Martin, and R. A. Gatenby, "Ph imaging," *IEEE Engineering in Medicine and Biology Magazine*, vol. 23, no. 5, pp. 57–64, 2004.

[73] S. J. Reshkin, R. A. Cardone, and V. Casavola, "The role of disturbed ph dynamics and the na+/h+ exchanger in metastasis," *Nature Reviews Cancer*, vol. 5, no. 10, pp. 786–795, 2005.

[74] M. P. Lowe, D. Parker, O. Reany, S. Aime, M. Botta, G. Castellano, E. Gianolio, and R. Pagliarin, "ph-dependent modulation of relaxivity and lumines-

cence in macrocyclic gadolinium and europium complexes based on reversible intramolecular sulfonamide ligation," *Journal of the American Chemical Society*, vol. 123, no. 31, pp. 7601–7609, 2001.

[75] K. E. Lokling, S. L. Fossheim, R. Skurtveit, A. Bjornerud, and J. Klaveness, "ph-sensitive paramagnetic liposomes as mri contrast agents: in vitro feasibility studies," *Magnetic Resonance Imaging*, vol. 19, no. 5, pp. 731–738, 2001.

[76] K. E. Lokling, R. Skurtveit, S. L. Fossheim, G. Smistad, I. Henriksen, and J. Klaveness, "ph-sensitive paramagnetic liposomes for mri: assessment of stability in blood," *Magnetic Resonance Imaging*, vol. 21, no. 5, pp. 531–540, 2003.

[77] S. R. Zhang, P. Winter, K. C. Wu, and A. D. Sherry, "A novel europium(iii)-based mri contrast agent," *Journal of the American Chemical Society*, vol. 123, no. 7, pp. 1517–1518, 2001.

[78] S. Aime, A. Barge, D. D. Castelli, F. Fedeli, A. Mortillaro, F. U. Nielsen, and E. Terreno, "Paramagnetic lanthanide(iii) complexes as ph-sensitive chemical exchange saturation transfer (cest) contrast agents for mri applications," *Magnetic Resonance in Medicine*, vol. 47, no. 4, pp. 639–648, 2002.

[79] N. K. Subbarao, R. A. Parente, F. C. Szoka, L. Nadasdi, and K. Pongracz, "Ph-dependent bilayer destabilization by an amphipathic peptide," *Biochemistry*, vol. 26, no. 11, pp. 2964–2972, 1987.

[80] W. J. Li, F. Nicol, and F. C. Szoka, "Gala: a designed synthetic ph-responsive amphipathic peptide with applications in drug and gene delivery," *Advanced Drug Delivery Reviews*, vol. 56, no. 7, pp. 967–985, 2004.

[81] A. Viale and S. Aime, "Current concepts on hyperpolarized molecules in mri," *Current Opinion in Chemical Biology*, vol. 14, no. 1, pp. 90–96, 2010.

[82] S. Viswanathan, Z. Kovacs, K. N. Green, S. J. Ratnakar, and A. D. Sherry, "Alternatives to gadolinium-based metal chelates for magnetic resonance imaging," *Chemical Reviews*, vol. 110, no. 5, pp. 2960–3018, 2010.

[83] M. Woods, D. E. Woessner, and A. D. Sherry, "Paramagnetic lanthanide complexes as paracest agents for medical imaging," *Chemical Society Reviews*, vol. 35, no. 6, pp. 500–511, 2006.

[84] S. Aime, D. D. Castelli, and E. Terreno, "Highly sensitive mri chemical exchange saturation transfer agents using liposomes," *Angewandte Chemie International Edition*, vol. 44, no. 34, pp. 5513–5515, 2005.

[85] L. Schroder, T. J. Lowery, C. Hilty, D. E. Wemmer, and A. Pines, "Molecular imaging using a targeted magnetic resonance hyperpolarized biosensor," *Science*, vol. 314, no. 5798, pp. 446–449, 2006.

[86] K. Bartik, M. Luhmer, J.-P. Dutasta, A. Collet, and J. Reisse, "129xe and 1h nmr study of the reversible trapping of xenon by cryptophane-a in organic solution," *Journal of the American Chemical Society*, vol. 120, no. 4, pp. 784–791, 1998.

[87] H. A. Fogarty, P. Berthault, T. Brotin, G. Huber, H. Desvaux, and J.-P. Dutasta, "A cryptophane core optimized for xenon encapsulation," *Journal of the American Chemical Society*, vol. 129, no. 34, pp. 10332–10333, 2007.

[88] R. M. Fairchild, A. I. Joseph, K. T. Holman, H. A. Fogarty, T. Brotin, J. P. Dutasta, C. Boutin, G. Huber, and P. Berthault, "A water-soluble xe@cryptophane-111 complex exhibits very high thermodynamic stability and a peculiar xe-129 nmr chemical shift," *Journal of the American Chemical Society*, vol. 132, no. 44, pp. 15505–15507, 2010.

[89] T. Traore, G. Clave, L. Delacour, N. Kotera, P.-Y. Renard, A. Romieu, P. Berthault, C. Boutin, N. Tassali, and B. Rousseau, "The first metal-free

water-soluble cryptophane-111," *Chemical Communications*, vol. 47, p. 9702, 2011.

[90] J. L. Mynar, T. J. Lowery, D. E. Wemmer, A. Pines, and J. M. J. Frchet, "Xenon biosensor amplification via dendrimercage supramolecular constructs," *Journal of the American Chemical Society*, vol. 128, no. 19, pp. 6334–6335, 2006.

[91] V. Roy, T. Brotin, J.-P. Dutasta, M.-H. Charles, T. Delair, F. Mallet, G. Huber, H. Desvaux, Y. Boulard, and P. Berthault, "A cryptophane biosensor for the detection of specific nucleotide targets through xenon nmr spectroscopy," *ChemPhysChem*, vol. 8, no. 14, pp. 2082–2085, 2007.

[92] T. Meldrum, L. Schroder, P. Denger, D. E. Wemmer, and A. Pines, "Xenon-based molecular sensors in lipid suspensions," *Journal of Magnetic Resonance*, vol. 205, no. 2, pp. 242–246, 2010.

[93] A. L. Zook, B. B. Adhyaru, and C. R. Bowers, "High capacity production of >65% spin polarized xenon-129 for nmr spectroscopy and imaging," *Journal of Magnetic Resonance*, vol. 159, no. 2, pp. 175–182, 2002.

[94] T. Brotin, A. Lesage, L. Emsley, and A. Collet, "129xe nmr spectroscopy of deuterium-labeled cryptophane-a xenon complexes: Investigation of hostguest complexation dynamics," *Journal of the American Chemical Society*, vol. 122, no. 6, pp. 1171–1174, 2000.

[95] T. Brotin, T. Devic, A. Lesage, L. Emsley, and A. Collet, "Synthesis of deuterium-labeled cryptophane-a and investigation of xe@cryptophane complexation dynamics by 1d-exsy nmr experiments," *Chemistry - A European Journal*, vol. 7, no. 7, pp. 1561–1573, 2001.

[96] S. N. Aski, Z. Takacs, and J. Kowalewski, "Inclusion complexes of cryptophane-e with dichloromethane and chloroform: A thermodynamic and

kinetic study using the 1d-exsy nmr method," *Magnetic Resonance in Chemistry*, vol. 46, no. 12, pp. 1135–1140, 2008.

[97] H. L. Clever, *IUPAC Solubility Data Series, Vol. 2: Krypton, Xenon and Radon - Gas Solubilities*. Pergamon Press, 1979.

[98] O. Taratula, P. A. Hill, N. S. Khan, P. J. Carroll, and I. J. Dmochowski, "Crystallographic observation of 'induced fit' in a cryptophane host-guest model system," *Nature Communications*, vol. 1, no. 9, p. 148, 2010.

[99] L. Schroder, T. Meldrum, M. Smith, T. J. Lowery, D. E. Wemmer, and A. Pines, "Temperature response of xe-129 depolarization transfer and its application for ultrasensitive nmr detection," *Physical Review Letters*, vol. 100, no. 25, 2008.

[100] M. Kunth, J. Dopfert, C. Witte, F. Rossella, and L. Schroder, "Optimized use of reversible binding for fast and selective nmr localization of caged xenon," *Angewandte Chemie International Edition*, vol. 51, no. 33, pp. 8217–8220, 2012.

[101] D. H. Brouwer, S. Alavi, and J. A. Ripmeester, "A double quantum 129xe nmr experiment for probing xenon in multiply-occupied cavities of solid-state inclusion compounds," *Physical Chemistry Chemical Physics*, vol. 9, no. 9, pp. 1093–1098, 2007.

[102] M. Hanni, P. Lantto, and J. Vaara, "Nuclear spin relaxation due to chemical shift anisotropy of gas-phase 129xe," *Physical Chemistry Chemical Physics*, vol. 13, no. 30, pp. 13704–13708, 2011.

[103] J. A. N. F. Gomes and R. B. Mallion, "Aromaticity and ring currents," *Chemical Reviews*, vol. 101, no. 5, pp. 1349–1384, 2001.

[104] M. A. M. Forgeron, R. E. Wasylishen, and G. H. Penner, "Investigation of magnetic shielding in xenon difluoride using solid-state nmr spectroscopy and relativistic density functional theory," *The Journal of Physical Chemistry A*, vol. 108, no. 21, pp. 4751–4758, 2004.

[105] P. J. Piggot and D. W. Hilbert, "Sporulation of bacillus subtilis," *Current Opinion in Microbiology*, vol. 7, no. 6, pp. 579–86, 2004.

[106] P. Setlow, "Spores of bacillus subtilis: their resistance to and killing by radiation, heat and chemicals," *Journal of Applied Microbiology*, vol. 101, no. 3, pp. 514–525, 2006.

[107] M. Rupnik, M. H. Wilcox, and D. N. Gerding, "Clostridium difficile infection: new developments in epidemiology and pathogenesis," *Nature Reviews Microbiology*, vol. 7, no. 7, pp. 526–536, 2009.

[108] M. Mock and A. Fouet, "Anthrax," *Annual Review of Microbiology*, vol. 55, pp. 647–671, 2001.

[109] A. Driks, "The bacillus anthracis spore," *Molecular Aspects of Medicine*, vol. 30, pp. 368–373, 2009.

[110] P. T. McKenney, A. Driks, and P. Eichenberger, "The bacillus subtilis endospore: assembly and functions of the multilayered coat," *Nature Reviews Microbiology*, vol. 11, no. 1, pp. 33–44, 2013.

[111] B. A. Traag, A. Driks, P. Stragier, W. Bitter, G. Broussard, G. Hatfull, F. Chu, K. N. Adams, L. Ramakrishnan, and R. Losick, "Do mycobacteria produce endospores?," *Proceedings of the National Academy of Sciences of the United States of America*, vol. 107, no. 2, pp. 878–881, 2010.

[112] K. M. L. Taylor and W. Lin, "Hybrid silica nanoparticles for luminescent spore detection," *J. Mater. Chem.*, vol. 19, no. 35, pp. 6418–6422, 2009.

[113] H. Xu, X. Rao, J. Gao, J. Yu, Z. Wang, Z. Dou, Y. Cui, Y. Yang, B. Chen, and G. Qian, "A luminescent nanoscale metal-organic framework with controllable morphologies for spore detection," *Chemical Communications*, vol. 48, no. 59, pp. 7377–7379, 2012.

[114] M. L. Cable, J. P. Kirby, D. J. Levine, M. J. Manary, H. B. Gray, and A. Ponce, "Detection of bacterial spores with lanthanidemacrocycle binary complexes," *Journal of the American Chemical Society*, vol. 131, no. 27, pp. 9562–9570, 2009.

[115] I. Lee, W.-K. Oh, and J. Jang, "Screen-printed fluorescent sensors for rapid and sensitive anthrax biomarker detection," *Journal of Hazardous Materials*, vol. 252253, no. 0, pp. 186–191, 2013.

[116] W.-K. Oh, Y. S. Jeong, J. Song, and J. Jang, "Fluorescent europium-modified polymer nanoparticles for rapid and sensitive anthrax sensors," *Biosensors and Bioelectronics*, vol. 29, no. 1, pp. 172–177, 2011.

[117] S. Kaieda, B. Setlow, P. Setlow, and B. Halle, "Mobility of core water in bacillus subtilis spores by 2h nmr," *Biophysical Journal*, vol. 105, pp. 2016–2023, 2013.

[118] R. G. K. Leuschner and P. J. Lillford, "Investigation of bacterial spore structure by high resolution solid-state nuclear magnetic resonance spectroscopy and transmission electron microscopy," *International Journal of Food Microbiology*, vol. 63, pp. 35–50, 2001.

[119] E. P. Sunde, P. Setlow, L. Hederstedt, and B. Halle, "The physical state of water in bacterial spores," *Proceedings of the National Academy of Sciences of the United States of America*, vol. 106, no. 46, pp. 19334–19339, 2009.

[120] I. C. Ruset, S. Ketel, and F. W. Hersman, "Optical pumping system design for large production of hyperpolarized 129xe," *Physical Review Letters*, vol. 96, no. 5, p. 053002, 2006.

[121] Y. Bai, P. A. Hill, and I. J. Dmochowski, "Utilizing a water-soluble cryptophane with fast xenon exchange rates for picomolar sensitivity nmr measurements," *Analytical Chemistry*, vol. 84, no. 22, pp. 9935–9941, 2012.

[122] D. Baumer, E. Brunner, P. Blmler, P. P. Znker, and H. W. Spiess, "Nmr spectroscopy of laser-polarized 129xe under continuous flow: A method to study aqueous solutions of biomolecules13," *Angewandte Chemie International Edition*, vol. 45, no. 43, pp. 7282–7284, 2006.

[123] B. Driehuys, H. E. Moller, Z. I. Cleveland, J. Pollaro, and L. W. Hedlund, "Pulmonary perfusion and xenon gas exchange in rats: Mr imaging with intravenous injection of hyperpolarized xe-129," *Radiology*, vol. 252, no. 2, pp. 386–393, 2009.

[124] C. Boutin, H. Desvaux, M. Carrire, F. Leteurtre, N. Jamin, Y. Boulard, and P. Berthault, "Hyperpolarized 129xe nmr signature of living biological cells," *NMR Biomed.*, vol. 24, p. 1264, 2011.

[125] X. Zhou, D. Graziani, and A. Pines, "Hyperpolarized xenon nmr and mri signal amplification by gas extraction," *Proceedings of the National Academy of Sciences of the United States of America*, vol. 106, no. 40, pp. 16903–16906, 2009.

[126] J. P. Mugler, T. A. Altes, I. C. Ruset, I. M. Dregely, J. F. Mata, G. W. Miller, S. Ketel, J. Ketel, F. W. Hersman, and K. Ruppert, "Simultaneous magnetic resonance imaging of ventilation distribution and gas uptake in the human lung using hyperpolarized xenon-129," *Proceedings of the National Academy*

of Sciences of the United States of America, vol. 107, no. 50, pp. 21707–21712, 2010.

[127] C.-Y. Cheng, T. C. Stamatatos, G. Christou, and C. R. Bowers, "Molecular wheels as nanoporous materials: Differing modes of gas diffusion through ga10 and ga18 wheels probed by hyperpolarized 129xe nmr spectroscopy," *Journal of the American Chemical Society*, vol. 132, no. 15, pp. 5387–5393, 2010.

[128] L. Schroder, "Xenon for nmr biosensing inert but alert," *Physica Medica: European Journal of Medical Physics*, vol. 29, no. 1, pp. 3–16, 2013.

[129] P. Nikolaou, A. M. Coffey, L. L. Walkup, B. M. Gust, N. Whiting, H. Newton, S. Barcus, I. Muradyan, M. Dabaghyan, G. D. Moroz, M. S. Rosen, S. Patz, M. J. Barlow, E. Y. Chekmenev, and B. M. Goodson, "Near-unity nuclear polarization with an open-source 129xe hyperpolarizer for nmr and mri," *Proceedings of the National Academy of Sciences of the United States of America*, vol. 110, no. 35, pp. 14150–14155, 2013.

[130] M. Woods, D. E. Woessner, and A. D. Sherry, "Paramagnetic lanthanide complexes as paracest agents for medical imaging," *Chemical Society Reviews*, vol. 35, no. 6, pp. 500–511, 2006.

[131] J. Bozue, K. L. Moody, C. K. Cote, B. G. Stiles, A. M. Friedlander, S. L. Welkos, and M. L. Hale, "Bacillus anthracis spores of the bcla mutant exhibit increased adherence to epithelial cells, fibroblasts, and endothelial cells but not to macrophages," *Infection and Immunity*, vol. 75, no. 9, pp. 4498–4505, 2007.

[132] R. Giorno, J. Bozue, C. Cote, T. Wenzel, K.-S. Moody, M. Mallozzi, M. Ryan, R. Wang, R. Zielke, J. R. Maddock, A. Friedlander, S. Welkos, and A. Driks, "Morphogenesis of the bacillus anthracis spore," *Journal of Bacteriology*, vol. 189, no. 3, pp. 691–705, 2007.

[133] A. Driks, S. Roels, B. Beall, C. P. Moran, and R. Losick, "Subcellular localization of proteins involved in the assembly of the spore coat of bacillus subtilis," *Genes and Development*, vol. 8, no. 2, pp. 234–244, 1994.

[134] L. B. Zheng, W. P. Donovan, P. C. Fitz-James, and R. Losick, "Gene encoding a morphogenic protein required in the assembly of the outer coat of the bacillus subtilis endospore," *Genes and Development*, vol. 2, no. 8, pp. 1047–1054, 1988.

[135] P. Berthault, G. Huber, and H. Desvaux, "Biosensing using laser-polarized xenon nmr/mri," *Progress in Nuclear Magnetic Resonance Spectroscopy*, vol. 55, no. 1, pp. 35–60, 2009.

[136] K. V. Romanenko, *Xe-129 NMR Studies of Xenon Adsorption*, vol. 69 of *Annual Reports on NMR Spectroscopy*, pp. 1–. San Diego: Elsevier Academic Press Inc, 2010.